UCGE Reports

Number 20178

Department of Geomatics Engineering

Integration of GPS with A Medium Accuracy IMU for Metre-Level Positioning

(URL: http://www.geomatics.ucalgary.ca/links/GradTheses.html)

by

Xiaohong Zhang

June 2003

UNIVERSITY OF CALGARY

INTEGRATION OF GPS WITH A MEDIUM ACCURACY IMU FOR METRE-LEVEL POSITIONING

by

Xiaohong Zhang

A THESIS

SUBMITTED TO THE FACULTY OF GRADUATE STUDIES

IN PARTIAL FULFILMENT OF THE REQUIREMENTS FOR THE

DEGREE OF MASTER OF SCIENCE IN ENGINEERING

DEPARTMENT OF GEOMATICS ENGINEERING

CALGARY, ALBERTA

May, 2003

ABSTRACT

The estimation accuracy of a conventional Kalman filter is ultimately limited by imperfect mathematical modeling of the input noise and this issue has become a barrier to improving estimation performance for some applications. In contrast, the wave estimation method, which describes the dynamic system in a deterministic way over a short period, has the advantages of providing higher estimation accuracy in a situation where the input disturbances are of low frequency, slowly varying in nature, and rely on relatively weak observables. In the thesis, a wave estimator has been developed to integrate differential GPS (DGPS) with a medium accuracy IMU, for land positioning with the emphasis on accuracies at the metre level. A loosely coupled integration approach has been developed, which uses carrier phase-smoothed C/A-code-based DGPS positions and velocities as updates to the IMU.

Two data sets are used to assess the GPS/INS integration results. The first data set is from the CastNav 4000 GPS/INS simulator. This data set contains simulated inertial and GPS measurements with synchronized time tag. The simulator also provides a reference trajectory simultaneously as the data was logged. Another data set is from a field test near Calgary, using a Honeywell HG1700 IMU and two NovAtel OEM-4 GPS receivers. A reference trajectory for the field data was obtained by using the carrier phase kinematic positioning technique.

The above mentioned datasets were processed using a conventional Kalman filter as well as a wave estimator. For the field data set, the positioning accuracy has a RMS less than 0.5 m horizontally; the velocity estimation accuracy has a RMS value less than 3.5 cm/s when using a Kalman filter. In case of using a wave estimator, the position accuracy has a same RMS value with that of using a Kalman filter; and the velocity accuracy has an RMS value no greater than 1.26 cm/s. Both the Kalman filtering and the wave estimator case satisfied the metre-level positioning requirements. INS prediction results are also examined. For full GPS outage situation with no vehicle manoeuvring, the INS prediction accuracy is from 0.25m to 1.26m during 5 seconds and 10seconds simulated GPS data

gaps respectively. For full GPS outage situation with vehicle manoeuvring, the INS prediction accuracy varies from 3.15m to 12m during 5 seconds and 10 seconds GPS data gaps. For the simulation data set, when using a Kalman filter, a similar accuracy was achieved compared with the field data results. When using a wave estimator, the estimation results to the weakly observed state vectors achieved improved results compared with that of the Kalman filter. The horizontal misalignment angle estimation improved about 4 times.

ACKNOWLEDGEMENTS

I would like to express my great appreciation to my distinguished supervisor, Dr. M. Elizabeth Cannon, for her continued support and encouragement throughout my M.Sc. program. Her advice is very important to my current and future work.

Thanks also go to the many students in the Department of Geomatics Engineering for their assistance in data collection, pre-processing as well as for the many fruitful discussions throughout my graduate studies. Especially, I would like to acknowledge Mr. Junjie Liu for his help of processing the field test data by using new FLYKIN^{TM} software package and many helpful discussions. Mr. Mark Petovello is thanked for checking and pre-processing simulated GPS/INS raw data and many good suggestions to my thesis work. Appreciation is also extended to Mr. Michael C. Olynik, Mr. Rakesh A. Nayak, Dr. Luiz P. S. Fortes, and Mr. Shin Eun Hwan for their help during my MSc program in different ways.

I would like to acknowledge Mr. Ziwen Liu from Varco International, Inc. USA, for sharing his precious experience in the area of estimation theory, wave estimation method and inertial navigation system. Professor Oleg Salychev from the Bauman Moscow State Technical University, Russia, is thanked for his patient explanations and helpful discussions in INS, GPS/INS integration as well as in estimation methods and theories during his stay in Calgary. Special thanks also go to Dr. El-Sheimy for providing static HG1700 IMU data.

TABLE OF CONTENTS

LIST OF FIGURES

LIST OF TABLES

LIST OF NOTATION

A. CONVENTIONS

A.1. Matrices are in upper case and bold

A.2. Vectors are in lower case and bold

A.3. Rotation matrix **R** is specified by two indices denoting the two coordinates systems, e.g. $\mathrm{R}_{\mathrm{b}}^{\mathrm{l}}$ indicates a transformation from the body frame (b) to the local level frame (l)

A.4. Angular velocity of frame l with respect to frame i, coordinatized in frame b is given by:

$$\omega_{il}^{b} = [\omega_X, \omega_Y, \omega_Z]^T$$

or by corresponding skew-symmetric matrix:

$$\Omega_{il}^{b} = \begin{bmatrix} 0 & -\omega_Z & \omega_Y \\ \omega_Z & 0 & -\omega_X \\ -\omega_Y & \omega_X & 0 \end{bmatrix}$$

A.5. The following symbols specify an arbitrary quantity x:

x	true value
x_0	initial value
x_k	value at epoch k
$\dot{\mathrm{x}}$	first order derivative of x with respect to time
$\hat{\mathrm{x}}$	estimated value
x^T	transpose of x

A.6. The following operators are defined as:

(+)	Kalman updates
(-)	Kalman prediction
Δ	single difference between receivers
∇	single difference between satellites
A^T	matrix transpose
A^{-1}	matrix inverse

B. COORDINATE FRAMES

B.1 body frame (b-frame)

origin:	centre of rotation of the sensor unit
x-axis	right
y-axis	forward
z-axis	upward

B.2. Earth-fixed frame (e-frame)

origin	centre of mass of the Earth
x-axis	orthogonal to z-axis, in mean Greenwich meridional plane
y-axis	completes right-handed system
z-axis	direction of mean spin axis of the Earth

B.3. Inertial frame (I-frame)

origin	centre of mass of the Earth
x-axis	pointing towards mean vernal equinox
y-axis	completes right-handed system
z-axis	direction of mean spin axis of the Earth

B.4. Local level frame (l-frame)

origin	the same as in the b-frame

x-axis east direction on ellipsoid

y-axis north direction on ellipsoid

z-axis upward direction of ellipsoidal normal

B.5. Wander azimuth frame (w-frame)

origin the same as in the b-frame

x-axis rotate from the east towards the north in the tangent plane by an angle α

y-axis orthogonal to the x-axis in the level plane

z-axis upward direction of ellipsoidal normal

B.6. Platform frame (p-frame)

origin the same as in the b-frame

x-axis slightly misaligned from the x-axis of the l-frame

y-axis slightly misaligned from the y-axis of the l-frame

z-axis slightly misaligned from the z-axis of the l-frame

C. SYMBOLS

a semi-major axis of the reference ellipsoid

b semi-minor axis of the reference ellipsoid

b accelerometer bias

c speed of light

d gyro bias

f specific force

g gravity (magnitude)

g gravity vector

h ellipsoidal height

H design matrix in the state space model

I identity matrix

K Kalman gain

N update number within one cycle of wave method

P covariance matrix of state vector

$\mathbf{Q}$	power spectral density matrix
$\mathbf{R}$	covariance matrix of observation noise
R_M	meridional radius of curvature
R_N	prime vertical radius of curvature
$\mathbf{s}$	induced state vectors in wave estimation
$\mathbf{v}$	observation noise vector
$\mathbf{w}$	white noise process
$\mathbf{x}$	state vector
$\mathbf{z}$	measurement vector
α	wander angle
ζ	parameter of Markov process
γ	normal gravity
λ	geodetic longitude
$\mathbf{\Phi}$	transition matrix
φ	geodetic latitude
ϕ	roll
θ	pitch
ψ	yaw
$\mathbf{\Omega}$	skew symmetric matrix of vector $\boldsymbol{\omega}$
ω_e	Earth's rotation rate in the inertial space, $\omega_e=7.2921158e^{-5}$ rad s^{-1}

D. ACRONYMS

A-S	Anti-Spoofing
C/A code	Coarse/Acquisition code
CEP	Circular Error of Probability
DD	Double Difference
DGPS	Differential GPS
ECEF	Earth-Centred-Earth-Fixed reference system
FASF	Fast Ambiguity Search Filter
GPS	Global Positioning System

HDOP	Horizontal Dilution Of Precision
IMU	Inertial Measurement Unit
INS	Inertial Navigation System
L1	Civilian GPS frequency 1575.42MHz
L2	Military GPS frequency 1227.60MHz
LAMBDA	Least squares AMBiguity Decorrelation Adjustment
PDOP	Position Dilution of Precision
PPS	Precise Positioning Service
PRN	Pseudo Random Noise
RLG	Ring Laser Gyroscope
RMS	Root Mean Square
SINS	Strapdown Inertial Navigation System
LSO	Line Of Sight
SPS	Standard Positioning Service
WGS84	World Geodetic System of 1984
WE	Wave Estimation

CHAPTER 1

INTRODUCTION

1.1 Background and Objectives

The integration of the Global Positioning System (GPS) and an Inertial Navigation System (INS) has been an important development in modern navigation. GPS is a system that provides consistently accurate navigation solutions, which are generally independent of time, location and weather. GPS, by itself, is sometimes affected by signal blockage and attenuation in mountainous areas, dense forests, and areas with high-rise buildings. An INS is an autonomous, all-weather navigation system, which can provide position, velocity and attitude information in real-time. However, its navigation performance deteriorates with time due to the inertial sensor's performance. Researchers have found an efficient way to limit INS navigation errors by updating the INS velocity and position with external measurements, which have consistent accuracy over time. GPS is often used to provide these external measurements through a GPS/INS integrated system. In this case, the INS becomes an error-bounded navigator when GPS data is available. The advantages of GPS/INS integration are more than an improvement of accuracy. For example, the INS solutions can be used to identify and correct GPS carrier phase cycle slips (Cannon, 1991). Improved receiver reacquisition time by using INS to bridge GPS gaps in a tightly coupled GPS/INS Real Time Kinematic (RTK) robust positioning system has been achieved (Scherzinger, 2000). Gustafson et al. (1996) has achieved significant improvement in GPS receiver anti-jam capability by using a deeply integrated signal processing technique. Finally, positioning availability can be increased greatly (e.g. Greenspan, 1996).

The integration of GPS and INS has been successfully used in practice during the past decades. However, much of the work has focused on the use of a high accuracy Inertial Measurement Unit (IMU), which is an inertial sensors' block without navigation solutions output. These IMUs provide good accuracy measurements during GPS data

gaps, but their high cost places a severe restriction on applications (Petovello, 2001). For high accuracy positioning using GPS, carrier phase measurements are usually selected, but the carrier phase measurements are ambiguous due to an initially unknown number of cycles between the receiver and the satellite. High accuracy positioning is possible only if these ambiguities can be reliably resolved to their integer values (Kaplan, 1996). Another drawback of carrier phase processing is the relative difficulty in maintaining phase lock as compared to code lock. If a cycle slip can be detected and corrected, the associated ambiguity can be estimated as an integer value and determined by algorithms such as FASF (Chen, 1994), or LAMBDA (Teunissen and Tiberius, 1994). Although the above algorithms provide rapid ambiguity resolution capabilities, they are still limited by the error sources affecting the carrier phase measurements.

The pseudorange measurement is the time difference (in equivalent metres) between the Doppler-shifted received pseudo-random noise (PRN) code and the receiver-generated code. Since the measurement is not a true geometric range between the satellite and the receiver, but instead is significantly biased by several error sources, it is consequently denoted as a pseudorange. Differential GPS (DGPS) can cancel or reduce most of the common errors. Metre-level positioning can be achieved by DGPS using pseudorange measurements with a relatively simple carrier smoothing algorithm. One objective of this thesis is to use pseudorange-derived DGPS positions and velocities to update a medium accuracy IMU in order to achieve metre-level positioning accuracies by using a conventional Kalman filter.

Kalman filtering provides a powerful tool to create synergism between two navigation sensors - GPS receivers and INS - since it is able to take advantage of both systems' characteristics to provide a common, integrated navigation implementation with a performance superior to either of the sensor subsystems (Grewal and Weill, 2001). It gives optimal estimation as measured by the minimum mean square error (MMSE). However, it is optimal only if the system and measurement noise values are accurately modeled, and in addition, the estimation quality is only as good as the underlying model (Ray et al., 1999). Furthermore, the estimation transition state for a Kalman filter is a

sequential convergence process, which depends on the "degree of observability'' of the state variables. The weakly observed states need a longer time to converge and thus estimation during this period yields poorer results (Salychev, 2001). Reliable Kalman filtering results rely on the correct definition of both the mathematical and stochastic models used in the filtering process. At steady state, the estimation accuracy is limited by the input noise (Wang and Stewart, 2000). In recent years, some new estimation methods have been developed and wave estimation is one of them. In the wave estimation method, input disturbances are described by pseudo-deterministic models that are valid over a short time interval. This has been successfully used in navigation for the past decade; Salychev (1991) applied wave estimation approaches to an inertial surveying system (I-42) while Liu (1992) applied it to real-time azimuth estimation for a LTN 90-100 Strapdown INS initial alignment process. Ray et al. (1999) applied a modified wave estimation method to a real-time GPS/GLONASS-INS (LT-90-100) integration system. In all of the above applications, which involved a navigation-grade INS, the estimation accuracy improved significantly. The second objective of this thesis is to use a wave estimator to integrate DGPS with a medium accuracy IMU, and to compare the results with those from the conventional Kalman filter.

The design and implementation of Kalman filter and wave estimator will be assessed by using both simulation and field data. A six-hour land vehicle simulation data set from CastNav 4000 GPS/INS simulator, will be used to assess the integration results. A one-hour land vehicle field test data using the Honeywell HG1700 IMU and two NovAtel OEM4 GPS receivers is then used to assess the properties of a Kalman filter and wave estimator using real data.

1.2 Thesis Outline

In Chapter 2, both GPS and INS fundamentals are reviewed. GPS measurements and error sources are discussed. The DGPS technique to reduce these errors is also reviewed. Fundamentals of inertial navigation systems and their structures are also discussed as well as error sources, their propagation properties and error modeling. IMU raw data from both the field test and GPS/INS simulator are analyzed in order to investigate their

error properties. A stochastic model for both the gyroscope and the accelerometer are established. Finally, different integration strategies and filter architectures are discussed, and their advantages and disadvantages are briefly summarized.

Chapter 3 reviews basic estimation methodologies, i.e. conventional Kalman filtering, innovation-based adaptive Kalman filtering, as well as the wave estimation method. Properties and estimation accuracies of these methods are discussed. A loosely coupled integrated approach is selected to achieve the metre-level positioning results. The mathematical models for Kalman filtering, adaptive Kalman filtering as well as wave estimation are established. These models will be used in the next two chapters to process both the simulated and field test data sets.

Chapter 4 gives the analysis of the simulated data set from the CastNav 4000 GPS/INS simulator. This equipment creates a GPS RF and inertial environment for developing, testing, and integrating loosely-coupled GPS/INS systems. Kalman filtering and wave estimation methods are used to process this data set. Both sets of results are compared with the reference trajectory provided by the simulator. Advantages and disadvantages of both estimation methods are then discussed.

Chapter 5 focuses on the field data analysis. A test run was carried out in Calgary, Alberta, on August 16, 1999. Both DGPS and IMU data were logged simultaneously. The IMU used in this field test was a medium accuracy Honeywell HG1700 whereas the GPS receivers were NovAtel OEM4 units. Utilizing the loosely coupled model developed in Chapter 3, Kalman filtering results are first accessed. One of the advantages of GPS/INS integration is the IMU prediction during a GPS outage. Both full and partial GPS outages are simulated (as there are no outages occurring during this field test) and prediction accuracy is discussed. As an alternative of the Kalman filter, wave estimators are also used to process the data. Results from both the Kalman filter and the wave estimator are analyzed.

Chapter 6 contains conclusions and recommendations formed through this thesis as well as the topics that need further research and development.

CHAPTER 2

FUNDAMENTALS OF GPS AND INS

2.1 Global Positioning System

The GPS is a satellite navigation system maintained by the U.S. Department of Defense (DoD), and jointly managed by the DoD and the Department of Transportation. The current GPS constellation consists of 28 Block II/IIA/IIR satellites (www.navcen.uscg.gov/Ftp/gps/status.txt), occupying six orbital planes inclined with a 55-degree angle with respect to the equator. GPS satellites broadcast navigation messages and provide a global, 24-hour, all-weather navigation service (Department of Defense, 2001).

GPS satellites orbit 20,200 km above the Earth's surface with a period of about 12 hours. They transmit signals on two frequencies; L1 at 1575.42 MHz and L2 at 1227.6 MHz. These signals are bi-phase modulated by one or two PRN codes; the Coarse/Acquisition, C/A-code, and the Precise, P-code. The L1 carrier is modulated by both the C/A- and the P-codes while the L2 carrier is only modulated by the P-code. The C/A-code is transmitted at 1/10 of the fundamental GPS frequency (10.23 MHz) and is repeated every one millisecond. In contrast, the P-code is transmitted at the fundamental frequency and is only repeated every 267 days. The navigation message, containing broadcast ephemeris and health information, is modulated on both frequencies at 50 bits per second (Spilker, 1996).

The C/A-code is unrestricted and is used for the Standard Positioning Service (SPS) where single point positioning accuracies of 13 metres horizontally and 22 metres vertically can be achieved at a 95% confidence interval (Department of Defense, 2001). Recent field test at the University of Calgary shows a better result. The RMS values are on the order of 2.0 m horizontally and 4.0 to 5.0 m vertically (Skone et al., 2003). The

more accurate P-code which provides the Precise Positioning Service (PPS) to authorized users only. Unauthorized users are restricted from the P-code by the DoD. This restriction is accomplished by means of Anti-Spoofing (A-S), where the P-code is translated (to give the encrypted Y-code) except to authorized users (Hofmann-Wellenhof et al., 2001).

2.1.1 Observables and Error Sources

There are three types of GPS observables, namely, pseudorange, carrier phase and Doppler, whereby the pseudorange and carrier phase measurements are generally considered the two basic observables. Pseudorange measurements are made by comparing a receiver-replicated PRN code with the incoming signal from a particular satellite to determine the time shift needed to correlate the two signals. This time shift is the pseudorange and it represents the difference in time between signal transmission and reception, the so-called transmit time. It is called pseudorange rather than range since the receiver and satellite clocks are not synchronized, therefore, the pseudorange contains clock biases as well as other error sources. The carrier phase measurement is made by differencing the incoming carrier signal with a receiver-generated carrier signal. The resulting beat phase is therefore the difference in phase between the satellite and receiver signals at the time of measurement. Differencing of the carrier signals is much more accurate than the measurement of time in the case of the pseudorange, therefore the carrier phase has lower noise characteristics (Cannon, 1991).

The signal travels through inhomogeneous space, which has varying effects on the code (p) and carrier (Φ) measurements. The code and carrier phase observables can be expressed as (Lachapelle, 1998)

$$p = \rho + c(dt - dT) + d_r + d_{trop} + d_{ion} + d_{mult/p} + \varepsilon_p \tag{2-1}$$

$$\Phi = \rho + c(dt - dT) + \lambda N + d_r + d_{trop} - d_{ion} + d_{mult/\Phi} + \varepsilon_\Phi \tag{2-2}$$

where ρ is the geometric range (m)

c is the speed of light (m/s)

dt	is the satellite clock error (s)
dT	is the receiver clock error (s)
d_r	is the orbital error (m)
d_{ion}	is the ionosphere delay (m)
d_{trop}	is the troposphere delay (m)
$d_{\rho mult}$	is the pseudorange multipath effect (m)
ε_p	is the pseudorange measurement noise (m)
λ	is the wavelength of GPS carrier (m)
	0.19m for L1 and 0.24m for L2
N	is the integer ambiguity (cycles)
$d_{\Phi mult}$	is the carrier phase multipath effect (m), and
ε_Φ	is the carrier phase measurement noise (m).

The carrier phase measurement generated from the receiver contains only the fractional part of the geometric range, so it is ambiguous. The ambiguity, N, is an integer value which represents the difference between the true range and measured phase. The ambiguity is constant over a measurement time span provided there are no cycle slips in the carrier phase data. Cycle slips are caused in situations such as satellite shading, extreme vehicle dynamics, intense ionosphere activity, etc., and results in loss of phase lock between the receiver and the satellite.

The Doppler frequency is the third observable and it represents the rate of change of the carrier phase observable. It reflects the relative velocity between the receiver and the GPS satellite. This information can be used for velocity derivation and cycle slip detection. This observable can be expressed as (Lachapelle, 2001):

$$\dot{\Phi} = \dot{\rho} + c(d\dot{t} - d\dot{T}) + \dot{d}_r + \dot{d}_{trop} - \dot{d}_{ion} + \dot{d}_{mult/\Phi} + \dot{\varepsilon}_{\Phi} \qquad (2\text{-}3)$$

where $\dot{\Phi}$ is the Doppler (m/s)

$\dot{\rho}$ is the range rate between the receiver and the satellite (m/s), and

$(\bullet)$ denotes a time derivative.

It should be noticed that the ambiguity term is gone after time derivation calculus.

Ionospheric Error

The ionosphere is a region of the atmosphere extending roughly from 50 to 1,500 km, and it is characterized by a significant number of free electrons (with negative charge) and positively charged ions (Leick, 1995). Free electrons affect the propagation of radio waves, so they are of interest to GPS users. The ionosphere can cause a group delay of the modulated signal, a carrier phase advance and scintillations, which are the small-scale irregularities in the electron content of the ionosphere, with spatial extents from a few metres to a few kilometres. It can produce both refraction and diffraction effects on received GPS signals (Wanninger, 1993). It should be noted that the effects on the code and carrier phase have the same value but opposite sign.

The ionospheric error can be of the order of 2-50 m in single point positioning mode and it can be reduced by DGPS processing. The improvement depends on the baseline length between the reference station and the remote receiver, as the ionosphere decorrelates spatially. The residual error is approximately 2 parts per million (ppm) with differential corrections, but it may reach 20 ppm or more under extreme high ionospheric conditions (e.g. Lachapelle, 2001), since the activity of the ionosphere is strongly affected by the number of the sunspots, which are dark patches on the Sun. The number of sunspots on the Sun at any given time varies in an 11-year cycle as does the number and severity of disturbances in space weather (Bugoslavskaya, 1962). Figure 2-1 shows the sunspot numbers in the last solar cycle (solar maximum occurred in the middle of 2000). (http://science.msfc.nasa.gov/ssl/pad/solar/images/ssn_predict_l.gif). Figure 2-2 shows

the evolution of the Earth's mean TEC in the same period (http://www.aiub.unibe.ch/ionosphere/meantec.gif). They are consistent largely.

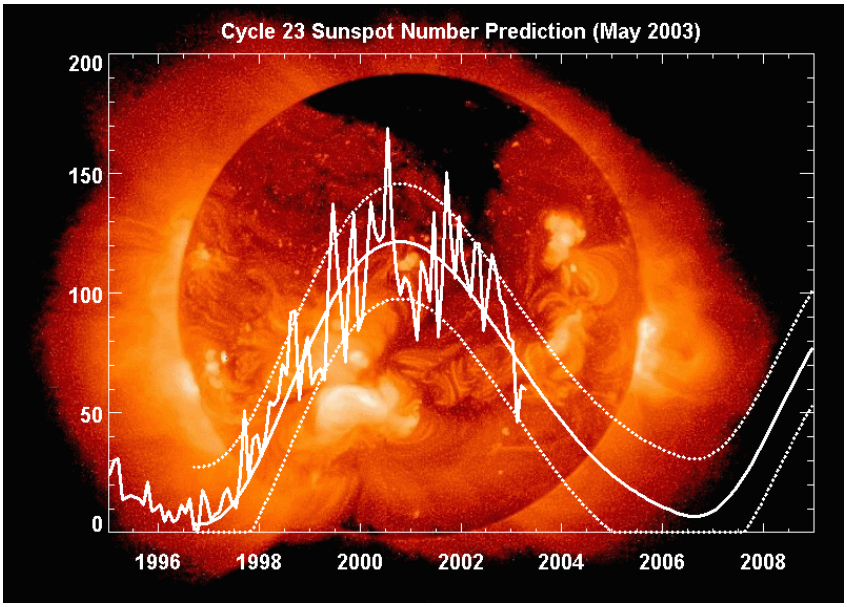

Figure 2-1 Sunspot Numbers and the Periodic Behaviors

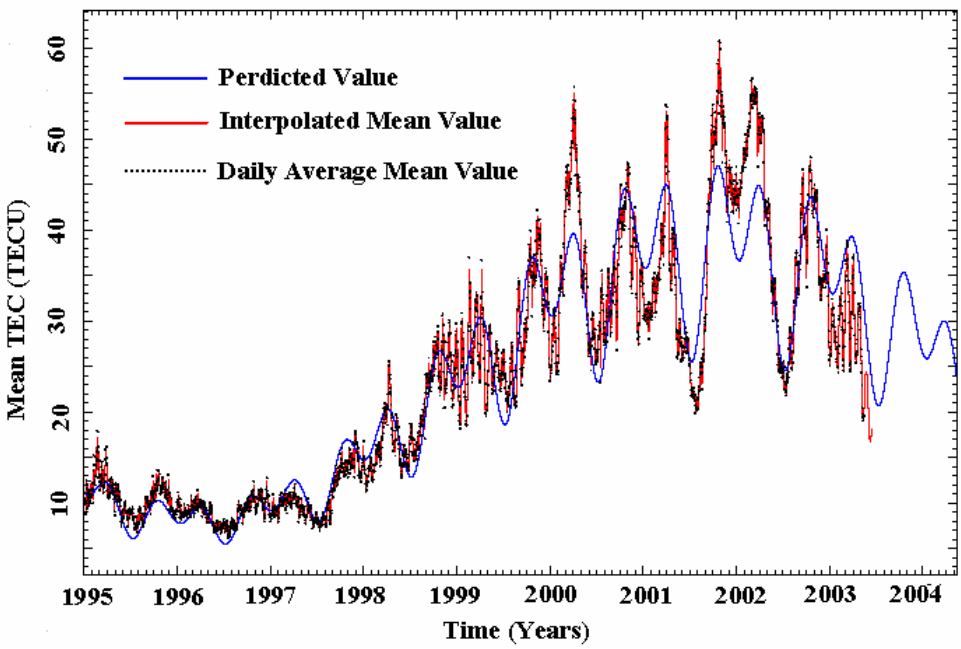

Figure 2-2 Earth's Mean TEC and the Periodic Behaviors

In addition to varying with the solar cycle, the TEC presents the following type of variations (Skone, 1999):

1 Daily: Maximum around 2:00 pm local time in the equatorial region.

2 Seasonal: Lowest TEC in the summer (of the Northern Hemisphere); minima close to the equinoxes (March and September) and in the winter. These characteristics follow the months of the year, not the season, which means that they are opposite for the Southern Hemisphere, i.e. lowest in the winter and maximum in the summer.

3 Geographic: Two maxima at ±10° from the magnetic equator, in the region under the so-called equatorial anomaly.

Tropospheric Delay

The troposphere is the lower part of the Earth's atmosphere where temperature decrease with an increase in altitude. The thickness of the troposphere is not the same everywhere. It extends to a height of less than 9 km over the poles and in excess of 16 km over the equator (Lutgens and Tarbuck, 1989). The troposphere is electrically neutral and non-dispersive for frequencies as high as about 15 GHz. Within this medium, group and phase velocities of the GPS signal on both the L1 and L2 frequencies are equally reduced. The influences of the troposphere on the GPS measurement can be expressed by wet and dry components. The wet component depends on the distribution of the water vapour in the atmosphere and is harder to model. However, it is responsible for only 10% to 20% of the total troposphere refraction. The dry component can be precisely described by models (Seeber, 1993). Mendes (1999) presents a detailed description and analysis of several models. The resulting delay is a function of atmospheric temperature, pressure, and moisture content. Without appropriate compensation, tropospheric delay will induce pseudorange and carrier-phase errors from about 2 metres for a satellite at the zenith to more than 20 metres for a low-elevation satellite (Spilker, 1996). The residual tropospheric error is about 1 ppm in differential mode (Lachapelle, 1998).

Orbital Error

To use GPS for positioning, it is generally assumed that the satellite coordinates are known. These orbits are expressed in terms of an ephemeris, which is a mathematical description of where a satellite is at a given time (Roulston et al., 2000). The satellite coordinates are then developed from these ephemerides.

Three types of data are available to determine position and velocity vectors of the satellites in a terrestrial reference frame at any instant: almanac, broadcast ephemerides, and precise ephemerides (Hofmann-Wellenhof et al., 2001). These data types differ in accuracy. The broadcast orbit RMS accuracy currently is about 2 m (Beutler, 1997). The GPS Accuracy Improvement Initiative (AII) focuses on enhancing the quality of the clock and ephemeris parameter values embedded within the broadcast navigation message (Hay, 2000). Once operational in 2005, AII is expected to reduce the signal-in-space range error (SISER) to 1.3 m RMS (ibid).

In order to derive more precise orbits needed for scientific and engineering applications, several groups started to compute what is known as precise ephemerides (Fortes, 2002). Among them are the official precise orbits computed by the Navel Surface Warfare Center together with National Imagery and Mapping Agency (NIMA), available upon request about 4-8 weeks after the observations (Buetler et al., 1998), and the orbit computed by the International GPS Service (IGS) (IGS, 2001). IGS products are currently used by a large user community because of their user-friendly properties. The accuracy of the real-time IGS Ultra-Rapid (Predicted) orbit product is about 0.25 m and updated twice per day. The accuracy of the IGS Rapid orbit product is about 0.05 m, updated daily with a latency of 17 hours. The accuracy of IGS final orbit product is better than 0.05 m, updated weekly with a latency of 13 to 20 days (IGS ACC, 2001). In this thesis the broadcast ephemeredes are used.

Satellite Clock Error

GPS satellites use two types of atomic clocks: rubidium and caesium. Satellite clock error is referred to as the difference between the satellite clock and the GPS system time (reference clock). This is monitored by the Master Control Station (MCS) and the errors are transmitted as coefficients of a polynomial as a part of the navigation message. Satellite clock errors can be effectively eliminated through DGPS (Lachapelle, 2001).

Receiver Clock Error

Receiver clock error is the offset between the receiver clock and the GPS system time. The error magnitude is a function of the receiver's internal firmware. It can vary between 200 μs to a few ms. Receiver clock error changes with time due to the clock-drift. Receiver clock error can be established along with station coordinates, or it can be completely removed by single differencing between satellites (Cannon, 1999).

Multipath and Noise Errors

The above discussed errors can be minimized or removed by DGPS corrections; however, multipath and receiver noise cannot be compensated by using DGPS.

Multipath is the corruption of the direct GPS signal by one or more signals reflected from the local surroundings. These reflections affect both pseudorange and carrier-based measurements in a GPS receiver. As shown in Figure 2-3, the reflector of electromagnetic signals could be buildings, metal surfaces, water bodies, and the ground (Nayak, 2000). Pseudorange multipath is limited by the chipping rate. The higher the chipping rate, the lower the maximum multipath (Leick, 1995). The maximum C/A-code multipath can reach a magnitude of about 0.5 of a code chip (150 m), and generally there is no effect from reflectors that are more than 150 m from the antenna (Lachapelle, 2001). The maximum carrier-phase multipath can reach 0.25 λ, which means that it will not exceed 4.75 cm for L1 (Ray, 2000).

Measurement noise is any noise that is generated by the receiver itself in the process of taking the pseudorange or the phase measurement. It is considered to be white noise, and the receiver noise level is dependent on a number of factors (Raquet, 1998). For instance, it is usually a function of the code correlation method, receiver dynamics and antenna gain pattern. With narrow correlation techniques, the measurement noise is at a level ranging from 0.1 % to 1 % of the measurement wavelength (Nayak, 2000). The noise on the pseudorange is at a level of 5 to 10 centimetres for high elevation satellites; it may increase to tens of centimetres for lower elevation satellite; while only several millimetres on the carrier phase observable (Raquet, 1998). The receiver noise increases by $\sqrt{2}$ when differential correction is applied.

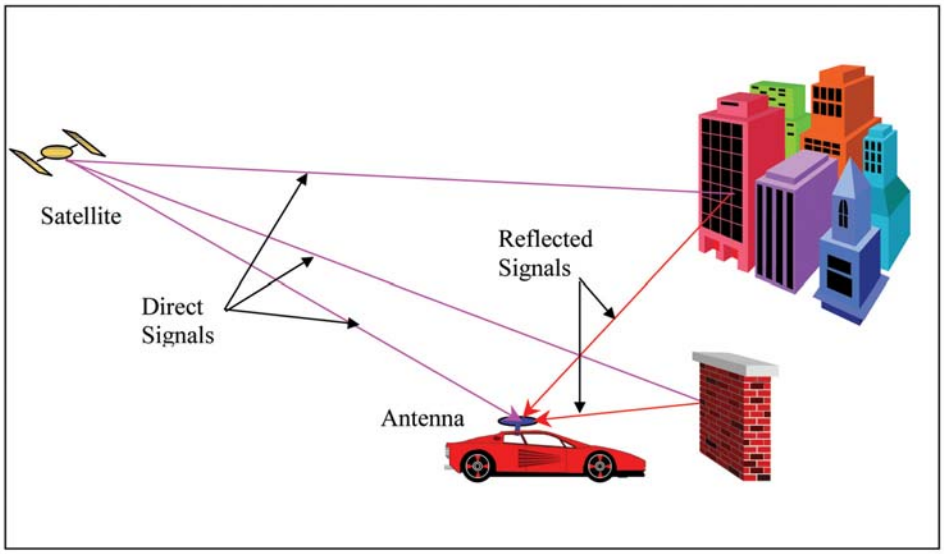

Figure 2-3 Multipath Environment Example (from Nayak, 2000)

2.2 Inertial Navigation Systems (INS)

The basic principle of an INS is based on the integration of accelerations observed by the accelerometers on board the moving platform. The system will accomplish this task through appropriate processing of the data obtained from the specific force and angular velocity measurements. Thus, an appropriately initialized inertial navigation system is

capable of continuous determination of vehicle position, velocity and attitude without the use of the external information (Britting, 1971).

2.2.1 Hardware Configurations

There are three types of INS, namely space-stabilized systems (SSINS), local-level systems (LLINS), and strapdown systems (SINS) (Salychev, 1995).

Space-Stabilized System

The space-stabilized system keeps its sensor axes coinciding with an inertial frame. It requires the system to establish its orientation with respect to the inertial frame and to torque the platform back by the amount of rotation it senses, as shown in Figure 2-4. The rectangular box represents the platform; the frame axis with a subscript l refers to the local level frame, and the inertial frame axis is subscripted with an i. At the starting point A, it is assumed that the local level frame and the inertial frame coincide. When the SSINS moves from point A to point C, the local level frame rotates an angle relative to inertial space; however, the platform frame tracks the inertial frame so, it still coincides with inertial frame. The integration of the raw data is performed in the inertial frame as well. The result can then be transformed to the local level frame. The main disadvantage of this system is that the gyros and accelerometers are put into a varying gravity field.

Local-Level System

A local-level system aligns its sensor axis with the local level frame. The platform is constantly torqued in order to coincide with the local level frame; the navigation solutions will be obtained in this frame as well. The advantage of a local level system is that no coordinate transformation is needed so the navigation calculation is relatively simple. The problem is that when the system works in the polar region, the control torque becomes very large, so the local level system usually transfers to a wandering mode when it works in high latitude areas (Lei, 1978). Figure 2-5 shows how the LLINS works. When the LLINS t moves from point A to point C, the local level frame rotates an angle with respect to the inertial space, and the platform tracks the rotation of the local level frame. The platform frame axis still coincides with the local level frame.

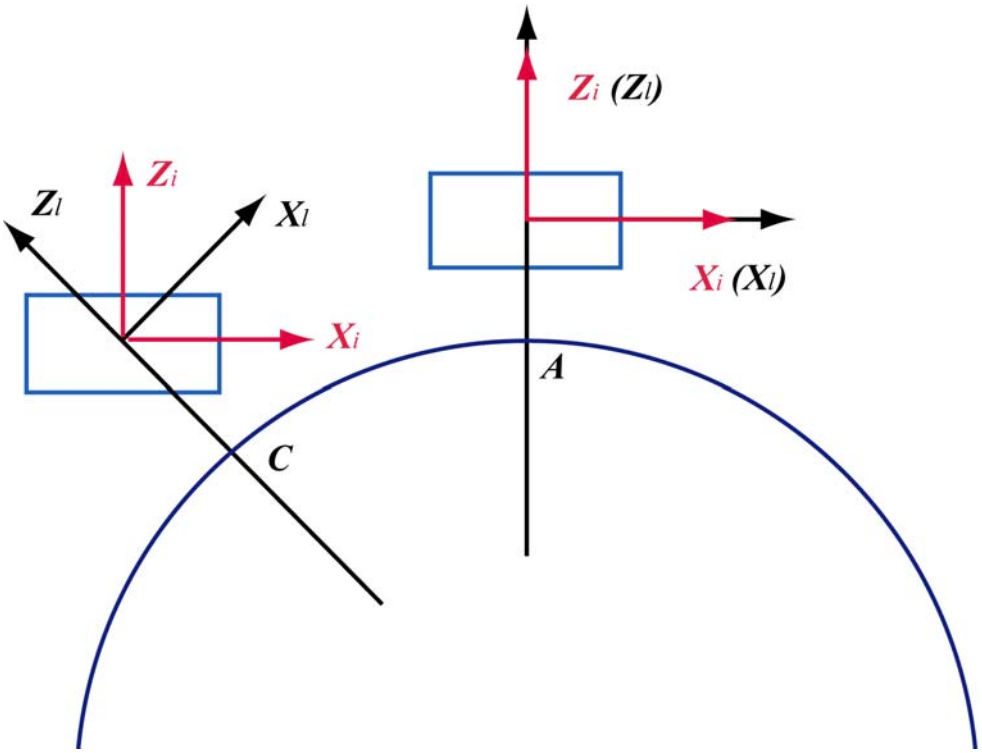

Figure 2-4 Space Stabilized Inertial Navigation System

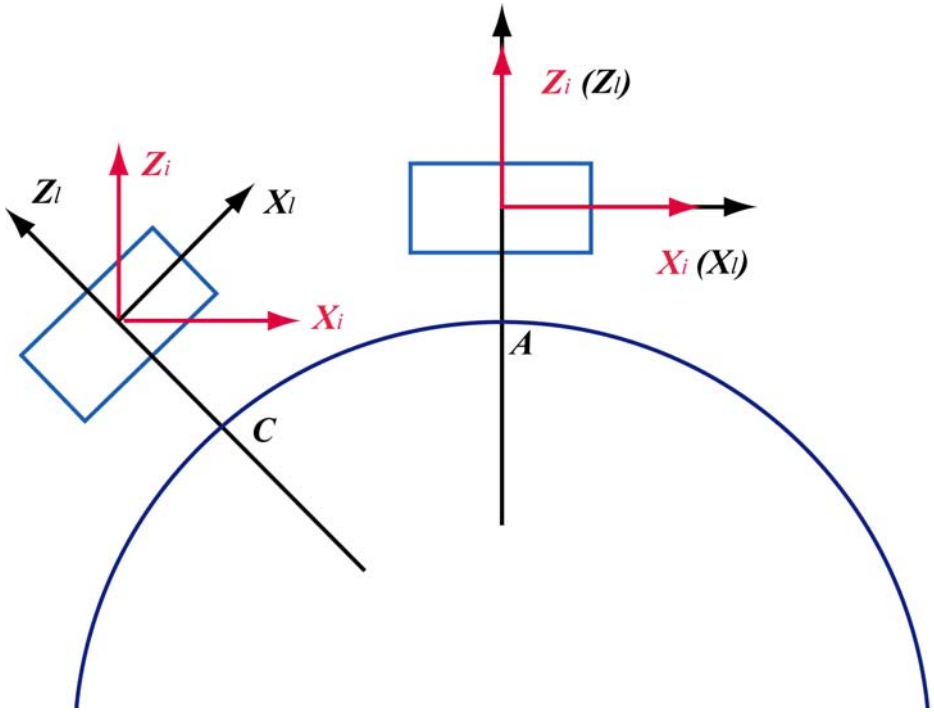

Figure 2-5 Local Level Inertial Navigation Systems

Strapdown Inertial Navigation System

Both above mentioned systems have a mechanical platform, which is torqued to track the navigation frame. Therefore, they are called gimballed systems. The third system is the strapdown inertial navigation system (SINS). In a SINS, the gyroscope and the accelerometer triads are directly mounted on the moving vehicle; therefore, the sensors are not mounted on a stabilized platform as in the case of a gimballed system. In an SINS, a mathematical platform is established in the computer. The sensors measure the rotation rates and the specific forces along the axes of the body frame. If the initial Euler angles and velocities of the system are known, the rotation rate of the system due to the Earth's rotation and system velocity can be removed from the measured rate in order to obtain the attitude rate. The Euler angle increment can be achieved by integrating the attitude rate, so the systems Euler angle can be determined. Once the Euler angle is known, the measured specific force can be transformed to a local level or wandering frame; therefore, the navigation solution will be achieved as that in the local level system.

An IMU and the navigation mechanization algorithms form an INS. The IMU is a single unit, which collects angular velocity and linear acceleration data and then sends it to the onboard microprocessor. The IMU housing actually contains two separate sensor triads. The first one is the accelerometer triad. The signal it generates represents the accelerations along each of its axes produced by, and acting on, the vehicle. The second sensor triad is the gyroscope triad; the signals it outputs describe the vehicle angular rate about each of the sensor axes. Even though the IMU is not located at the vehicle centre of mass, the angular rate measurements are not affected by linear or angular accelerations. Navigation mechanization equations are the computer implementation of the INS equations based on the computed and measured variables (Farrel and Barth, 1999). Mechanization equations can be established in different frames according to the application tasks. The inertial sensor used in this research is a Honeywell HG1700 strapdown IMU, which is a medium accuracy unit using Ring Laser Gyroscope (RLG) technology (Honeywell Inc.). Compared to its mechanical gyroscope counterpart, system

reliability is increased since an RLG does not have any moving parts. In addition, the costs of RLGs are also lower than mechanical gyros. However, except for very high-end products, the noise level of RLGs is higher than mechanical gyros. Therefore, it is very important to establish proper error models and apply gyro drift testing and compensations before the system can be switched to navigation mode. This will be discussed in Section 2.2.4.

2.2.2 Mechanization Equations

Measurements from the gyros and the accelerometers are the angular velocities and specific forces about and along the three axes of the body frame (b-frame), which is a 3-D coordinate system coinciding with the output axes of the sensor block, as shown in Figure 2-6. The navigation frame is where the data integration is performed. Users can select any coordinate system as the navigation frame depending on the application requirements. The local level frame is often selected as the navigation frame because of its computational efficiency and convenience (Lei, 1978).

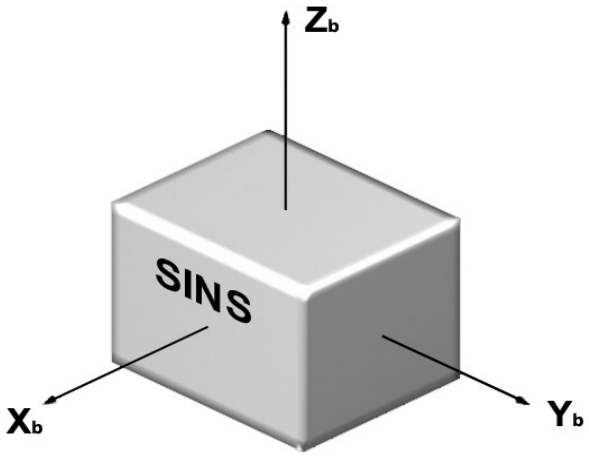

Figure 2-6 Definition of Body Frame

Sensors errors involved in the raw measurements must be compensated before they are sent to the mechanization equations to calculate the navigation solutions. These sensor errors contain deterministic and random components. Error properties and modeling will be discussed in detail in Section 2.2.3.

After the sensor error compensation of the raw measurements sensed in the body frame, the angular velocities are integrated to update the transformation matrix from the body frame to the navigation frame, i.e., $\mathbf{R}_b^l$, by using the quaternion method (Salychev, 1998). The linear accelerations along the body frame axes obtained from the specific force measurements are transformed to the navigation frame, and are integrated to obtain the velocity and position in the navigation frame.

In inertial space, Newton's second law of motion can be expressed as follows:

$$\ddot{\mathbf{r}}^i = \mathbf{f}^i + \mathbf{G}^i \tag{2-4}$$

where (i) refers to the inertial frame

$\mathbf{f}^i$ is the specific force vector

$\ddot{\mathbf{r}}^i$ is the acceleration vector of the INS carrier, and

$\mathbf{G}^i$ is the gravitational acceleration vector.

The above equation can be transformed into the local level frame conveniently, and can be expressed as the following set of first order differential equations, see Schwarz and Wei (2000) for details:

$$\begin{bmatrix} \dot{\mathbf{r}}^l \\ \dot{\mathbf{v}}^l \\ \dot{\mathbf{R}}_b^l \end{bmatrix} = \begin{bmatrix} \mathbf{D}\mathbf{v}^l \\ \mathbf{R}_b^l \mathbf{f}^b - (2\boldsymbol{\Omega}_{ie}^l + \boldsymbol{\Omega}_{el}^l)\mathbf{v}^l + \mathbf{g}^l \\ \mathbf{R}_b^l \boldsymbol{\Omega}_{lb}^b \end{bmatrix} \tag{2-5}$$

where l refers to local level frame

The position vector can be expressed as:

$$\mathbf{r}^l = (\varphi,\ \lambda,\ h) \tag{2-6}$$

φ is the latitude, λ is the longitude and h is the height.

The velocity vector in l-frame can be expressed as equation (2-7) and **D** is a 3×3 square matrix, which expressed the relationship of the velocity and position vector in local level frame.

$$\mathbf{v}^l = ((R_N + h)\ \dot{\lambda}\cos\varphi,\ (R_M + h)\ \dot{\varphi},\ \dot{h}) \tag{2-7}$$

$$\mathbf{D} = \begin{bmatrix} 0 & 1/(R_M + h) & 0 \\ 1/(R_N + h)\cos\varphi & 0 & 0 \\ 0 & 0 & 0 \end{bmatrix} \tag{2-8}$$

$$\mathbf{g}^l = \mathbf{G}^l - \mathbf{\Omega}_{ie}^l \mathbf{\Omega}_{ie}^l \mathbf{r}^l \tag{2-9}$$

$\mathbf{g}^l$ is the gravity vector in the local level frame, and

$\mathbf{\Omega}_{ie}^l$ is the skew-symmetric matrix of the angular velocity vector $\boldsymbol{\omega}_{ie}^l$.

Equation (2-10) is the earth rate relative to the inertial space projected in l - frame

$$\boldsymbol{\omega}_{ie}^l = [0,\quad \omega_e\cos\varphi,\quad \omega_e\sin\varphi]^T \tag{2-10}$$

$\mathbf{\Omega}_{el}^l$ is the skew-symmetric matrix of the angular velocity vector $\boldsymbol{\omega}_{el}^l$

$$\boldsymbol{\omega}_{el}^l = [-v_n / R_M,\quad v_e / R_N,\quad v_e \tan\varphi / R_N]^T \tag{2-11}$$

is the angular velocity vector of the l-frame relative to e-frame

$\mathbf{\Omega}_{lb}^b$ is the skew-symmetric matrix of the angular velocity vector $\boldsymbol{\omega}_{lb}^b$

$$\boldsymbol{\omega}_{lb}^b = \boldsymbol{\omega}_{ib}^b - \mathbf{R}_l^b \boldsymbol{\omega}_{il}^l \tag{2-12}$$

$$\boldsymbol{\omega}_{ib}^b = \tilde{\boldsymbol{\omega}}_{ib}^b - \mathbf{d}_{ib}^b \tag{2-13}$$

$\tilde{\boldsymbol{\omega}}_{ib}^b$ is the gyro sensed angular velocity vector

$\mathbf{d}_{ib}^{b}$ is the gyro drift vector

$\boldsymbol{\omega}_{ib}^{b}$ is the corrected angular velocity vector in body frame

$\mathbf{R}_{b}^{l}$ is the transformation matrix from body frame to local level frame

$$\mathbf{f}^{b} = \tilde{\mathbf{f}}^{b} - \mathbf{b}^{b} \tag{2-14}$$

$\tilde{\mathbf{f}}^{b}$ is the accelerometer sensed acceleration in body frame

$\mathbf{b}^{b}$ is the accelerometer bias vector

v_e , v_n are east and north velocity respectively, and

R_M , R_N are the radii of the meridian and prime vertical respectively.

The computation involved to implement the system described in equation (2-5) includes the processing of angular rate measurements implied in the term $\boldsymbol{\Omega}_{lb}^{b}$ and the specific force term $\mathbf{f}^{b}$ as shown in Figure 2-7. Firstly, gyro drift corrections are applied to the measured body rates with respect to inertial space by using equation (2-13). The corrected angular rate measurements are then used to compute the transformation matrix between the body and navigation frames, which is required to transform the specific force measurements from the accelerometers. This transformation matrix, $\mathbf{R}_{b}^{l}$, must be continuously updated in order to follow the vehicle dynamics. Secondly, the specific force measurements, $\tilde{\mathbf{f}}^{b}$, will be corrected by the accelerometer bias first, as shown by equation (2-14), then the corrected specific force measurements will be transformed from the body to the navigation frame. As the specific force contains all the sensed accelerations, the Coriolis acceleration, gravitational and centrifugal accelerations must be removed in order to extract correct vehicle velocity and position. The Coriolis acceleration is a function of the vehicle velocity while the sum of gravitational and centrifugal acceleration is the gravity which can be approximated by the free-air normal gravity $\boldsymbol{\gamma}^{l}$. Details of these corrections can be found in Wong (1988). The corrected

specific force now represents the vehicle acceleration, and can be integrated to get the vehicle velocity increments.

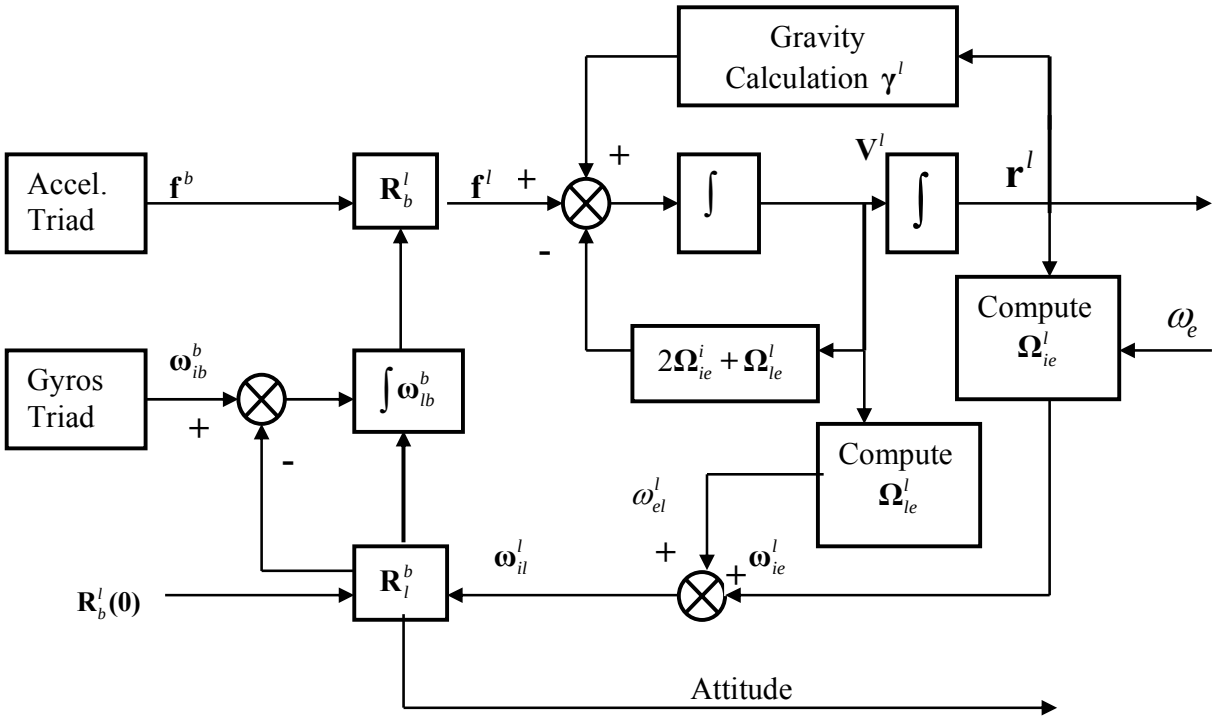

Figure 2-7 Diagram of SINS Mechanization Equation Solution in the Local Level Frame

2.3 Error Sources and Properties

INS navigation solutions are degraded by sensor errors and random disturbances (Salychev, 1998). These error sources include (1) Bias errors: a constant signal on the output, independent of input, and can be modeled as random walk. (deg. /hr); (2) Scale factor errors: linear and proportional to input. (Usually expressed in ppm); (3) Misalignment: ideally, the gyro and accelerometer defined an orthogonal triad, but the installation can not be perfect (it is also called non-orthogonality); (4) Temperature error: temperature dependence of bias and scale factor errors; and (5) Quantization errors: A/D converter has finite precision where very weak signals are treated as noise (Lei, 1978). Inertial error sources can be divided into two categories. One category contains stationary

errors like the random constant part of the gyro drift. Every time the system is started, a unique "constant" drift can be determined by initial calibration and drift testing process. The other kind of errors are non-stationary errors like the accelerometer scale factor. It has terms related to the acceleration and the rate of acceleration, others like non-orthogonality of the sensor's installation. They are dependent on the body dynamics to a great extent, which makes the inertial sensors have a large error during vehicle dynamics (Salychev, 2001).

For the stationary part, there are two error propagation properties: un-damped oscillation and un-bounded position errors. Computer-simulated INS errors are shown in Figure 2-8 and Figure 2-9. Figure 2-8 shows the misalignment angle. For an initial value of three arc-seconds due to the accelerometer bias, it causes an un-damped oscillation with a maximum magnitude of about 6 arc-seconds. Figure 2-9 shows the east position error caused by a constant gyro drift of 0.01 deg/hr. It will become un-bounded over time. These errors also propagate with three different frequencies. Figure 2-8 and Figure 2-9 show the relationship of these three frequencies: the Shuler frequency (ω_s=1.24e-2 rad/s), Earth rotation (ω_e=7.2921158e-5 rad/s) and Foucault frequency ($\omega_f = \omega_e \sin\varphi$). In Figure 2-8, the Shuler frequency modulates the Foucault period; and in Figure 2-9 the Shuler frequency is superpositioned with the Earth period. Therefore, it is necessary to damp the Shuler and Earth frequencies for long-term applications (Lei, 1978).

For the Honeywell HG1700 used in this research, the day to day gyro drift is up to 1.0 deg / hr (Ford, 2001). If there is no compensation, the positioning errors will be as high as 16 nautical miles per hour. (Detailed description of this system is given in Section 5.1.) Therefore, the initial calibration and drift compensation is very important in order to achieve high accuracy position results. For details see Shin (2001).

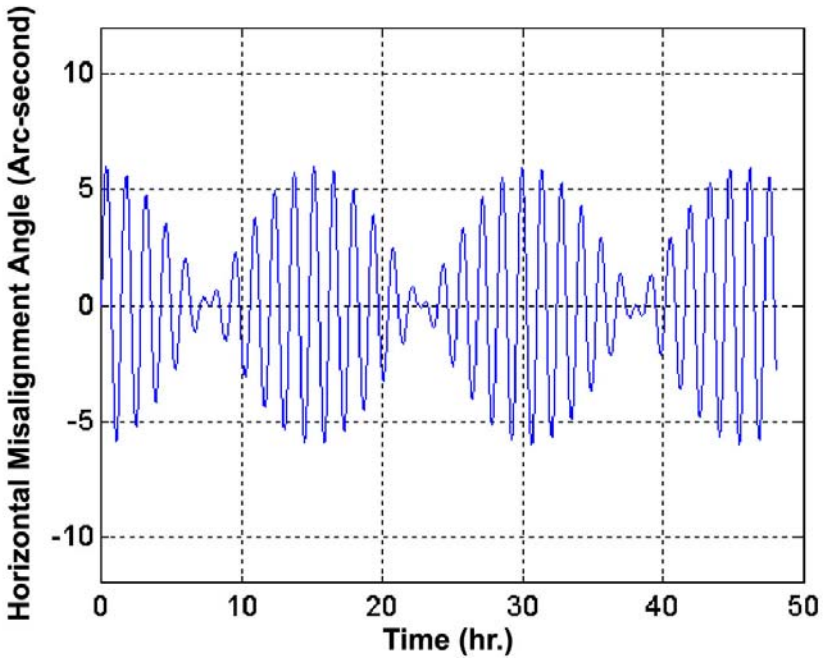

Figure 2-8 Simulated INS Horizontal Misalignment Angle

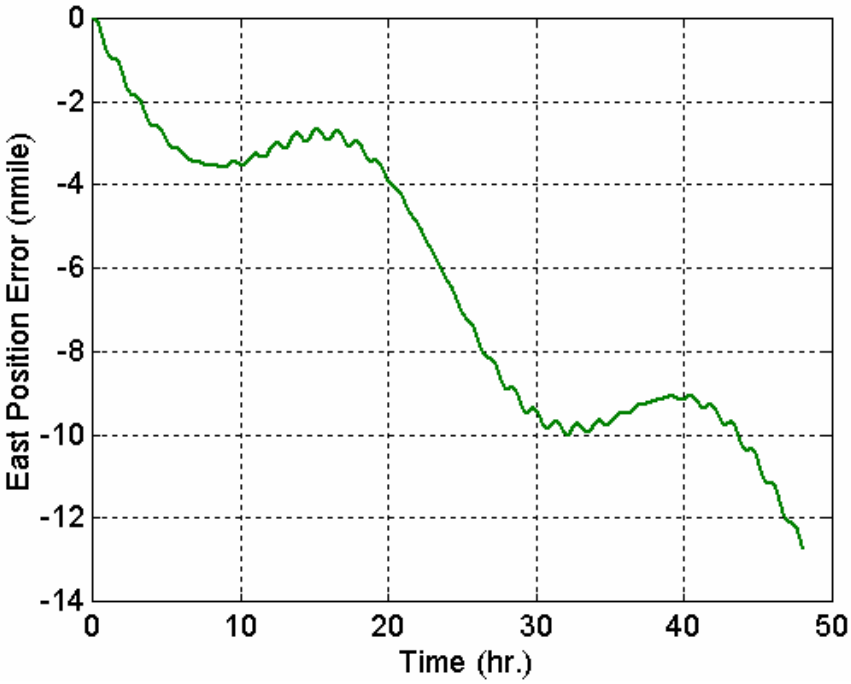

Figure 2-9 Simulated INS Position Errors

2.2.4 INS Error Models

The errors that need to be estimated include misalignment angles, position errors, velocity errors and sensor biases. They are defined as the deviations of the computed values from the true values. Their behaviour can be modeled by applying perturbing techniques, i.e. by assuming the navigation quantities are perturbed from their true values by a small amount and deriving the expression for those small deviations from the true values as a set of first-order differential equations. The following is an overview of the errors and for the details see Wong (1988).

Attitude Errors

Attitude errors are defined as the misalignment angles due to the orthogonal transformation errors between the body frame and the local level frame coordinate axes, expressed in the local level frame (Salychev, 1998), as shown in equation 2-15, where **E** is skew-symmetric matrix of the misalignment angle $\boldsymbol{\varepsilon}^{l}$.

$$\tilde{\mathbf{R}}_b^l = (\mathbf{I} + \mathbf{E})\mathbf{R}_b^l \tag{2-15}$$

State space model is:

$$\dot{\varepsilon}^l = -\boldsymbol{\Omega}_{il}^l \varepsilon^l - \boldsymbol{\delta\omega}_{il}^l + \mathbf{R}_b^l \boldsymbol{\delta d} \tag{2-16}$$

where

$$-\boldsymbol{\Omega}_{il}^l = \begin{bmatrix} 0 & \omega_e \sin\varphi & \omega_e \cos\varphi \\ -\omega_e \sin\varphi & 0 & -\varphi \\ \omega_e \cos\varphi & \varphi & 0 \end{bmatrix} \tag{2-17}$$

$$\boldsymbol{\omega}_{il}^l = \begin{bmatrix} -\delta\varphi \\ -(\omega_e + \dot{\lambda})\sin\varphi\delta\varphi + \cos\varphi\delta\dot{\lambda} \\ (\omega_e + \dot{\lambda})\cos\varphi\delta\varphi + \sin\varphi\delta\dot{\lambda} \end{bmatrix} \tag{2-18}$$

δd is the residual gyro drift

~ represents errors

I is the identity matrix

Position Errors

$$\delta\dot{\varphi} = \frac{\delta V_N}{R_m} \tag{2-19}$$

$$\delta\dot{\lambda} = \frac{\delta V_E}{R_n \cos\varphi} + \frac{V_E}{R_n \cos\varphi} \tan\varphi\delta\varphi \tag{2-20}$$

$$\delta\dot{h} = \delta v_z \tag{2-21}$$

Velocity Errors

$$\dot{\boldsymbol{\delta\mathbf{v}}}^l = -\mathbf{F}^l\boldsymbol{\varepsilon}^l - (\boldsymbol{\Omega}_{el}^l + 2\boldsymbol{\Omega}_{ie}^l)\boldsymbol{\delta\mathbf{v}}^l + \mathbf{V}^l(\boldsymbol{\delta\omega}_{el}^l + \mathbf{2}\boldsymbol{\delta\omega}_{ie}^l) + \mathbf{R}_b^l\boldsymbol{\delta\mathbf{b}} + \boldsymbol{\delta\gamma}^l \tag{2-22}$$

where **F** is the skew-symmetric matrix of the specific force vector $\mathbf{f}^l$

$\mathbf{V}^l$ is the skew-symmetric matrix of the velocity vector $\mathbf{v}^l$

$\boldsymbol{\delta\gamma}^l$ is the error in the normal gravity vector

$$-\mathbf{F}\boldsymbol{\varepsilon}^l = \begin{bmatrix} 0 & f_u & -f_n \\ -f_u & 0 & f_e \\ f_n & -f_e & 0 \end{bmatrix} \begin{bmatrix} \varepsilon_e \\ \varepsilon_n \\ \varepsilon_u \end{bmatrix} \tag{2-23}$$

f_n f_e f_u are the north, east and up components of the specific force respectively

$$-(\boldsymbol{\Omega}_{el}^l + 2\boldsymbol{\Omega}_{ie}^l)\boldsymbol{\delta\mathbf{v}}^l = \begin{bmatrix} 0 & 0 & 0 \\ -R\dot{\lambda}\cos\varphi\sin\varphi & 0 & 0 \\ R\dot{\lambda}\cos^2\varphi & R\dot{\varphi} & 0 \end{bmatrix} \begin{bmatrix} \delta\dot{\lambda} \\ \delta\dot{\varphi} \\ \delta\dot{h} \end{bmatrix} \tag{2-24}$$

$$\boldsymbol{\delta\gamma}^{l} = \begin{bmatrix} 0 \\ 0 \\ -\dfrac{\partial\gamma}{\partial h}\delta h \end{bmatrix} = \begin{bmatrix} 0 \\ 0 \\ \dfrac{2\gamma}{R}\delta h \end{bmatrix} \tag{2-25}$$

δb is the residual accelerometer bias, and

R is the mean radius of the Earth.

In the above equations, the following approximation has been made in order to simplify the formulas:

$$\omega_e >> \dot{\varphi}, \dot{\lambda}, \;\; \dot{\varphi}, \dot{\lambda} >> \frac{\dot{h}}{R}$$

This is true for most of the land and marine platform dynamics. For high dynamic vehicles, however, the equations will be slightly different from those given here (Cannon, 1991).

Sensor Errors

The variation of the residual gyro drift and accelerometer bias from alignment to alignment is random. They can be modeled by a first order Gauss-Markov process as described by equations (2-26) and (2-27) or white noise, shown in equations (2-28) and (2-29), according to the analysis results from the field data.

$$\dot{\mathbf{d}} = -\zeta\mathbf{d} + \mathbf{w} \tag{2-26}$$

$$\dot{\mathbf{b}} = -\beta\mathbf{b} + \mathbf{w} \tag{2-27}$$

$$\dot{\mathbf{d}} = \mathbf{0} \tag{2-28}$$

$$\dot{\mathbf{b}} = \mathbf{0} \tag{2-29}$$

In this research, the sensor errors are described by white noise. Equations (2-28) and (2-29) will be used to model the gyro and accelerometer errors in the following chapters.

Error Models of Dynamic System

The error equations discussed above can be written in matrix form

$$\dot{\mathbf{x}} = \mathbf{F}\mathbf{x} + \mathbf{w} \tag{2-30}$$

where

$$\mathbf{x} = [\varepsilon_n \ \varepsilon_e \ \varepsilon_u \ \delta\varphi \ \delta\lambda \ \delta h \ \delta\dot{\varphi} \ \delta\dot{\lambda} \ \delta\dot{h} \ d_x \ d_y \ d_z \ b_x \ b_y \ b_z]^T \tag{2-31}$$

The dynamics matrix F is shown in Figure 2-12.Equation (2-30) is called the system model and equation (2-31) defines the state vector. Details about the linear system state space model are reviewed in Chapter 3.

$$\begin{bmatrix}
0 & -\omega_e \sin\varphi & -\dot{\varphi} & \omega_e \sin\varphi & 0 & 0 & 0 & -\cos\varphi & 0 & R_{21} & R_{22} & R_{23} & 0 & 0 & 0 \\
\omega_e \sin\varphi & 0 & -\omega_e \cos\varphi & 0 & 0 & 0 & 1 & 0 & 0 & R_{11} & R_{12} & R_{13} & 0 & 0 & 0 \\
\dot{\varphi} & \omega_e \cos\varphi & 0 & -\omega_e \cos\varphi & 0 & 0 & 0 & -\sin\varphi & 0 & R_{31} & R_{32} & R_{33} & 0 & 0 & 0 \\
0 & 0 & 0 & 0 & 0 & 0 & 1 & 0 & 0 & 0 & 0 & 0 & 0 & 0 & 0 \\
0 & 0 & 0 & 0 & 0 & 0 & 0 & 1 & 0 & 0 & 0 & 0 & 0 & 0 & 0 \\
0 & 0 & 0 & 0 & 0 & 0 & 0 & 0 & 1 & 0 & 0 & 0 & 0 & 0 & 0 \\
0 & \frac{-f_u}{R_M} & \frac{f_e}{R_M} & 0_1 & 0 & 0 & 0 & \omega_e \sin\varphi & \frac{-\dot{\varphi}}{R_M} & 0 & 0 & 0 & \frac{R_{21}}{R_M} & \frac{R_{22}}{R_M} & \frac{R_{23}}{R_M} \\
\frac{f_u}{R_E} & 0 & \frac{f_n}{R_M} & 0 & 0 & 0 & 2\omega_e \tan\varphi & 0 & \frac{-2\omega_e}{R_N} & 0 & 0 & 0 & \frac{R_{11}}{R_E} & \frac{R_{22}}{R_E} & \frac{R_{23}}{R_E} \\
-f_e & f_n & 0 & 0 & 0 & c & 2R_M\dot{\varphi} & 2R_E\omega_e \cos\varphi & 0 & 0 & 0 & 0 & R_{31} & R_{32} & R_{33} \\
0 & 0 & 0 & 0 & 0 & 0 & 0 & 0 & 0 & 0 & 0 & 0 & 0 & 0 & 0 \\
0 & 0 & 0 & 0 & 0 & 0 & 0 & 0 & 0 & 0 & 0 & 0 & 0 & 0 & 0 \\
0 & 0 & 0 & 0 & 0 & 0 & 0 & 0 & 0 & 0 & 0 & 0 & 0 & 0 & 0 \\
0 & 0 & 0 & 0 & 0 & 0 & 0 & 0 & 0 & 0 & 0 & 0 & 0 & 0 & 0 \\
0 & 0 & 0 & 0 & 0 & 0 & 0 & 0 & 0 & 0 & 0 & 0 & 0 & 0 & 0 \\
0 & 0 & 0 & 0 & 0 & 0 & 0 & 0 & 0 & 0 & 0 & 0 & 0 & 0 & 0
\end{bmatrix}$$

Figure 2- 10 Dynamic Matrix of INS Error Model (Sun, 1999)

2.3 GPS/INS Integration Schemes and Architectures

The degree of complexity of the integration approach should reflect the mission requirement; it may also be limited by the investment that can be made to obtain these objectives. Integration strategies and mechanisms may be very simple or relatively complex. Generally speaking, the GPS/INS integration schemes have three categories, namely uncoupled mode; loosely coupled mode and tightly coupled mode (Greenspan, 1996). For each category, variations may exist across applications. This section will discuss commonly used integration schemes and their architectures.

2.3.1. Uncoupled Mode

Figure 2-11 illustrates the configuration in which GPS and INS produce independent navigation solutions with no influence of one on the other. $(P\,V)_{GPS}$ are the GPS-derived position, velocity while $(P\,V\,A)_{INS}$ are INS-derived position, velocity and attitude. $(P\,V\,A)_{est}$ are the estimated positions, velocities and attitudes parameters. The integrated navigation solution is mechanized by an external integration processor. It can be as simple as a selector or be as complex as a Kalman filter (Spilker, 1996). A selector is the simplest way to combine these two systems together, and the accuracy of the navigation solution will not be worse than the accuracy of the INS. In the case when a medium to low accuracy IMU is used, the accuracy may be very low. A Kalman filter is a good solution in this case.

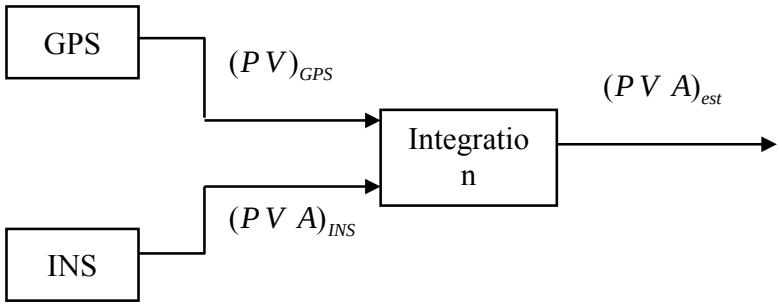

Figure 2-11 Uncoupled Integration Mode

The features of the uncoupled integration method are that it is the easiest, fastest and least expensive way to integrate GPS and INS. Both GPS-only and INS-only navigation solutions are available separately which can provide some tolerance to failures of the subsystem components. It can also provide en-route navigation which is at least as accurate as that available from the INS (Greenspan, 1996).

2.3.2 Loosely Coupled Mode

Inertial navigation systems in principle permit autonomous operation. However, due to their error propagation properties, most applications require high-terminal accuracy. And external aiding is usually utilized to bound the INS errors. Figure 2-12 shows a loosely coupled integrated configuration with a feedback loop (Greenspan, 1996).

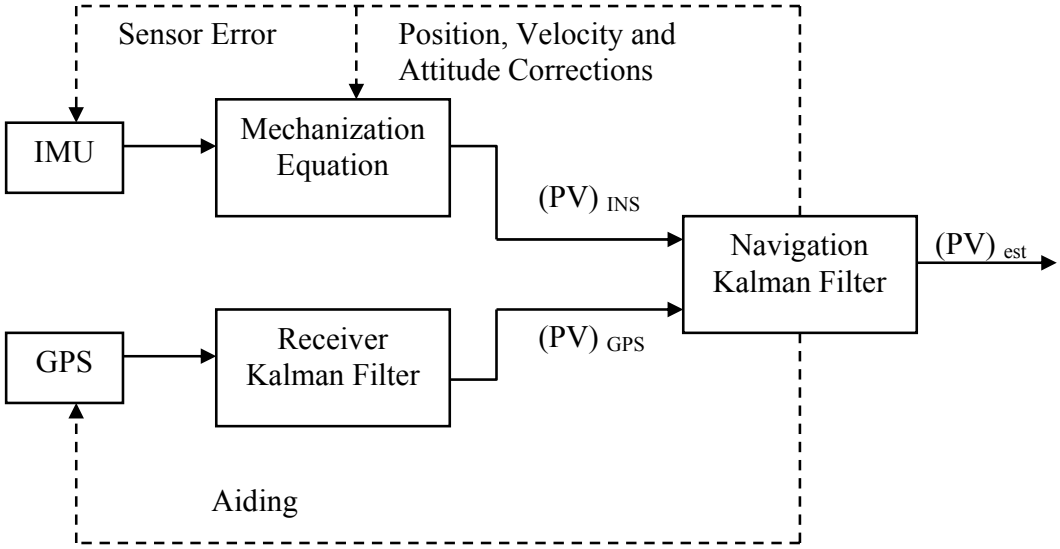

Figure 2-12 Loosely Coupled Integration Approach

In a loosely coupled system, the GPS receiver has its own Kalman filter to process pseudorange or Doppler measurements which are used to calculate positions and velocities. GPS-derived positions and velocities are combined with INS positions and velocities to form the error residuals which are sent to the navigation Kalman filter. This filter corrects the INS in a feedback manner, and the effects of biases and drifts, as well as misalignment errors, will be significantly decreased. The features of a loosely coupled

approach include: (1) it allows maximum use of off-the-shelf hardware and software that can be easily assembled into a cascaded system without major development; and (2) the feedback of the error states to the inertial navigation system will bound the INS errors. This is especially important for medium to low accuracy IMU systems because the feedback loop effectively corrects sensor errors. In addition, the position, velocity and attitude corrections to the INS mechanization equations can be applied at the same time if needed.

According to different applications, a loosely coupled scheme can be implemented in a variety of configurations. Most commonly used are open-loop and closed-loop implementations. Removing all the dashed lines in Figure 2-12 forms an open-loop configuration. All the measurements from GPS (pre-filtered position and velocity) and INS (position and velocity) are processed in the navigation Kalman filter. As there is no feedback, all the measurements are used without pre-correction. Open-loop implementation is straightforward to realize. However, it is only suitable for integration with a high-end inertial sensor and for short-term applications. A medium to low accuracy IMU propagates relatively large navigation errors in a fixed time interval compared with that of a high-end system. If there is no feedback loop to produce the compensation to the inertial sensor and the mechanization equation, the measurements will have higher values that will spoil the linear system assumption. For a closed-loop configuration, feedback is applied from the integration filter to the inertial sensors and/or the mechanization equations. Results from the previous step are used to minimize approximation error. A closed-loop scheme is especially useful when the sensor accuracies are poor. Because medium to low accuracy sensors usually have fast varying error properties, real-time or near real-time estimation and compensation to these errors is very important to improve the accuracy of the navigation solutions from the INS.

A loosely coupled integration approach has been widely used in the past decade because of its high flexibility and performance. For example Cannon et al. (1999) used an open loop, loosely coupled, integration scheme for an airborne decimetre level positioning. INS solutions were used to detect and correct GPS cycle slips and to bridge GPS gaps.

Salychev et al. (2000) used a closed loop, loosely coupled, integration scheme and realized both a low-cost and medium accuracy GPS/IMU integration for attitude determination, which reached an RMS value of 22 to 25 arc-min horizontally when using a low-cost IMU, and an RMS value of 2 to 3 arc-min horizontally when using an medium accuracy IMU. Scherzinger (2001) used a loosely coupled inertial Real Time Kinematic (RTK) aiding, which exported the INS position and variance-covariance matrix to the GPS/INS filtering module in order to accelerate the time to a fix integer ambiguity solution after a GPS outage. The results showed that after a full GPS outage lasting up to 60 seconds, the integer recovery time decreased to 10 to 15 seconds compared of 45 to 100 seconds when no position seed was used.

2.3.3 Tightly Coupled Mode

In a tightly coupled system architecture, separate Kalman filters for the GPS receiver and the navigation process are combined into a single integrated filter. As shown in Figure 2-13, this filter accepts GPS pseudorange and Doppler measurement residuals directly. The filter error states now include the INS error states (position, velocity, attitude, gyro drift, accelerometer bias) as well as new states representing the GPS receiver clock bias and drift. The components of the filter state vector that represent the INS errors are used to calibrate the INS and correct its estimates of position and velocity and the direction cosine matrices (DCM) describing vehicle attitude. The filter estimates of clock bias and drift are used to correct the GPS measurements. An INS-derived estimate of pseudorange and range rate are formed using satellite ephemeris data, INS position and velocity data and estimated GPS receiver clock errors. This predicted pseudorange and Doppler are combined with the receiver output data to form residuals that drive the navigation filter. Outputs from the Kalman filter and the INS can also be used to aid the satellite tracking loops in the GPS receiver.

The tightly coupled architecture more effectively utilizes the available measurements and *a priori* information to determine and correct for system errors in a highly integrated fashion. It can thus yield better performance than the loosely coupled system, providing accurate navigation estimates during periods of high vehicle dynamics or jamming.

Ohlmeryer et al. (2002) applied a tightly coupled GPS/INS configuration to an extended range guided missile system. A positioning accuracy on target of between 1-2 metres circular error of probability (CEP) out to 40 nautical miles in a GPS jamming environment has been achieved. Some of the benefits of a tightly coupled system are: more direct exploitation of the fundamental measurement data, more direct aiding of the receiver tracking process by the filter and INS, a higher likelihood of maintaining firm satellite tracks, and better resiliency to poor satellite geometry, high vehicle dynamics, data dropouts, IMU errors, and jamming.

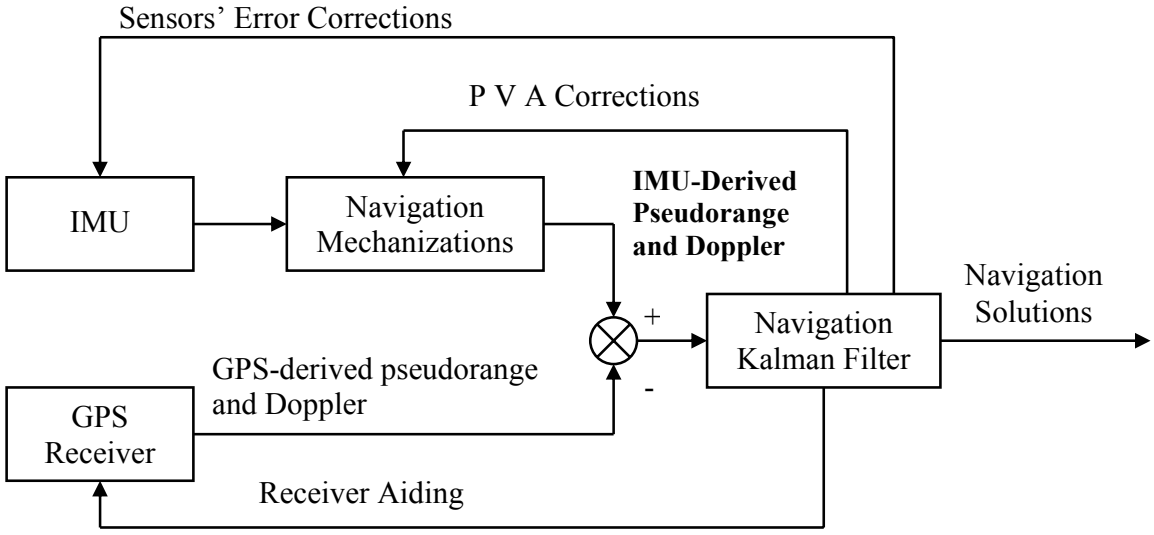

Figure 2-13 Tightly Coupled Integration Scheme

CHAPTER 3

ESTIMATION APPROACHES

In this Chapter, two GPS/INS integration approaches are discussed. The state space approach for error estimation is reviewed. The conventional Kalman filtering algorithm and the adaptive Kalman filtering algorithm, as well as their application to GPS/INS integration, are discussed. As an alternative to a Kalman filter, the wave estimation approach is introduced and its mathematical model is established. Both the Kalman filter and wave estimator will be used to fuse GPS/INS data in the following chapters.

3.1 Kalman Filter Algorithm

The Kalman filter algorithm has been widely used to process the data since it has many advantages over other estimators (e.g. Greenspan, 1996). Kalman filtering offers flexibility such that it can be used in either in a real-time or a post-mission environment. It can also accommodate measurement updates from a wide variety of sensors, GPS in this case. Details of the Kalman filter derivation will not be given here, however, there are numerous references available such as Gelb (1974), Brown (1996) and Grewal et al. (2001).

3.1.1. State Space Model and Kalman Filtering Algorithm

According to linear system theory, the dynamics of a linear system can be represented by a state space model, where a set of first order differential equations express the deviation from a reference trajectory (Liu, 1994):

$$\dot{\mathbf{x}} = \mathbf{F}\mathbf{x} + \mathbf{w} \tag{3-1}$$

$$\mathbf{z} = \mathbf{H}\mathbf{x} + \mathbf{v} \tag{3-2}$$

where $\mathbf{x}$ is an $n \times 1$ state vector

$\mathbf{F}$ is an $n \times n$ system dynamic matrix

$\mathbf{w}$ is an $n \times 1$ system noise vector

$\mathbf{z}$ is an $m \times 1$ observation vector

$\mathbf{v}$ is an $m \times 1$ measurement noise

$\mathbf{H}$ is an $m \times n$ design matrix

m is the number of measurement, and

n is the number of the states.

Equation (3-1) is the dynamic equation and equation (3-2) is the observation equation. Since the implementation of the estimation process is done on a computer, the discrete form is generally more convenient to use. Corresponding to equations (3-1) and (3-2), the discrete system equations are derived as follows:

$$\mathbf{x}_{k+1} = \mathbf{\Phi}_{k+1,k}\mathbf{x}_k + \mathbf{w}_k \tag{3-3}$$

$$\mathbf{z}_k = \mathbf{H}\mathbf{x}_k + \mathbf{v}_k \tag{3-4}$$

where k denotes epoch t_k

$\mathbf{\Phi}$ is the $n \times n$ state transition matrix

$\mathbf{x}_k$ is the state vector at a discrete epoch k

$\mathbf{z}_k$ is the observation vector at a discrete epoch k, and

$\mathbf{w}_k$ and $\mathbf{v}_k$ are system driving noise and observation noise at epoch k.

In a Kalman filter, it is assumed that $\mathbf{w}_k$ and $\mathbf{v}_k$ have white noise characteristics with the following properties (Gelb 1974):

$$\mathbf{E}[\mathbf{w}_k] = \mathbf{0}, \ \mathbf{E}[\mathbf{v}_k] = \mathbf{0},$$

$$\mathbf{E}[\mathbf{w}_i \mathbf{w}_j^T] = \mathbf{Q}\boldsymbol{\delta}_{ij}, \quad \mathbf{E}[\mathbf{v}_i \mathbf{v}_j^T] = \mathbf{R}\boldsymbol{\delta}_{ij}, \quad \mathbf{E}[\mathbf{w}_i \mathbf{v}_i^T] = 0,$$

$$\delta_{ij} = \begin{cases} 1 & i = j \\ 0 & i \neq j \end{cases}$$

where $\mathbf{E}(\bullet)$ is the mathematical expectation.

For a stationary system, the state transition matrix $\mathbf{\Phi}$ is:

$$\mathbf{\Phi} = e^{\mathbf{F}\Delta t} \tag{3-5}$$

and can be approximated by a Taylor series expansion over a short time interval (Zheng, 1998) , Δt . Expanding equation (3-5), and truncating after the first two terms, results in:

$$\mathbf{\Phi} = \mathbf{I} + \mathbf{F}\Delta\mathbf{t} \tag{3-6}$$

where **I** is the identity matrix.

Kalman filtering is a two-step recursive process (Salychev, 1998). The first step is prediction by the system model, i.e.:

$$\hat{\mathbf{x}}_k(-) = \mathbf{\Phi}_{k,k-1}\mathbf{x}_{k-1}(+) \tag{3-7}$$

$$\mathbf{P}_k(-) = \mathbf{\Phi}_{k,k-1}\mathbf{P}_{k-1}(+)\mathbf{\Phi}^T_{k,k-1} + \mathbf{Q}_{k-1} \tag{3-8}$$

and the second step is the measurement update of the system model. The elements of the update process are as follow:
Kalman gain matrix:

$$\mathbf{K}_k = \mathbf{P}_k(-)\mathbf{H}^T_k[\mathbf{H}_k\mathbf{P}_k(-)\mathbf{H}^T_k + \mathbf{R}_k]^{-1} \tag{3-9}$$

Error covariance update:

$$\mathbf{P}_k(+) = [\mathbf{I} - \mathbf{K}_k\mathbf{H}_k]\mathbf{P}_k(-) \tag{3-10}$$

State update:

$$\hat{\mathbf{x}}_k = \mathbf{x}_k(-) + \mathbf{K}_k(\mathbf{z}_k - \mathbf{H}\hat{\mathbf{x}}_k(-)) \tag{3-11}$$

where $\hat{\mathbf{x}}_k$ is the estimated state vector

$\mathbf{\upsilon}_k = \mathbf{z}_k - \mathbf{H}_k\hat{\mathbf{x}}_k(-)$ is the innovation vector

$\mathbf{P}_k$ is the $n \times n$ covariance matrix of the state vector

I is the identity matrix

$\mathbf{R}_k$ is the $m \times m$ covariance matrix of the measurement noise

$\mathbf{K}_k$ is the $n \times m$ Kalman gain matrix, and

$\mathbf{Q}_k$ is the $n \times n$ covariance matrix.

$\mathbf{Q}_k$ can be derived from the integral of the spectral density matrix of the system noise matrix **Q**, i.e. (Maybeck, 1994).

$$\mathbf{Q}_k = \int_0^{\Delta t} \mathbf{\Phi}(\tau)\mathbf{Q}(\tau)\mathbf{\Phi}^T(\tau)d\tau \tag{3-12}$$

The above equation can be simplified as follows, and for details see Wong (1988).

$$\mathbf{Q}_k \approx \mathbf{Q}\Delta t \tag{3-13}$$

A flowchart of the Kalman filter is shown in Figure 3-1.

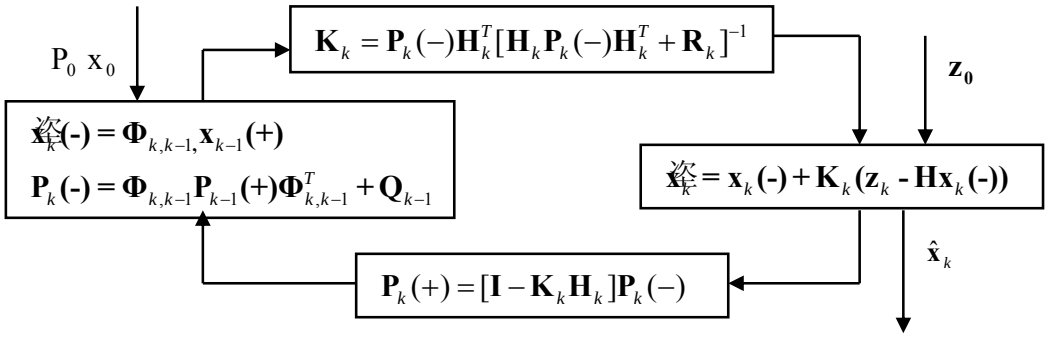

Figure 3-1 Flowchart of a Kalman Filter (Brown, 1994)

$\mathbf{P_0}$ is the initial value of **P** matrix

$\mathbf{x_0}$ is the initial value of the state vector, and

$\mathbf{z_0}$ is the initial value of the measurement vector.

3.1.2. Accuracy of the Kalman Filter

The estimation accuracy depends on the *a priori* information of the system and measurement models, as well as the noise statistics. The estimation error, defined as the difference between the estimates and the true state vector, can be expressed as follows:

$$\tilde{\mathbf{x}}_k = \mathbf{x}_k - \hat{\mathbf{x}}_k \tag{3-14}$$

Substituting the Kalman filtering equations and the system model into equation (3-14) gives:

$$\tilde{\mathbf{x}}_k = (\mathbf{I} - \mathbf{K}_k\mathbf{H})\boldsymbol{\Phi}_k\tilde{\mathbf{x}}_{k-1} - (\mathbf{I} - \mathbf{K}_k\mathbf{H})\mathbf{w}_{k-1} + \mathbf{K}_k\mathbf{v}_k \tag{3-15}$$

Restoring the above equation in reverse time, the estimation error at any epoch, k, can be expressed in terms of the initial errors (Salychev, 1998):

$$\begin{aligned}\tilde{\mathbf{x}}_k = &\left\{\prod_{i=1}^{k}(\mathbf{I} - \mathbf{K}_k\mathbf{H})\boldsymbol{\Phi}\right\}\tilde{\mathbf{x}}_0 \\ &- \sum_{j=0}^{k-2}\left\{\prod_{i=1}^{j}(\mathbf{I} - \mathbf{K}_{k+1-i}\mathbf{H})\boldsymbol{\Phi}\right\}(\mathbf{I} - \mathbf{K}_{k-j}\mathbf{H})\mathbf{w}_{k-j-1} \\ &+ \sum_{j=0}^{k-2}\left\{\prod_{i=1}^{j}(\mathbf{I} - \mathbf{K}_{k+1-i}\mathbf{H})\boldsymbol{\Phi}\right\}\mathbf{K}_{k-j}\mathbf{v}_{k-j}\end{aligned} \tag{3-16}$$

The first component of equation (3-16) shows how the initial estimation error attenuates with time. It has been proven that $\left\|\prod_{i=1}^{k}(\mathbf{I} - \mathbf{K}_k\mathbf{H})\boldsymbol{\Phi}\right\|$ tends to zero over time (Leondes, 1976). The second term shows the influence of input noise, and the last term illustrates the process of measurement noise smoothing. A well-designed Kalman filter will attenuate the initial state errors, and smooth the effects of system and measurement errors through the averaging process.

A priori information

A priori information including the initial value of the state $\mathbf{x}_0$, and the initial error covariance matrix, $\mathbf{P}_0$, will only influence the transit process of a Kalman filter but not the steady state, i.e. theoretically *a priori* information will not affect the estimation optimality of the Kalman filter. However, since the Kalman filter has a sequential convergence property, strongly observed states converge first, weakly observed states, such as the accelerometer and gyro biases, take a longer time to converge (Salychev, 1991). During this period, the estimation errors attenuate slowly, and estimation gives poor results. Therefore, their initial values should be carefully determined through lab calibration tests. At steady state, the Kalman filter provides the estimates with a constant accuracy, which cannot be improved.

Matrix **R** *and* **Q**

The measurement noise covariance matrix, **R,** which describes how well the measurement noise is modeled, is one of the important factors related to the estimation quality. Imperfect modeling may be caused by the non-modeling and/or mis-modeling of the measurement observables, also by ignoring the non-white properties of measurement errors. The system noise covariance, **Q**, which defines the extent to which the prediction should be trusted, is another important factor that affects the estimation quality. The role of the **Q** matrix in a Kalman filter is to define the uncertainty after each prediction step (Mohamed, 1999). A **Q** value that is too large will result in noisy estimates, whereas a **Q** value that is too small will result in a smoother, but biased, estimate. Therefore, a reasonable **Q** matrix value is critical for achieving good estimates.

Innovation sequence

The innovation sequence is defined as the difference between the current measurement vector and the *a priori* estimates, as shown in Salychev (1998):

$$\boldsymbol{\upsilon}_k = \mathbf{z}_k - \mathbf{H}\hat{\mathbf{x}}_k(-) \tag{3-17}$$

Substituting the measurement equation and using the definition in equation (3-14) gives:

$$\boldsymbol{\upsilon}_k = \mathbf{H}\tilde{\mathbf{x}}_k(-) + \mathbf{v}_k \tag{3-18}$$

This shows that the innovation sequence contains information on the *a priori* estimation error, which is corrupted by the measurement noise. The innovation sequence has the following properties: (1) $\boldsymbol{\upsilon}_\mathbf{k}$ is white noise for an optimal Kalman filter. This property can be used to check the optimality of a Kalman filter; (2) the covariance matrix of the innovation sequence is:

$$\mathbf{Y}_k^{-1} = \mathbf{E}[\boldsymbol{\upsilon}_k \boldsymbol{\upsilon}_k^T] = \mathbf{H}\mathbf{P}_k(-)\mathbf{H}^T + \mathbf{R}_k \tag{3-19}$$

where $\mathbf{Y}_\mathbf{k}$ is called the information matrix of innovations (Grewal, 2001), and (3) the likelihood function of the innovation vector is:

$$\mathcal{L}(\boldsymbol{\upsilon}_k) = \exp(-\frac{1}{2}\boldsymbol{\upsilon}_k^T \mathbf{Y}_k \boldsymbol{\upsilon}_k) \tag{3-20}$$

which can be used to check the anomalous sensor data. Alternatively, its equivalent statistics expression is:

$$\chi^2 = \frac{\boldsymbol{\upsilon}_k^T \mathbf{Y} \boldsymbol{\upsilon}_k}{l} \tag{3-21}$$

where l is the dimension of $\boldsymbol{\upsilon}_\mathbf{k}$. Equation (3-21) is non-negative with a minimum value of zero. If the Kalman filter was perfectly designed and all the white noise was Gaussian, this would be a χ^2 distribution. An upper limit threshold value can be determined to detect the anomalous sensor data (Grewal, 2001).

The innovation sequence also plays an important role in the innovation-based adaptive estimation (IAE) algorithm. This will be discussed in the next section. It can also be used as an indicator of the real estimation errors. In practice, there is usually a gap between the theoretical estimation error (expressed by the covariance matrix of the estimation error, $\mathbf{P}_\mathbf{k}$) and the real one. This is caused by the imperfection of the mathematical description of the applied system model.

Accuracy limit of Kalman filter

According to Salychev (1998), the steady state value of the estimation error covariance matrix is:

$$\mathbf{P}_{st} = \mathbf{A}(\boldsymbol{\Phi}\mathbf{A})^{n+1}\mathbf{A}\mathbf{P}_{st}(\boldsymbol{\Phi}^T)^{n+1} + \mathbf{A}\sum_{i=1}^{n}(\boldsymbol{\Phi}\mathbf{A})^i \mathbf{Q}(\boldsymbol{\Phi}^T)^i \tag{3-22}$$

where $\mathbf{A} = \mathbf{I} - \mathbf{K}_{st}\mathbf{H}$ and $\mathbf{P}_{st}, \mathbf{K}_{st}$ are the steady state of $\mathbf{P}_k$ and $\mathbf{K}_k$ respectively.

It is clear that the first term attenuates over time. The second term will tend to a steady value, which depends on the level of the system noise, i.e. the level of the system uncertainty restricts the estimation accuracy.

3.1.3. Kalman Filter Configuration Implemented

An open loop loosely coupled GPS/INS integration scheme has been selected for this research because a loosely coupled scheme has the advantages of: (1) maximizing the use of the off-shelf products; (2) a relatively simple mathematical model; (3) robust navigation solutions; and (4) provision of INS predicted positions and velocities during GPS outages. Details have been discussed in Section 2.3.2. The system model is described in equations (2-30) and (2-31) and Figure 2-11. The measurement equation is:

$$\mathbf{z}_k = \begin{bmatrix} \mathbf{P}_{\mathbf{INS}} - \mathbf{P}_{\mathbf{GPS}} \\ \mathbf{V}_{\mathbf{INS}} - \mathbf{V}_{\mathbf{GPS}} \end{bmatrix} \tag{3-23}$$

and the measurement covariance matrix is:

$$\mathbf{R}_k = diag(\sigma_\varphi^2 \ \sigma_\lambda^2 \ \sigma_h^2 \ \sigma_{v_n}^2 \ \sigma_{v_e}^2 \ \sigma_{v_h}^2) \tag{3-24}$$

Details will be discussed in Chapters 4 and 5.

3.2 Adaptive Kalman Filter

As discussed in Section 3.1, the estimation accuracy of a conventional Kalman filter depends on the *a priori* knowledge of the system model and the noise statistics. If this knowledge is not successfully accurate, the estimation accuracy will be degraded. Adapting the filter covariance matrices **R** and/ or **Q** is one of the remedies to solve the above issue. There are two different implementations of the adaptive Kalman filter. One is the multiple model adaptive estimation (MMAE) while the other is an innovation-based adaptive estimator (IAE) (Mohamed, 1999).

3.2.1. Multiple Model Adaptive Estimation (MMAE)

In the MMAE approach, a bank of Kalman filters runs in parallel using different models for the statistical filter information matrices, **R** and/or **Q**. The structure of each filter and the bank of filters are shown in Figures 3-2 and 3-3, respectively (Mohamed, 1999).

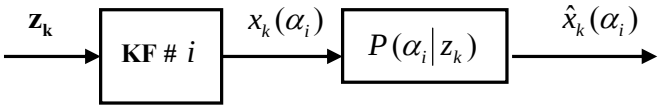

Figure 3- 2 #i Kalman filter in a MMAE

In Figure 3-2, α_i and $P(\alpha_i)$ are the unknown random variable and its known statistical distribution respectively, and in Figure 3-3 l is the total number of filters.

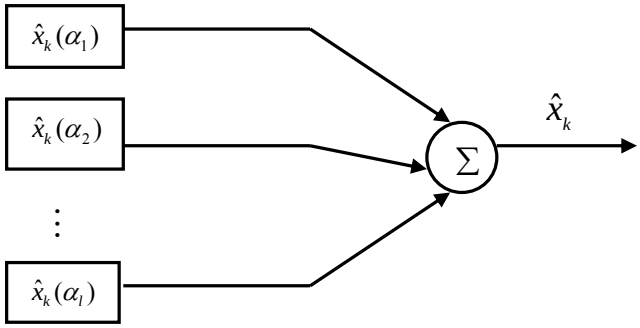

Figure 3- 3 Structure of MMAE

At each recursive step, the adaptive filter performs the following:

(1) According to its own statistic model, each filter will calculate its estimates $\hat{x}_k(\alpha_i)$.

(2) Compute the *a posteriori* probabilities for each hypothesis.

(3) Form the adaptive estimates of **x** as a weighted sum of the estimates from each individual Kalman filter:

$$\hat{\mathbf{x}}_k = \sum_{i=1}^{l} x_k(\boldsymbol{\alpha}_i) P(\alpha_i | z_k) \tag{3-25}$$

In the above equation $\mathbf{P}(\boldsymbol{\alpha}_i | \mathbf{z}_k)$ is the weight of the i^{th} filter when measurements $\mathbf{z}$ up to epoch k are available. As measurements evolve with time, the adaptive scheme learns which of the filters is the correct one, and its weight will approach unity while others

approach zero. The bank of filters accomplishes this by investigating the sums of the weighted squared measurement innovation vector or the so-called residuals. The estimates of the filter with the smallest sum receives the highest weight and prevail.

3.2.2.Innovation-Based Adaptive Estimator (IAE)

The IAE approach (Maybeck, 1994; Salychev, 1998) adapts the $\mathbf{R}_k$ and/or $\mathbf{Q}_k$ matrices. Based on the whiteness of the filter innovation sequence, $\mathbf{R}_k$ and $\mathbf{Q}_k$ matrices are adapted as follows:

$$\hat{\mathbf{R}}_k = \hat{\mathbf{C}}_k - \mathbf{H}\mathbf{P}_k(-)\mathbf{H}^T \tag{3-26}$$

$$\hat{\mathbf{Q}}_k = \mathbf{K}_k\mathbf{C}_k\mathbf{K}_k^T \tag{3-27}$$

In the above equation, $\hat{\mathbf{Q}}_k$ and $\hat{\mathbf{R}}_k$ are the estimated values of $\mathbf{Q}$ and $\mathbf{R}$ matrices, and $\hat{\mathbf{C}}_k$ is the calculated covariance matrix of the innovation sequence at epoch k, which can be calculated as follows:

$$\hat{\mathbf{C}}_k = \frac{k-1}{k}\mathbf{C}_{k-1} + \frac{1}{k}\boldsymbol{\upsilon}_k\boldsymbol{\upsilon}_k^T \tag{3-28}$$

The IAE approach adds little computational complexity to the GPS/INS integration algorithm. Based on a number of computer runs of different GPS/INS datasets, the time increased for the computation of the adaptive block in the IAE approach does not exceed 5% of the original processing time of the conventional Kalman filter (Mohamed, 1999). Compared with the MMAE approach, considerable time saving is achieved, therefore IAE approach is more suitable for application to GPS/INS integration. The calculation schemes of the adaptive algorithm for an unknown **R**-only and unknown **Q-**only are shown in Figure 3-3 and Figure 3-4. For a detailed derivation, refer to Salychev (1998) and Mohamed (1999).

3.2.3 Application of IAE to Loosely Coupled GPS/INS

As discussed in the last section, the IAE approach has its advantages in application to a loosely coupled GPS/INS integrated system. An adaptive **Q** method is used in this research. While the measurement noise covariance matrix, **R**, is kept constant, the system

noise covariance matrix, **Q**, is estimated adaptively. As the system under investigation is stationary, the adapted result will provide more accurate knowledge of the system noise, hence the estimation accuracy should be improved. These results will be shown in Chapter 5.

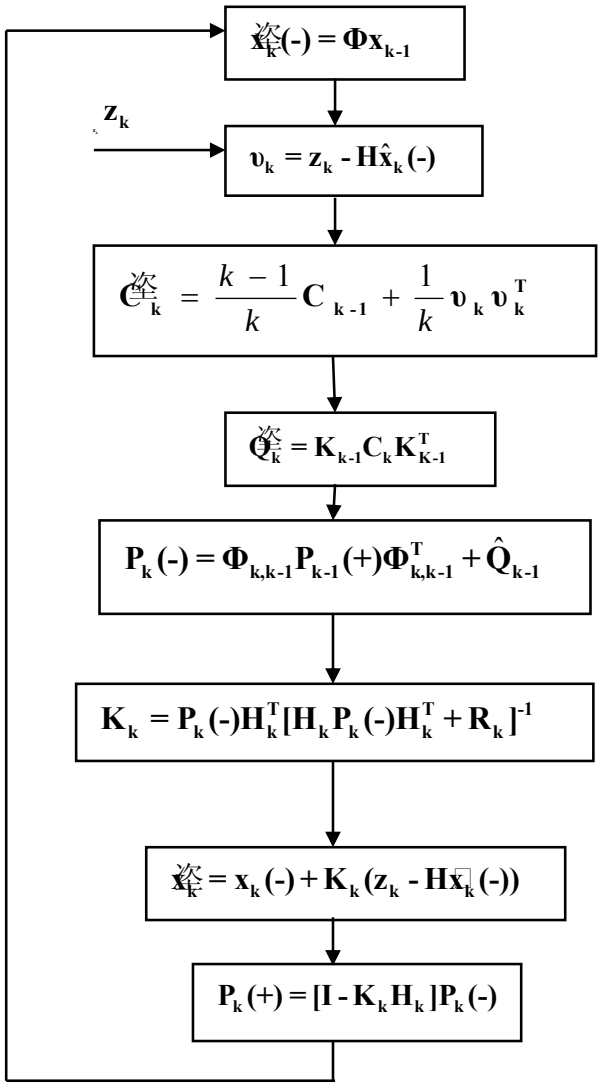

Figure 3- 4 Flowchart for Adaptive R Matrix Only Method

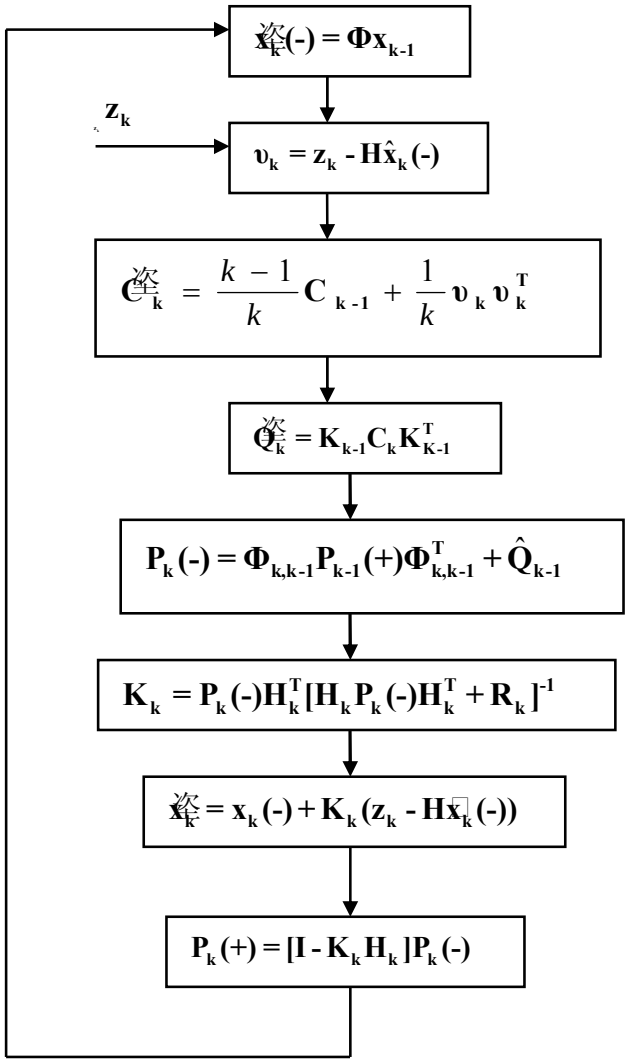

Figure 3-5 Flowchart for Adaptive Q Matrix Only Method

3.3 Wave Estimator

3.3.1 The Methodology

In a conventional Kalman filter, the input noise in equation (3-1) is white or coloured and is described by expectations and variances. In reality, some noise processes have a discernible waveform, which can be described by deterministic means over a short time. Typical examples are shown in Figure 3-6. The wave estimation technique is based on this principle and the wave process can be expressed as follows (Salychev, 1998):

$$w(t) = c_1 f_1(t) + c_2 f_2(t) + ... + c_n f_n(t) \tag{3-29}$$

where

$f_i(t)$ are known base functions, and

$c_i(t)$ are unknown coefficients which vary from one instant to the next.

For example, the disturbances shown in equation (3-29) can be given as: $w(t) = c_1$ and $w(t) = c_1 + c_2 t$, respectively.

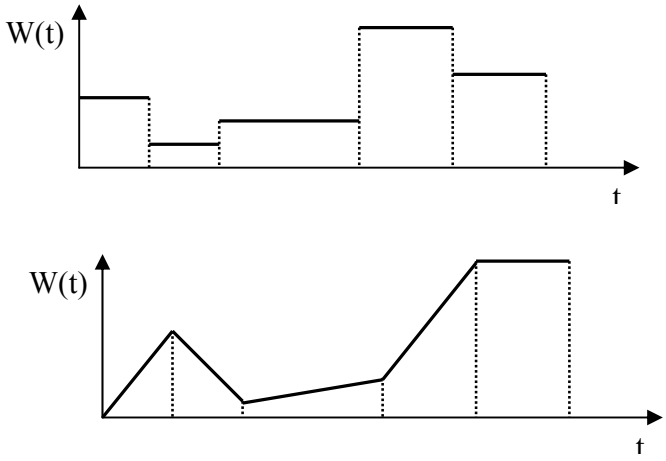

Figure 3-6 System Noise Waveform Examples

The coefficients appear random with respect to time and value, and they change in a piecewise manner. In order to represent $w(t)$ in state space, equation (3-29) can be rewritten in differential equation form with Dirac functions as input:

$$\frac{d^i w(t)}{dt^i} + r_i \frac{d^{i-1} w(t)}{dt^i} + \cdots + r_1 w(t) = \delta(t) \tag{3-30}$$

Equation (3-30) now can be written in state variable form with (Liu, 1992):

$$x_1 = w(t)$$

$$\dot{x}_1 = x_2 + \delta_1(t)$$
$$\dot{x}_2 = x_3 + \delta_2(t)$$
$$\cdots\cdots$$
$$\dot{x}_i = -r_1 x_1 - r_2 x_2 - \cdots\cdots - r_i x_i + \delta_i(t)$$

or in matrix notation

$$\dot{\mathbf{x}} = \mathbf{A}\,\mathbf{x} + \boldsymbol{\delta} \tag{3-31}$$

where $\delta_1(t), \delta_2(t) \cdots\cdots \delta_i(t)$ are Dirac impulse functions with unknown intensity. Equation (3-31) can be expressed in the following discrete form:

$$\mathbf{x}_k^* = \boldsymbol{\Phi}^* \mathbf{x}_{k-1}^* + \boldsymbol{\delta}_{k-1}^{0*} \tag{3-32}$$

where $\boldsymbol{\delta}_{k-1}^{0*}$ is the analogue of a series of Dirac functions of unknown density

i.e. $\delta = \lim_{T \to 0} \frac{\delta^{0*}}{T}$, and

$\mathbf{x}_k^*$ are disturbance states.

Physically, $\boldsymbol{\delta}_{k-1}^{0*}$ is a pulse sequence with unknown value.

Equation (3-30), which describes the disturbance acted on the linear dynamic system, can be added to the original systems shown in equation (3-1) to represent a linear system as:

$$\begin{bmatrix} \mathbf{x}_k \\ \mathbf{x}_k^* \end{bmatrix} = \begin{bmatrix} \boldsymbol{\Phi}_{11} & \boldsymbol{\Phi}_{12} \\ \mathbf{0} & \boldsymbol{\Phi}_{22}^* \end{bmatrix}_{k,k-1} \begin{bmatrix} \mathbf{x}_{k-1} \\ \mathbf{x}_{k-1}^* \end{bmatrix} + \boldsymbol{\delta}_{k-1}^* \tag{3-33}$$

The values of δ_{k-1}^* are assumed to change at an equal time interval NT, which is called a wave cycle; where N is an integer and T is the sampling time. Equation (3-31) is different from equation (3-1) in that though random in nature, the input pulse sequence is deterministic within one wave cycle and can be estimated. Equation (3-31) and the measurement equation (3-2) form the mathematical model for the estimation problem, which is similar to the Kalman filtering algorithm and can be solved by a set of recursive formulas.

Assume that the initial value of the state vector is $\mathbf{x}_0 = 0$. This is not a stringent restriction since the unknown initial values of the state vectors may be taken into account by a proper selection of the vector $\boldsymbol{\delta}_0$. In order to estimate the state vector in the first time interval of N time steps, the initial value of the vector $\boldsymbol{\delta}$ must be determined. Assuming that **H** is constant, for the first cycle, substituting equation (3-31) N times into equation (3-2) the following can be achieved:

$$\begin{aligned}
&\mathbf{z}_1 = \mathbf{H}\mathbf{x}_1 + \mathbf{v}_1 = \mathbf{H}\boldsymbol{\Phi}_{1,0}\mathbf{x}_0 + \mathbf{H}\boldsymbol{\delta}_0 + \mathbf{v}_1 \\
&\mathbf{z}_2 = \mathbf{H}\mathbf{x}_2 + \mathbf{v}_2 = \mathbf{H}\boldsymbol{\Phi}_{2,0}\mathbf{x}_0 + \mathbf{H}\boldsymbol{\Phi}_{2,1}\boldsymbol{\delta}_0 + \mathbf{v}_2 \\
&\cdots\cdots \\
&\mathbf{z}_N = \mathbf{H}\mathbf{x}_N + \mathbf{v}_N = \mathbf{H}\boldsymbol{\Phi}_{N,0}\mathbf{x}_0 + \mathbf{H}\boldsymbol{\Phi}_{N,1}\boldsymbol{\delta}_0 + \mathbf{v}_N
\end{aligned} \tag{3-34}$$

By introducing an auxiliary vector **s**, which satisfies the following recursive equation:

$$\mathbf{s}_{k+1} = \boldsymbol{\Phi}_{k,k-1}\mathbf{s}_k \tag{3-35}$$

with $\mathbf{s}_1 = \boldsymbol{\delta}_0$ k=1,2,…N-1, and $\mathbf{x}_0 = \mathbf{0}$, the following measurement equation is formed:

$$\mathbf{z}_k = \mathbf{H}\,\mathbf{s}_k + \mathbf{v}_k \tag{3-36}$$

Equations (3-33) and (3-34) form a conventional Kalman filtering mathematical model for the estimation of auxiliary vector **s**:

$$\hat{\mathbf{s}}_{k+1} = \boldsymbol{\Phi}_{k+1,k}\mathbf{s}_k + \mathbf{K}_{k+1}(\mathbf{z}_{k+1} - \mathbf{H}\boldsymbol{\Phi}_{k+1,k}\hat{\mathbf{s}}_k) \tag{3-37}$$

with $\hat{\mathbf{s}}_1 = \mathbf{0},\ k = \mathbf{1,2},.....N-1,$ and

$$\begin{aligned}
&\mathbf{P}_{k+1}(-) = \boldsymbol{\Phi}_{k+1,\mathbf{k}}\mathbf{P}_k(+)\boldsymbol{\Phi}^T_{k+1,k} \\
&\mathbf{K}_{k+1} = \mathbf{P}_{k+1}(-)\mathbf{H}^T[\mathbf{H}\mathbf{P}_{k+1}(-)\mathbf{H}^T + \mathbf{R}_{k+1}]^{-1} \\
&\mathbf{P}_{k+1} = (\mathbf{I} - \mathbf{K}_{k+1}\mathbf{H})\mathbf{P}_{k+1}(-)
\end{aligned}$$

where $\mathbf{P}_k = \mathbf{E}[\mathbf{s}_k\mathbf{s}_k^{\mathbf{T}}]$ is the $n \times n$ variance matrix of **s**, and

$\mathbf{R}_k = \mathbf{E}[\mathbf{v}_k\mathbf{v}_k^{\mathbf{T}}]$ is the $m \times m$ variance matrix of measurement noise.

At the end of the wave cycle, the estimation of $\mathbf{x_N}$ is simply:

$$\hat{\mathbf{x}}_N = \hat{\mathbf{s}}_N \tag{3-38}$$

In the second wave cycle (with N time steps) from t= (N+1)T to t= 2NT, a new unknown value of δ_1 appears at the instant k=N, which will affect the value of $\hat{\mathbf{x}}_{\mathbf{N+1}}$. The observation equation in this cycle can be expressed as follows:

$$\begin{aligned}
&\mathbf{z}_{N+1} = \mathbf{H}\mathbf{x}_{N+1} + \mathbf{v}_{N+1} = \mathbf{H}\boldsymbol{\Phi}_{N+1,N}\mathbf{x}_N + \mathbf{H}\boldsymbol{\delta}_1 + \mathbf{v}_{N+1} \\
&\mathbf{z}_{N+2} = \mathbf{H}\mathbf{x}_{N+2} + \mathbf{v}_{N+2} = \mathbf{H}\boldsymbol{\Phi}_{N+2,N}\mathbf{x}_N + \mathbf{H}\boldsymbol{\Phi}_{N+2,N+1}\boldsymbol{\delta}_1 + \mathbf{v}_{N+2} \\
&\cdots\cdots \\
&\mathbf{z}_{2N} = \mathbf{H}\mathbf{x}_{2N} + \mathbf{v}_{2N} = \mathbf{H}\boldsymbol{\Phi}_{2N,N}\mathbf{x}_N + \mathbf{H}\boldsymbol{\Phi}_{2N,N+1}\boldsymbol{\delta}_1 + \mathbf{v}_{2N}
\end{aligned} \tag{3-39}$$

Similar to the method used in the first wave cycle, the auxiliary vector $\mathbf{s_k}$ is introduced as shown in equation (3-33):

$$\mathbf{s}_{k+1} = \boldsymbol{\Phi}_{k,k-1}\mathbf{s}_k$$

with $\mathbf{s_{N+1}} = \boldsymbol{\delta}_1$, k=N+1, N+2,…2N-1. Rearranging the observation equation, the following measurement equation is obtained:

$$\begin{aligned}
&\mathbf{z}^*_{N+1} = \mathbf{z}_{N+1} - \mathbf{H}\boldsymbol{\Phi}_{N+1,N}\mathbf{x}_N = \mathbf{H}\mathbf{s}_{N+1} + \mathbf{v}^*_{N+1} \\
&\mathbf{z}^*_{N+2} = \mathbf{z}_{N+2} - \mathbf{H}\boldsymbol{\Phi}_{N+2,N}\mathbf{x}_N = \mathbf{H}\mathbf{s}_{N+2} + \mathbf{v}^*_{N+2} \\
&\cdots\cdots \\
&\mathbf{z}^*_{2N} = \mathbf{z}_{2N} - \mathbf{H}\boldsymbol{\Phi}_{2N,N}\mathbf{x}_N = \mathbf{H}\mathbf{s}_{2N} + \mathbf{v}^*_{2N}
\end{aligned} \tag{3-40}$$

where

$$\mathbf{v}^*_{N+i} = \mathbf{v}_{N+i} + \mathbf{H}\boldsymbol{\Phi}_{N+i,N}(\mathbf{x}_N - \hat{\mathbf{x}}_N) \tag{3-41}$$

The Kalman filter now has the initial condition $\mathbf{s_{N+1}} = \mathbf{0}$. The measurement noise covariance matrix **R** is:

$$\mathbf{R}_{N+i} = \mathbf{E}[\mathbf{v}^*_{N+i}\mathbf{v}^{*T}_{N+i}] = \mathbf{R}^0_{N+i} + \mathbf{H}\boldsymbol{\Phi}_{N+i,N}\mathbf{P}_N\boldsymbol{\Phi}^T_{N+i,N}\mathbf{H}^T \tag{3-42}$$

where

$$\mathbf{R}_{N+i}^{0} = \mathbf{E}[\mathbf{v}_{N+i}\mathbf{v}_{N+i}^{T}] \tag{3-43}$$

$$\mathbf{P}_{N+1} = \mathbf{E}[\mathbf{s}_{N+1}\mathbf{s}_{N+1}^{T}] \tag{3-44}$$

At the end of this cycle is the following:

$$\hat{\mathbf{x}}_{2N} = \mathbf{\Phi}_{2N,N}\mathbf{x}_{N} + \hat{\mathbf{s}}_{2N} \tag{3-45}$$

When it is necessary to restore the estimates between cycle point N, 2N,…., the following formulas can be used:

$$\begin{aligned}
&\hat{\mathbf{x}}_{N+1} = \mathbf{\Phi}_{N+1,N}\mathbf{x}_{N} + \hat{\mathbf{s}}_{N+1} \\
&\hat{\mathbf{x}}_{N+2} = \mathbf{\Phi}_{N+2,N}\mathbf{x}_{N} + \hat{\mathbf{s}}_{N+2} \\
&\hat{\mathbf{x}}_{N+3} = \mathbf{\Phi}_{N+3,N}\mathbf{x}_{N} + \hat{\mathbf{s}}_{N+3} \\
&\cdots\cdots
\end{aligned} \tag{3-46}$$

where

$$\begin{aligned}
&\hat{\mathbf{s}}_{2N-1} = \mathbf{\Phi}_{2N-1,2N}\mathbf{s}_{2N} \\
&\hat{\mathbf{s}}_{2N-2} = \mathbf{\Phi}_{2N-2,2N-1}\mathbf{s}_{2N-1} = \mathbf{\Phi}_{2N-1,2N}\mathbf{s}_{2N} \\
&\cdots\cdots \\
&\hat{\mathbf{s}}_{N+1} = \mathbf{\Phi}_{N+1,N+2}\mathbf{s}_{N+2} = \mathbf{\Phi}_{N+1,2N}\mathbf{s}_{2N}
\end{aligned} \tag{3-47}$$

The main advantage of wave estimation is that despite estimating within a wave cycle by a set of Kalman filter equations, the auxiliary vector **s** is estimated as described by equation (3-33) with zero input noise. It is well known that the estimated error covariance matrix is determined by the level of the input noise. When there is no input noise, the estimated error covariance matrix tends to zero. The following sub-section will give a detailed analysis of the accuracy of a wave estimator.

3.3.2 Accuracy Analysis

Assume that the system being considered here is time independent, i.e. $\mathbf{\Phi}_{k,k-1} = \mathbf{\Phi}$. In addition, define the error vector as follows:

$$\tilde{\mathbf{x}}_k = \mathbf{x}_k - \hat{\mathbf{x}}_k \tag{3-46}$$

At the end of an arbitrary wave cycle, k

$$\begin{aligned} \tilde{\mathbf{x}}_{k+N} &= (\mathbf{I} - \mathbf{K}_{k+N-1}\mathbf{H})\boldsymbol{\Phi}\tilde{\mathbf{x}}_{k+N-1} - \mathbf{K}_{k+N}\mathbf{v}^*_{k+N} \\ &= \left\{\prod_{i=1}^{N}(\mathbf{I} - \mathbf{K}_{k+N+1-i}\mathbf{H})\boldsymbol{\Phi}\right\}\tilde{\mathbf{x}}_k - \mathbf{K}_{k+N}\mathbf{v}^*_{k+N} \end{aligned} \tag{3-47}$$

The first term of the equation represents the contribution of the initial estimate error at the beginning of each wave cycle, and the second term is the effect of the measurement noise. The norm of the first term tends to zero as N increases, i.e. the estimation error tends to zero at the end of each wave cycle. As mentioned previously, instead of describing the system noise by a statistical model, the wave estimator uses a pseudo-random model to describe the system noise, and the estimation result is good when the model adequately fits the real disturbance. For the effect of measurement noise, it will remain at the same level as that in the case of a conventional Kalman filter.

3.3.2 Application of a Wave Estimator to GPS/INS Integration

The major error sources in an inertial navigation system are the inertial sensor errors. According to the analysis in Chapter 2, gyro drifts and accelerometer biases are modeled as white-noise processes. From classical INS theory, the gyro drift can be observed through the accumulation of information about the angular velocity, but the accelerometer biases are unobservable (Salychev, 1998). It will not make a significant difference if they are not included in the system model. For the filed data set used in this research, the convergence analysis for the Kalman filter shows that all the state vectors converge within 120 seconds except for accelerometer biases (Zhang, 2001). In order to simplify the problem, a sub-optimal model is selected where the accelerometer biases are eliminated which will not make a lot of difference over a short time span. The gyro drifts are modeled as straight lines within each cycle, i.e.:

$$\begin{aligned} \delta\omega_E &= c_0 + c_1 t \\ \delta\omega_N &= d_0 + d_1 t \end{aligned} \tag{3-48}$$

Rewriting equation (3-48) in state space form gives:

$$\begin{aligned} \dot{x}_1 &= \delta\dot{\omega}_E = x_2 + \delta_1 \\ \dot{x}_2 &= \delta_2 \\ \dot{x}_3 &= \delta\dot{\omega}_N = x_4 + \delta_3 \\ \dot{x}_4 &= \delta_4 \end{aligned} \tag{3-49}$$

Adding equation (3-49) into system equations, with the state transition matrix modified by the elimination of the accelerometer biases, a system model suitable for the wave algorithm is obtained.

3.4 Summary

This Chapter reviewed basic estimation approaches, i.e. conventional Kalman filtering, innovation-based adaptive Kalman filtering, as well as the wave estimation approach. Their advantages and disadvantages were discussed and the possibilities to apply these estimation methods to a loosely coupled GPS/INS integrated navigation system were analyzed. According to the above discussions, a brief summary is given as follow:

1. Kalman filtering offers flexibility such that it has been widely used to process the GPS/INS data in the last decade, and it can also been used in either a real-time or a post-mission environment. However, its estimation accuracy depends on the *a priori* information of the system and measurement models, as well as noise statistics. Lack of this information will degrade the estimation accuracy.

2. Adapting the filter covariance matrices **R** and/or **Q** is one of the remedies to achieving a better knowledge of the *a priori* information. IAE method adapts the $\mathbf{R_k}$ and/or $\mathbf{Q_k}$ matrices based on the whiteness of the filter innovation sequence. Compared with the MMAE method, it adds little computational complexity to the GPS/INS integration algorithm. An adaptive **Q**-only approach will be used in the following Chapters in order to improve the estimation accuracy of the navigation Kalman filter.

3. Wave estimation is a relatively new estimation method. Instead of using expectation and variance to model the white or coloured noise in a Kalman filter, a wave estimator describes the system noise by a deterministic means over a short time since some of the noise processes have discernible waveforms. Inertial sensor errors have this property. Therefore, the wave estimation method is suitable for low frequency, slow changing noise signals such as sensor errors in a GPS/INS integration system. It provides better estimation accuracy for weakly observed state variables.

4. It is very important to reasonably choose the wave cycle, which is the time within which the system noise can be described by a deterministic model. The estimation results are good if this pseudo-random model adequately fits the real disturbances.

5. Once the mathematical model for the wave estimation has been established, a software package was developed. It contains the following models: (1) Inertial mechanical equation; (2) Conventional Kalman filter; (3) Innovation-based adaptive Kalman filter; and (4) Wave estimation. The input files include IMU raw data as well as GPS position and velocity. A simplified diagram of the data processing flow for this research is shown in Figure 3-7. Green blocks refer to existing hardware / software whereas blue blocks are the software modules developed in this research.

6. GPS position and velocity calculation is provided by another software package: C^3NAVG^2. Details about C^3NAVG^2 will be discussed in the following chapters. The navigation filter block includes three sub-modules: a conventional Kalman filter; an innovation-based adaptive Kalman filter and a wave estimator. According to the users' choice, this system can realize loosely coupled GPS/INS integration via a conventional Kalman filter, a IAE adaptive **Q**-only filter or a wave estimator. These results with be shown and discussed in the following chapters.

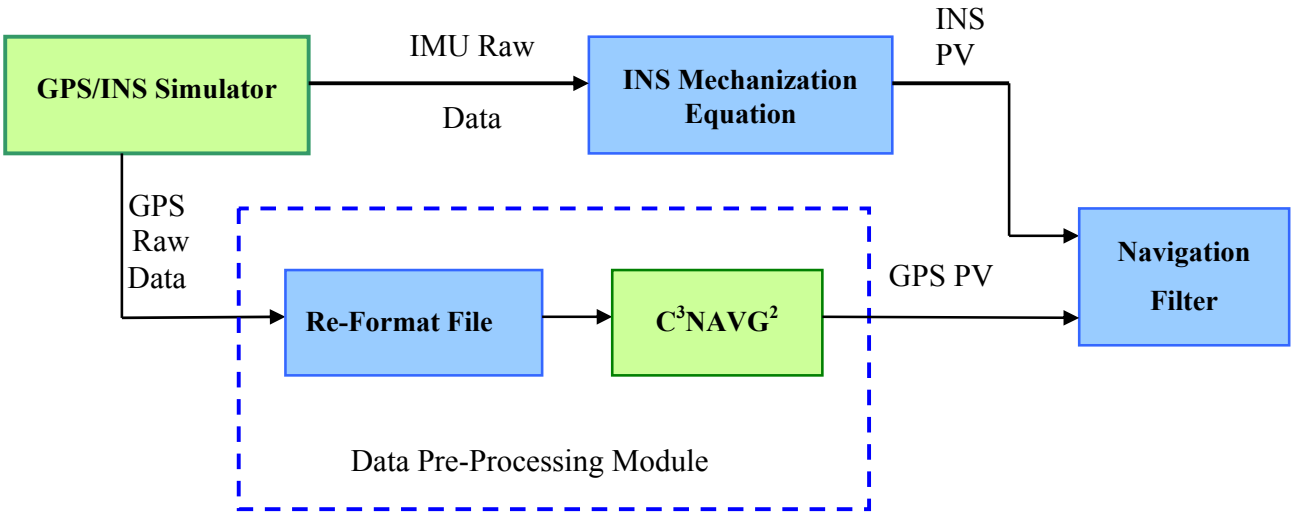

Figure 3-7 Diagram of The GPS/INS Integration System Data Flow

CHAPTER 4

GPS/INS SIMULATION ANALYSIS

As discussed in Chapter 3, a loosely coupled integration scheme has been developed to integrate a medium accuracy IMU with DGPS to achieve metre-level positioning accuracies. Mathematical models for both a Kalman filter and a wave estimator have been developed. In order to evaluate the design and implementation of these estimators, a simulated data set generated by a CastNav 4000 GPS/INS simulator was used to assess both the Kalman filter and wave estimator. The results from both estimators are analyzed. As discussed in Chapter 3, one of the advantages of the wave estimation approach is that it shows improved performance in comparison to a Kalman filter. The improvement is generally in situations where the input disturbances are of low frequency, slow varying in nature, and where there are relatively weak observables in the state vector. This chapter will discuss the accuracy improvement to these weak observables.

4.1 Equipment Setup and Data Files

The simulation system used to produce the GPS/INS data is a CastNav 4000 GPS/INS simulator from CAST Navigation Inc. The CastNav 4000 is a hardware-in-the-loop simulator that generates high fidelity, GPS RF signals commensurate with simulated inertial measurements as inputs to a loosely coupled and/or cascaded GPS/INS system to get real-time navigation solutions. This allows realistic dynamic stimulation in the laboratory environment. It creates a GPS RF and inertial environment for developing, testing, and integrating loosely coupled GPS/INS systems. The system offers dynamic manoeuvring capability with full control of the GPS constellation and host vehicle parameters. It also provides a data logging block to record the raw data from the GPS simulator and the simulated inertial sensor for post mission processing. A block diagram of the CastNav 4000 is shown in Figure 4-1 (Cast Navigation Inc., 2003). As post mission processing was selected in this research, only the green line connected components were used to generate the GPS/INS raw data.

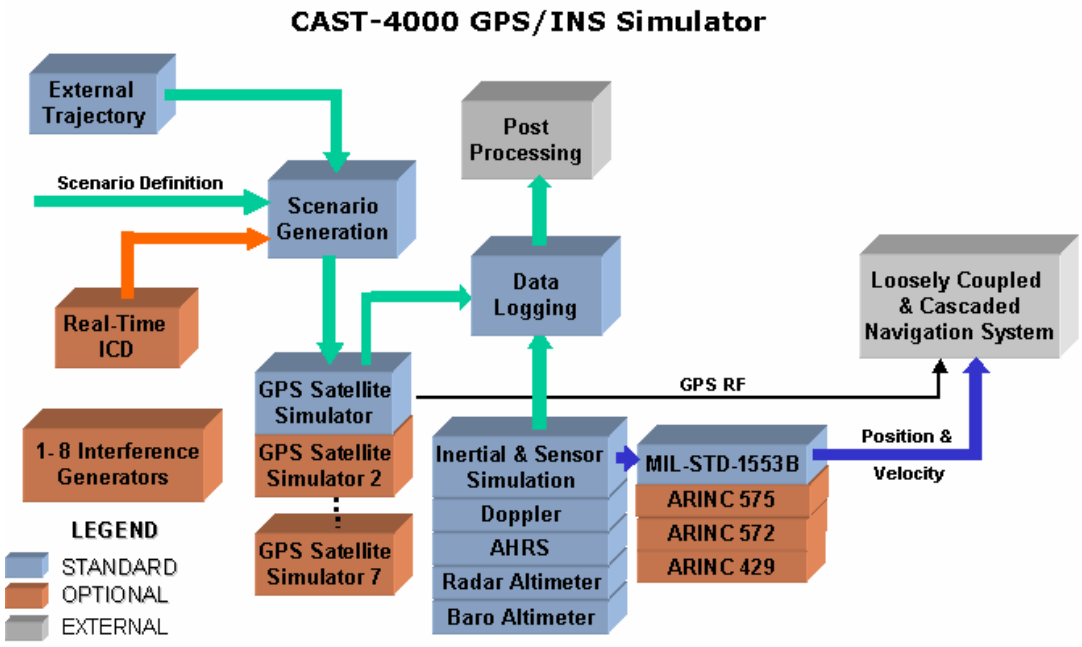

Figure 4- 1 Block Diagram of CastNav 4000 GPS/INS Simulator

4.1.1. Data File Descriptions

The raw GPS data produced for this test contains 1 Hz L1 C/A-code pseudorange and Doppler. The simulated IMU raw data are 100 Hz specific force and angular velocity measurements, with coning and sculling compensated. The IMU and GPS data specifications are shown in Tables 4-1 and 4-2 (Cast Inc., 2001).

Table 4-1 IMU Specifications of Simulation Data Set

Accelerometer Parameters		**Gyroscope Parameters**	
Scale factor accuracy (ppm)	300	Scale factor accuracy (ppm)	150
Scale factor linearity (ppm)	500	Scale factor linearity (ppm)	150
Bias (milli-g)	1	Bias (deg/hr)	1
Non-orthogonality (ppm)	100	Non-orthogonality (ppm)	100
Velocity random walk (m/s/$\sqrt{hr}$)	0.0198	Angular random walk (deg /$\sqrt{hr}$)	0.125

Table 4-2 GPS Simulation Data Assumptions

Troposphere Model	Collins Phase III
Ionosphere Model	Extended Klobuchar
Pseudorange Noise	1 m
Doppler Noise	1 cm/s
Multi Path Errors	Not Applied
Data Rate	1 Hz

In Table 4-2, only the troposphere and the ionosphere errors were applied by the GPS/INS simulator. The pseudorange and Doppler noises were added by the author. The Collins Phase III model uses built-in zenith delay and scale height parameters. In this simulated data set, total zenith delay is 2.59 m, and the troposphere scale height is 7282 m. Extended Klobuchar model modified conventional Klobuchar model to make it suitable to high altitude users, including receivers above the ionosphere as well as space based users. As a land vehicle situation was simulated in this test run, the so-called extended Klobuchar model is equivalent to the conventional Klobuchar model in this case.

This simulated data set contains the following data files:

1. Reference trajectory: a text file containing the GPS time tag, three dimensional true position, velocity and acceleration, as well as attitude information.

2. GPS raw data: binary data file contains GPS time tag, L1/L2 C/A-code pseudorange and the Doppler. Satellite ephemeris data is also contained in this file.

3. IMU raw data: binary data file contains IMU time tag, specific force and angular velocity measurements.

4. Reference file of IMU output. It includes specific force, angular velocity measurements and attitude reference values.

From the IMU specifications showed in Table 4-1, it is clear that the IMU is a medium accuracy unit, so it satisfies the requirements of this research.

4.1.2. Data Pre-Processing Module

GPS raw data from the GPS/INS simulator is a binary file, which contains both the observation and the ephemeris information. This data file has to be re-formatted before it can be used as the input of C^3NAVG^{2TM} ,which works in DGPS mode. Through it, the DGPS positions and velocities are obtained. This task is done by the data pre-processing module as shown in Figure 3-7. A detailed description of this module is shown in Figure 4-2. The output of the "Reformatted File" block contains two binary files: GPS raw measurement file, i.e. code pseudorange and Doppler on L1 and ephemeris files. These two binary files are then fed into the "C^3NAVG^{2TM} block". C^3NAVG^{2TM} is a C program that processes GPS and/or GLONASS pseudorange data in both static and kinematic modes (Petovello et al., 1999) This program also allows for carrier smoothing of the pseudorange, differential positioning, and height fixed, etc. The height fixed constrain can be applied in two different ways. One is "always", and the other is when GDOP greater than a pre-set thresh-hold. Single differential between receivers is used in this research. The DGPS results from C^3NAVG^{2TM} are assessed through a comparison with the reference trajectory; details will be given in Section 4.3.

The final output of the data pre-processing model, i.e. the output of the C^3NAVG^{2TM} , is a binary file, which contains GPS positions, velocities and time tags. Together with the output file from the INS mechanization block, which contains the INS derived positions and velocities, the GPS position and velocity file will be sent to the navigation filter block to realize GPS/INS integration. The navigation filter block has three parallel sub-modules: a conventional Kalman filtering module, an IAE adaptive filtering module and a wave estimator module. Switching to any one of these sub-modules can realize a specific navigation filtering approach selected by the users. In this chapter, a conventional Kalman filter and a wave estimator will be realized and the filtering accuracy will be discussed. In the next chapter, an IAE adaptive Kalman filter and a wave

estimator will be used to assess the field test data, and the accuracy of the INS prediction will also be analyzed.

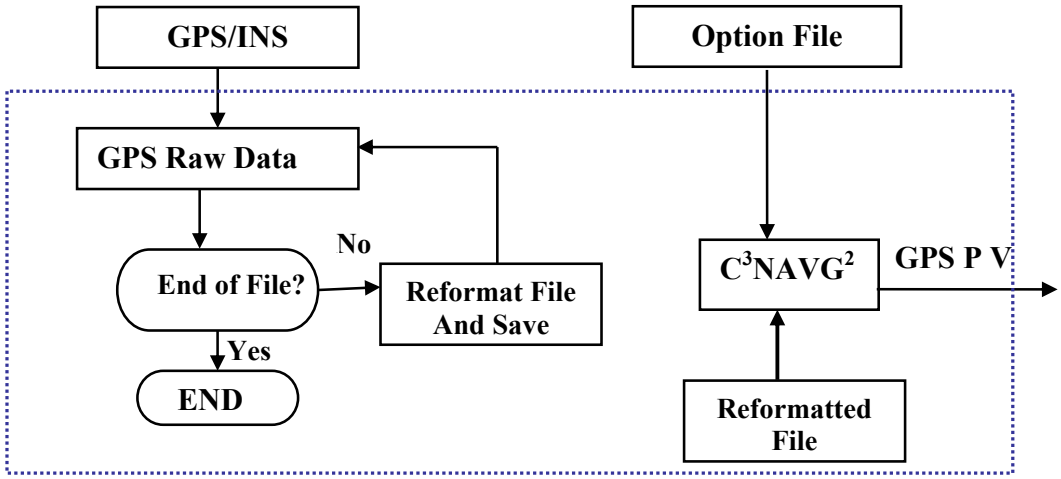

Figure 4-2 Diagram of Data Pre-Formatting Module

4.2 Test Descriptions

As discussed in Section 4.1, GPS observables and ephemeris can be extracted from the GPS raw data file. This binary file contains the dynamics information of both the host vehicle and the GPS satellites at each epoch. The transformed files are then fed into C^3NAVG^{2TM} to get position and velocity. This simulation test was carried out under land vehicle assumptions. Different dynamics were simulated including acceleration, deceleration and turning. A reference file, which contains true positions, velocities and accelerations was produced at the same time. This reference trajectory is used to assess both the C^3NAVG^{2TM} DGPS positions, velocities as well as the navigation filtering results. Figure 4-3 shows the 3-D reference trajectory. It is an 8-turn rectangular-shaped trajectory. The reference station coordinates are as follows (WGS-84):

$$\varphi_0 = 51^{\circ}00.00\ N$$
$$\lambda_0 = -115^{\circ}00.00\ W$$
$$h_0 = 1486.785\ m$$

Figure 4-4 shows the reference positions in latitude and longitude. Figure 4-5 shows the reference velocities. It can be seen that the maximum speed is about 30 m/s, i.e. 108 km/hr. Figure 4-6 shows the reference acceleration. It has a range of +/- 2 m/s^2 that adequately describes the movement of a land vehicle under typical operation.

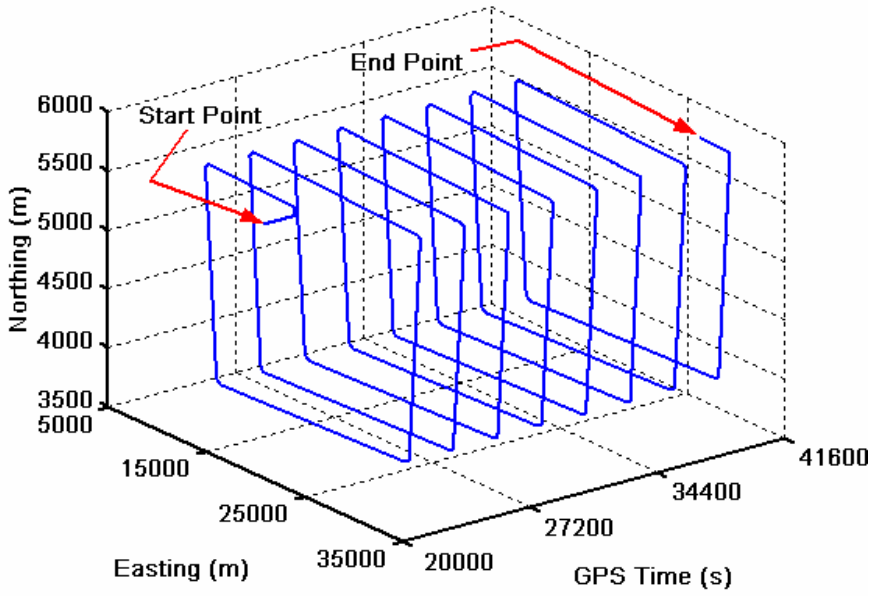

Figure 4- 3 Reference Trajectory of Simulated Data Set

The initial rover position is:

$$\varphi_0 = 51^{\circ}00.00\ N$$
$$\lambda_0 = -115^{\circ}00.00\ W$$
$$h_0 = 1100.00\ m$$

The initial separation between the reference and the rover is 368.785 m vertically. The reference and the rover coordinates coincide horizontally at the initial point. The maximum baseline length is about 22 km during this test run. The simulation test run took 6 hours. Data pre-processing and results assessment will be discussed in the next section.

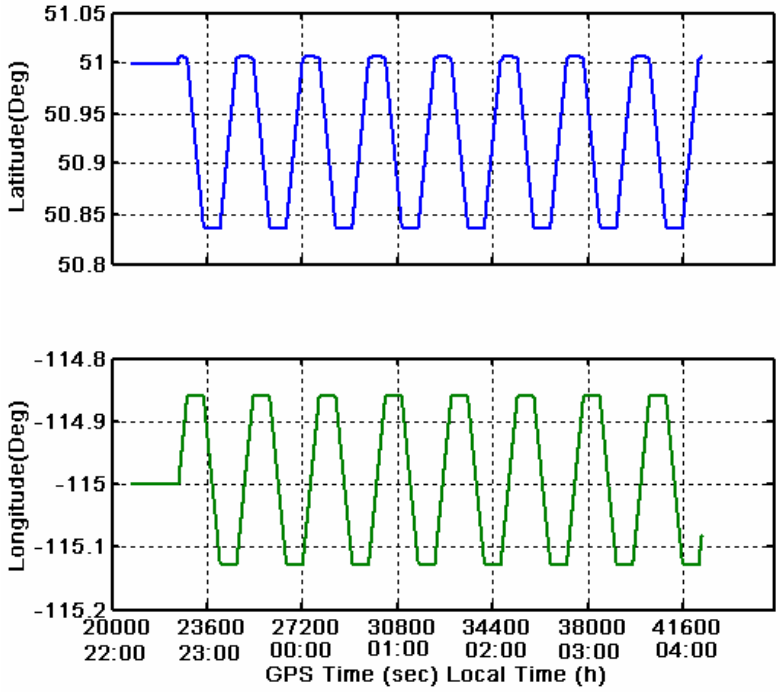

Figure 4- 4 Horizontal Reference Positions versus Time of the Simulation Data Set

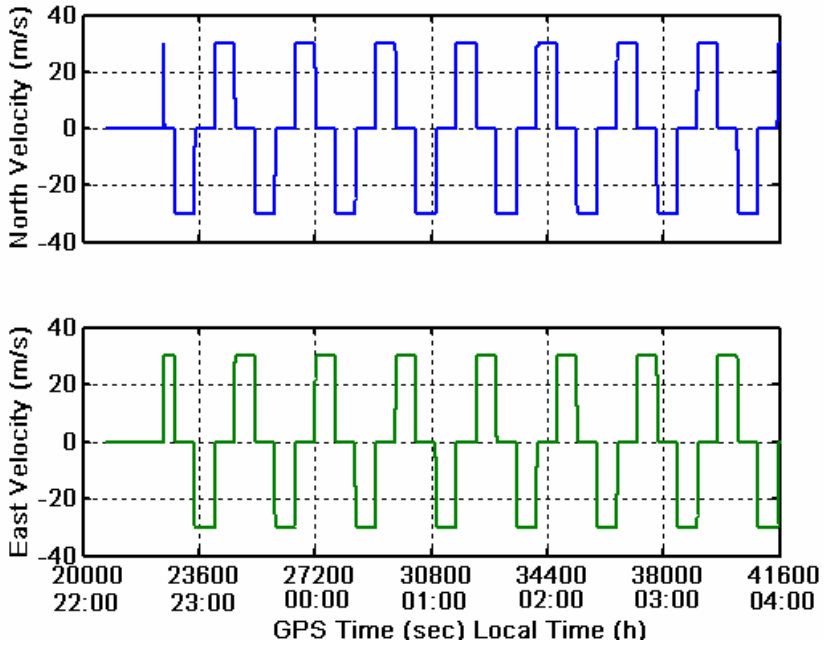

Figure 4- 5 Horizontal Reference Velocities versus Time of the Simulation Data Set

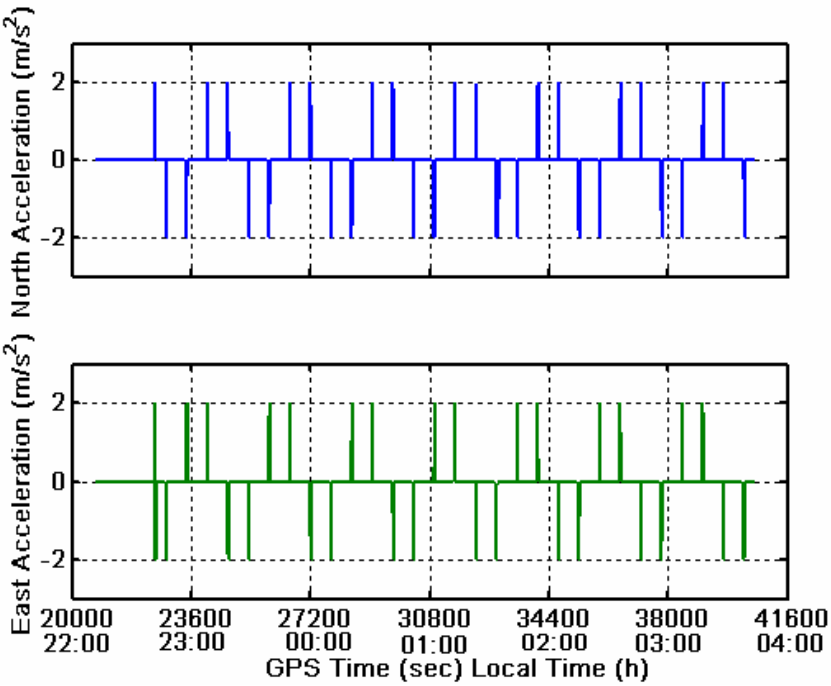

Figure 4- 6 Horizontal Reference Accelerations versus Time of the Simulation Data Set

4.3. Data Pre-Processing

4.3.1 Assessment of DGPS Position and Velocity

One of the objectives of this research is to achieve metre-level positioning results by using position and velocity derived from GPS pseudorange measurements integrating with a medium accuracy IMU. As the CastNav 4000 simulator cannot provide carrier phase measurements, carrier phase smoothing can not be realized; so only raw pseudorange and Doppler are used. Therefore, the GPS raw measurements, i.e. pseudorange and Doppler on L1, are pre-processed by C^3NAVG^{2TM}. An elevation mask of 15° was used. Ionospheric and tropospheric corrections were not applied because the maximum baseline length is not greater than 22 km and for such a short baseline DGPS can effectively remove most of the atmospheric affects. The DGPS results from C^3NAVG^{2TM} were assessed through a comparison with the reference trajectory. The statistics of the position and velocity differences between C^3NAVG^{2TM} and the reference trajectory are shown in Table 4-3. Both the RMS values of the horizontal position

differences are less than 0.24 m, and the horizontal RMS value of the velocity difference is no greater than 0.38 cm/s. The maximum horizontal position error is 2.5 m and the maximum velocity error is 3.0 cm/s. This means that the C3NAVG2^{TM} positions and velocities have consistent accuracy, and can be used as updates to the medium accuracy IMU as going to be discussed in the following sections. The horizontal position error variation versus time is shown in Figure 4-7. Figure 4-8 shows horizontal velocity error versus time. Figure 4-9 shows the satellite geometry and available satellite numbers during this simulated test run. The maximum satellites available is 9, and the minimum is 5, with an average of 7. The figure also shows that the DOPs are connected with the satellite numbers. For example, at GPS time 33300 seconds, an increased satellites number from 6 to 8 caused DOP values decreased almost 50 % at the same time. This consequently affects the position and velocity accuracy. Examining Figures 4-7, 4-8 and 4-9, it is clear that both the position and velocity errors decrease at GPS time 33300 seconds. These discussions show that, during this simulated test run, the DGPS position and velocity solutions from the C^{3}NAVG^{2TM} have consistent accuracy so it can be used as position and velocity updates in the GPS/INS system. Comparing Table 4-3 with Table 5-3, which is a statistics of the position and velocity assessment of C^{3}NAVG^{2TM} results while using a field data, the accuracy of the simulation data results are marginally better than that of the field data. The reasons are: 1) there are no multipath errors in simulation data. 2) The satellite availability and geometry in the simulated data is better than that of the field test.

Table 4- 3 Statistics of Position and Velocity Difference of C^{3}NAVG^{2TM} VS Reference Trajectory Using Simulated Data

Component	Mean	RMS
Latitude (m)	0.00	0.24
Longitude (m)	-0.01	0.21
Height (m)	0.00	0.21
North Velocity (cm/s)	0.00	0.25
East Velocity (cm/s)	0.00	0.38

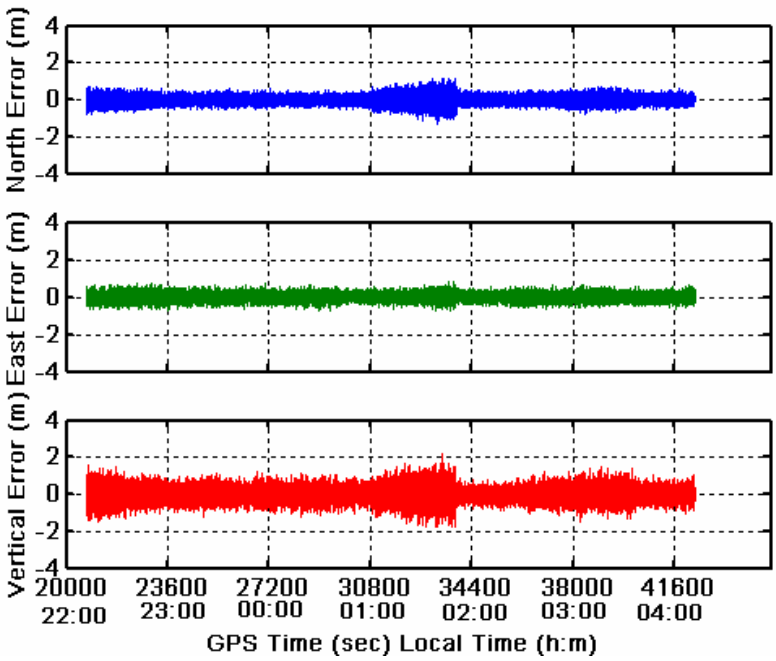

Figure 4- 7 Position Differences between C^{3}NAVG^{2TM} and the Reference Trajectory on the Simulated Data

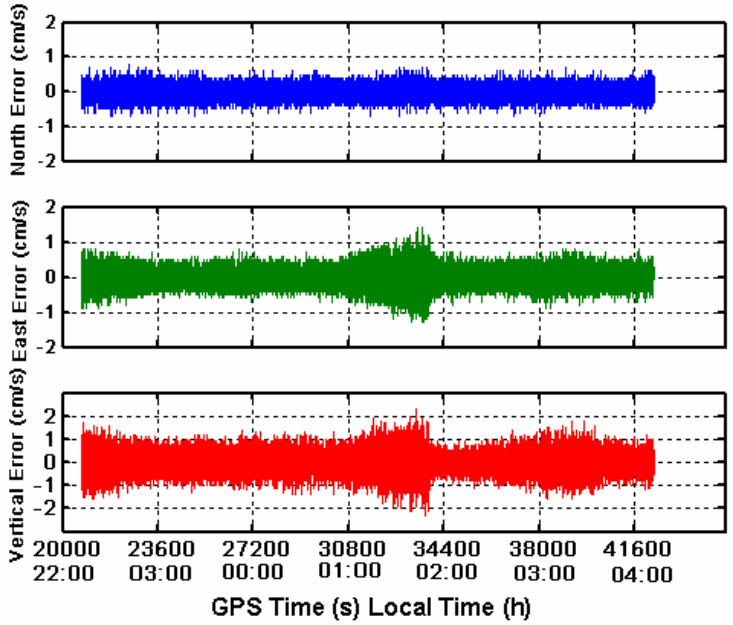

Figure 4- 8 Velocity Differences between C^{3}NAVG^{2TM} and The Reference Trajectory on the Simulated Data

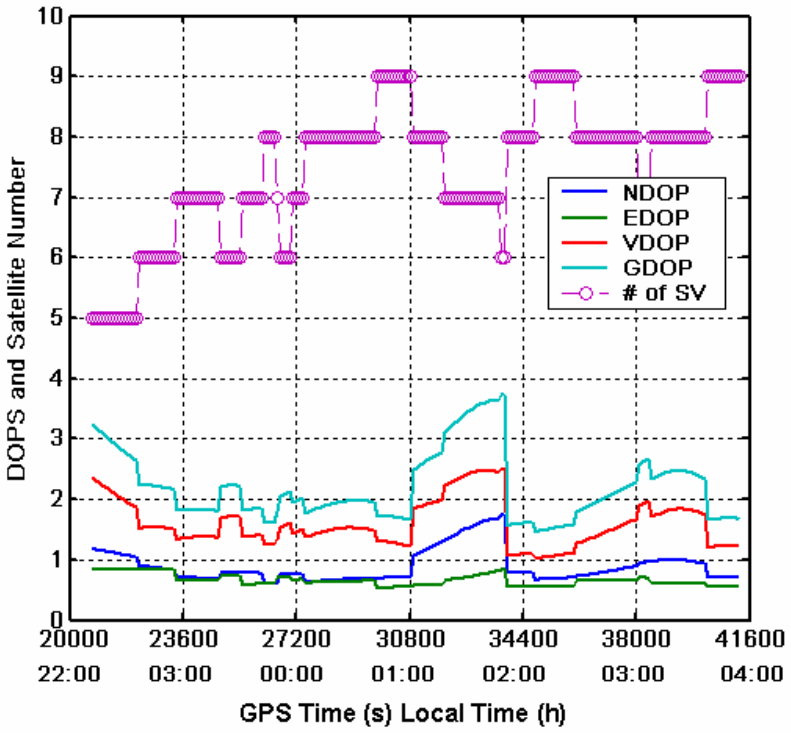

Figure 4- 9 Satellite Geometry and Availability during the Simulation Test

4.4 GPS/INS Integrated Results Using Kalman Filter

The navigation filter block shown in Figure 3-7 can be realized in different ways. In this chapter, a Kalman filter and a wave estimator will be implemented respectively to analyze the simulation data. In the next chapter, an IAE adaptive Kalman filter and a wave estimator will be realized to analysis the performance of the designed GPS/INS integration scheme by using the field test data. The following sub-sections will discuss the results using a Kalman filter.

4.4.1. Kalman Filtering Results Analysis

According to the mathematical model discussed in Chapter 3, a conventional Kalman Filter is implemented, and the accuracy of the Kalman filtering will be assessed. Table 4-4 shows the statistics of the horizontal position and velocity errors. Both the position and velocity errors have a zero means. The maximum position error has a value of 2.0 m, and the maximum velocity error has a value of 1.4 cm/s. Comparing Table 4-4 with 4-3,

it is clear that the accuracy of the filtered position and the velocity agreed with the accuracy of the DGPS position and velocity during this 6-hour simulation test. This is expected and shows that the GPS updates have effectively limited the IMU navigation solution errors. According to the sensor errors given in Table 4-1, the accumulated position error of INS-only will reach a maximum value of 400 km in 6 hours. Another advantage of GPS/INS integration is that it can provide attitude information, which is usually not available for the off-shelf GPS receivers. INS-only attitude information will be degraded due to sensor errors, initial misalignment and system noise. Using Kalman filtering with some attitude correction method suitable for medium to low accuracy IMU unit (Salychev, 2000), the misalignment angles can be limited to within a reasonable range, which is shown in Table 4-5. Table 4-5 shows that the horizontal misalignment angle is about 1 arc-minute. Figure 4-12 gives a plot of the horizontal misalignment angles.

Table 4- 4 Statistics of Position and Velocity Error Using a Kalman Filter

Component	Mean	RMS
North Position (m)	0.00	0.40
East Position (m)	0.00	0.46
North Velocity (cm/s)	0.00	1.16
East Velocity (cm/s)	0.00	2.10

The maximum horizontal misalignment angle is not greater than 2 arc-minutes, and the maximum azimuth misalignment is about 2 degrees. The horizontal accuracy is much better than the azimuth accuracy. Since the horizontal accuracy is basically determined by the accuracy of the accelerometers. According to Table 4-1, the bias of the accelerometer is only about 1 mGal. This guaranteed the horizontal accuracy, while the azimuth accuracy is constrained by the initial azimuth alignment results. As the gyro drift can not be completely compensated, the initial azimuth misalignment angle may be as large as a few degrees (Salychev, 2003). This is the main reason of a larger azimuth misalignment angle.

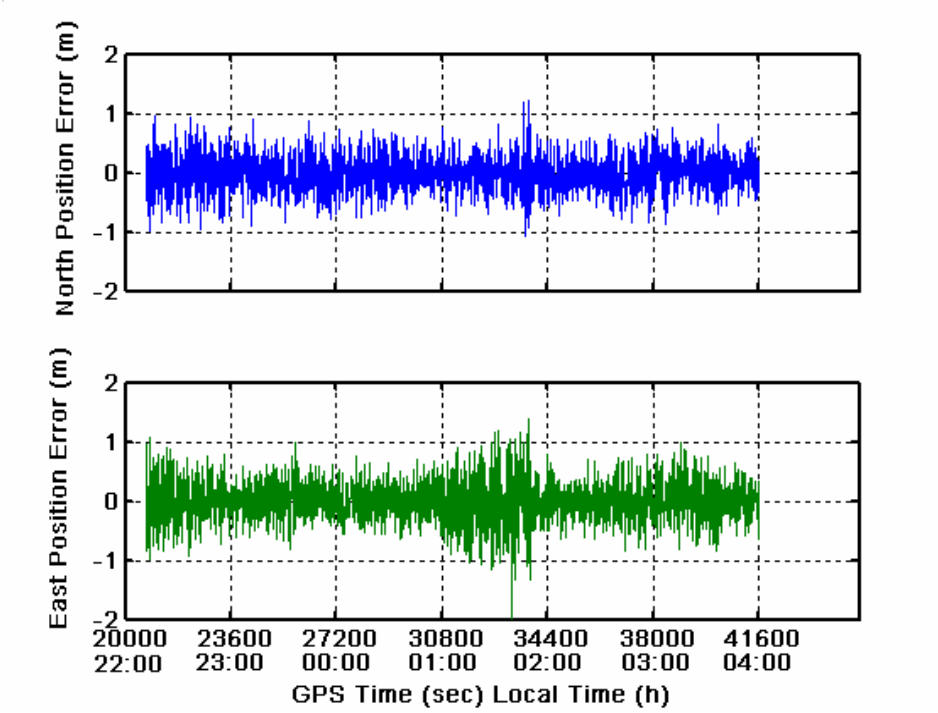

Figure 4- 10 Position Errors Using a Kalman Filter for the Simulated Data

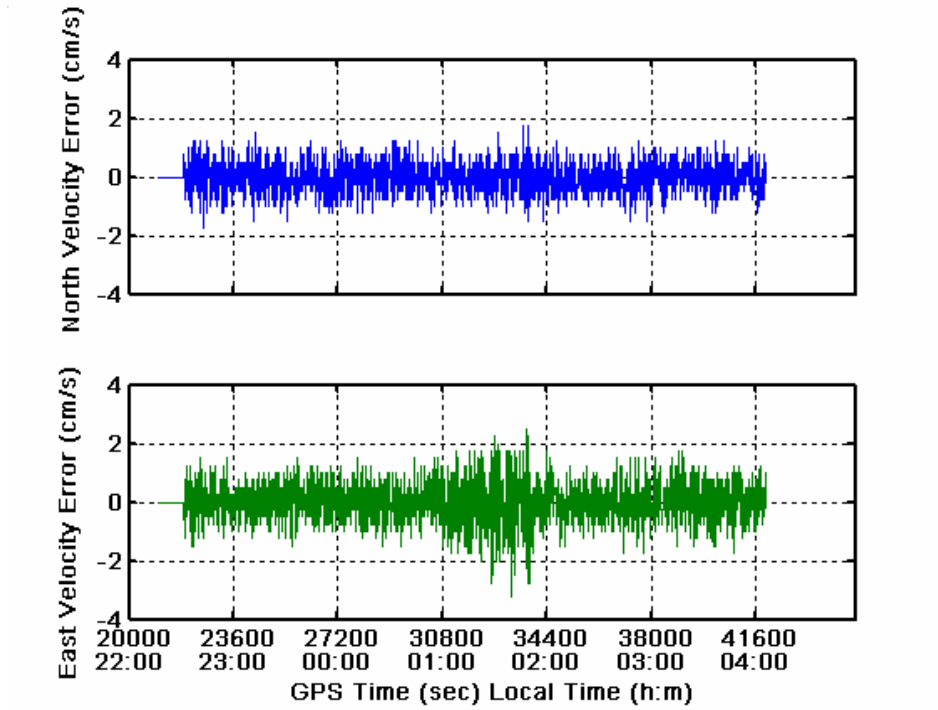

Figure 4- 11 Horizontal Velocity Estimation Errors of Kalman Filter for the Simulated Data

Table 4- 5 Misalignment Angle of Kalman Filter Using Simulation Data

	Mean	RMS
Roll (arcmin.)	-0.02	0.62
Pitch (arcmin.)	0.03	0.61
Heading (deg)	0.00	1

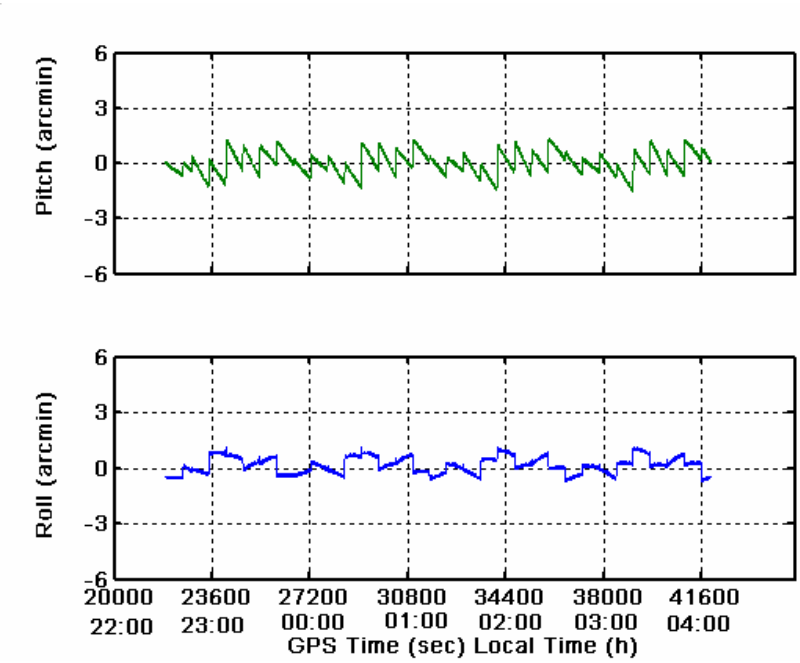

Figure 4- 12 Horizontal Misalignment Angle for the Simulated Data

4.4 GPS/INS Integrated Results Using a Wave Estimator

4.4.1.State vector Convergence Analysis

As discussed in Chapter 3, the wave estimation approach is suitable for the situation where the input disturbances are of low frequency, slow varying in nature, and have relatively weak observables in the state vector. The observability of a component of the state vector can be examined by its convergence property. It has been mentioned in Chapter 2 that the Kalman filter has a sequential behaviour of convergence for the different state vector components. The strongly observed state vector component converges first. For example, the component of the covariance matrix, or the RMS of the

estimation errors of each component of the state vector, can be examined to determine the observability of the state vector. Figure 4-13 shows the convergence process of the diagonal elements of the **P** matrix. In order to show the values of different range in a same frame, the diagonal elements of the P matrix have been normalized. This plot shows the transition process of the estimation errors. The position and the velocity errors converge first. Both of them have a transit time less than 5 seconds. The misalignment angles follow, it converges in 15 seconds, while the gyro drift will take more than 40 seconds to converge. Therefore, the gyro drift and the misalignment angles are considered as the weak observables.

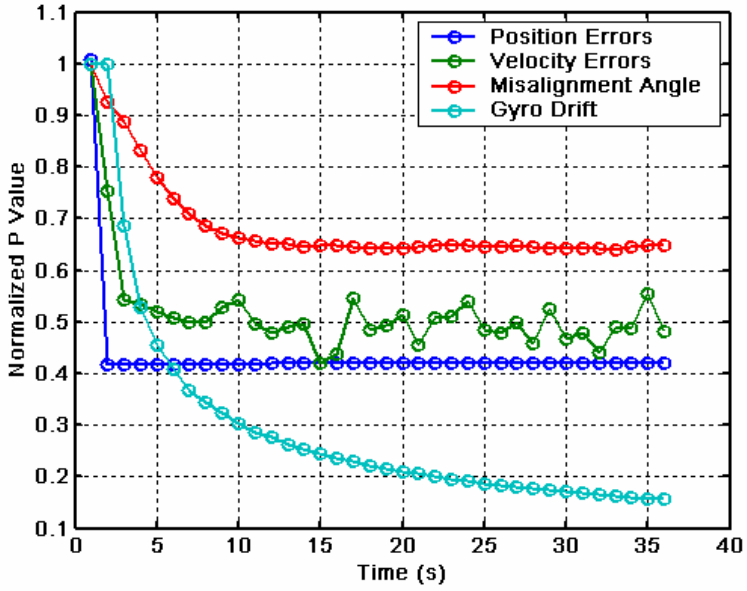

Figure 4- 13 Transit Process of the Covariance Matrix for the Simulated Data

According to the discussion in Section 3.3, the wave estimator is suitable for the estimation of weak observables, and the state component which has a close relationship with the weakly observed state vectors will benefit from it. In this case, the accuracy of the misalignment angle estimates are expected to have an improvement since it has a close relation with the gyro drift. This will be discussed in the next sub-section.

4.4.2 Benefits of the Estimation for Weakly Observed State Vectors

The gyro drift is described by a wave function. It increased the estimation accuracy of the weakly observed states, in this case, the misalignment angles. This can be explained by

the SINS error propagation process. Figure 4-14 show a simplified SINS error diagram, which ignored the Coriolis acceleration and the coupling terms between horizontal loops. It is suitable for short-term applications. In this figure, R is the average radius of the Earth; s is the Laplace operator; g is the gravity; ΔA is the accelerometer bias and ω^{dr} is the gyro drift. The misalignment angle can be derived from the diagram:

$$\begin{aligned} \dot{\varepsilon}_n &= \frac{\delta V_e}{R} + \omega_n^{dr} \\ \dot{\varepsilon}_e &= -\frac{\delta V_n}{R} + \omega_e^{dr} \end{aligned} \tag{4-1}$$

Equation (4-1) shows that the gyro drift has a direct affect on the misalignment angles. As discussed in Section 2.3, the velocity error equations have a close relation with the misalignment angle. See Equation (2-22). It can be expected that, if the gyro drift (weak observable) can be adequately estimated using a wave model, the misalignment angle estimation will be benefit greatly; consequently, the velocity estimation will be benefit to some extent as well. Figure 4-15 shows a simplified flowchart for wave stimulator calculation according to the derivations in Section 3.3.

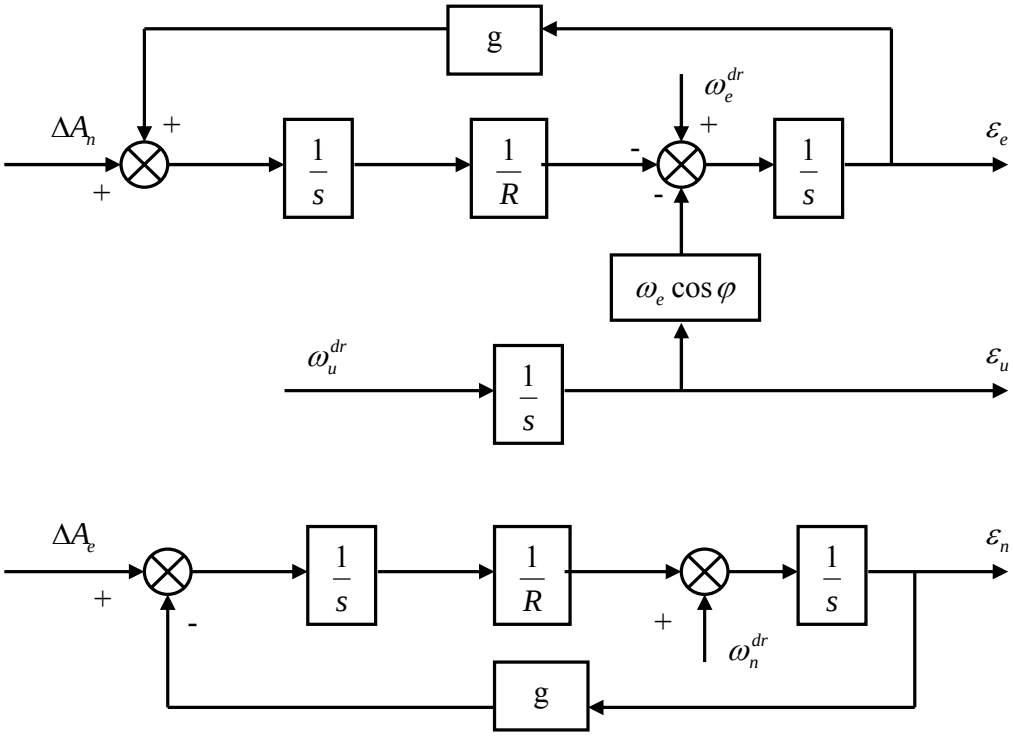

Figure 4-14 Simplified SINS Error Propagation Diagram (from Yi, 1987)

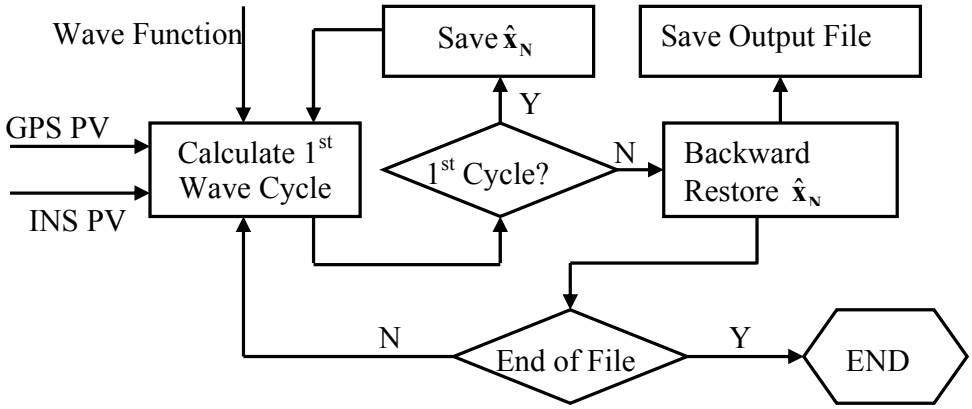

Figure 4- 15 Calculation Flowchart of Wave Estimation

Together with the INS derived positions and velocities, GPS positions and velocities are sent to the wave estimator. State vectors are directly estimated at the end of each wave cycle. After the first wave cycle, state vectors at every epoch can be recovered through a backward restore technique. This means a wave estimator can not be used as a real-time filter. It has a time delay equal to the length of a wave cycle.

4.4.3 Estimation Results Using Wave Estimator

Figures 4-16 and 4-17 give the estimated position and velocity errors by using the wave estimator. Through trial and error, the wave cycle was selected as 300 seconds. As a result, there are no estimates in the first cycle as mentioned in Section 3.3. Therefore, what is shown here is the estimation error starting at the second wave cycle. Comparing Figure 4-16 with 4-10, the position estimate of the Kalman filter and the wave estimator have a similar accuracy. However, the results from the Kalman filter are noisier than that of the wave estimator, since the wave estimator uses the pseudo-determinate model to describe the system noise. Figure 4-17 shows the velocity estimation errors of the wave estimator. The maximum horizontal velocity error is no greater than 1 cm/s. Table 4-5 shows the statistics of the position and velocity errors with the wave cycle equal to 300 seconds. The jumps at the beginning of some wave cycles in Figure 4-17 are caused by an improperly selected initial values of the vector **s** for that wave cycle, and the

assumption that the wave coefficient of the input noise changes at a fixed interval, (300 seconds here), which might not be the best choice.

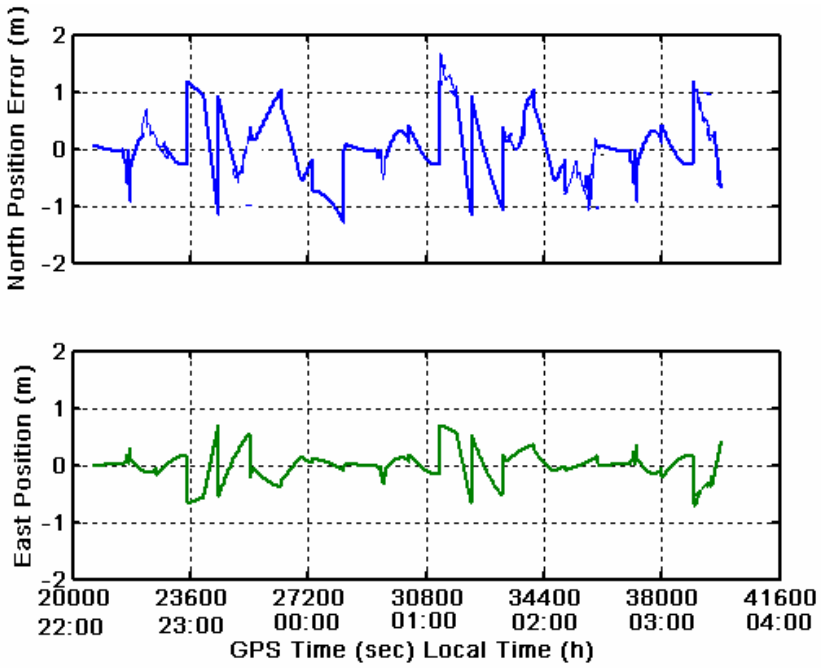

Figure 4-16 Position Errors Using a Wave Estimator for the Simulation Data

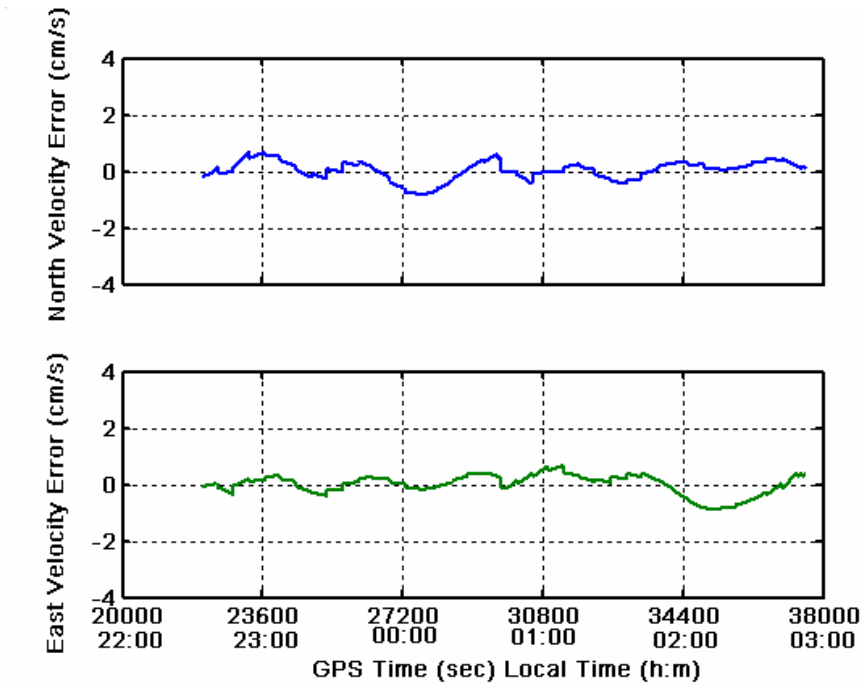

Figure 4- 17 Velocity Errors Using a Wave Estimator for the Simulation Data

Table 4- 6 Statistics of Position and Velocity Estimation Errors

Component	Mean	RMS
North Position (m)	0.00	0.26
East Position (m)	0.00	0.25
North Velocity (cm/s)	0.00	0.40
East Velocity (cm/s)	0.00	0.52

Figure 4-18 shows the horizontal misalignment angle, and Table 4-5 gives the statistics. Comparing Figures 4-18 with 4-14, it is clear that the estimation accuracy of the horizontal misalignment angle increased greatly. According to the discussion in Chapter 3, a wave estimator is suitable to the weakly observed states. In this research the gyro drift has been described by the wave function, therefore, the state vector, which has a stronger relation with it, will benefit by the wave approach. The estimation of the misalignment angles improved significantly. On the other hand, the position error, which does not have a strong relation with the gyro drift, has no direct benefit.

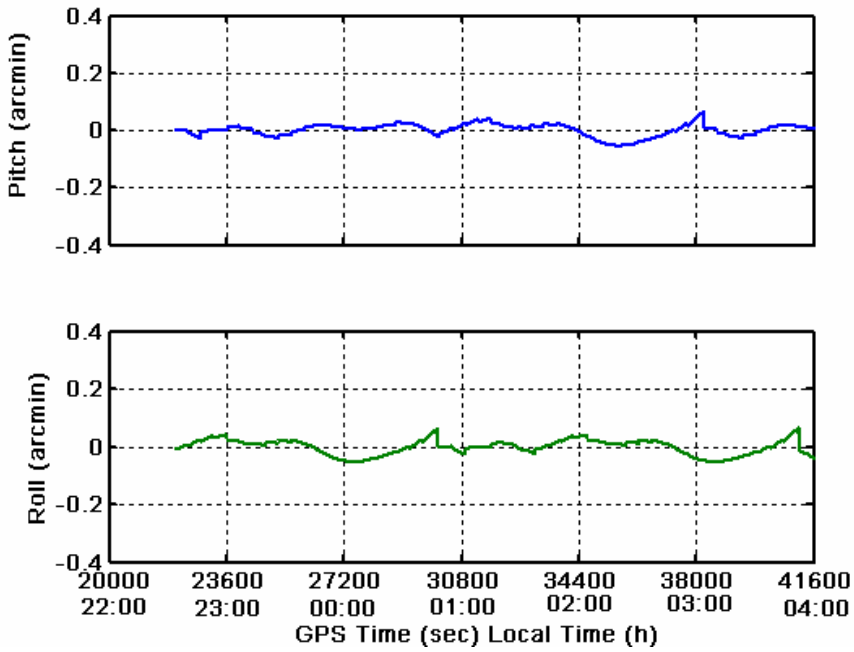

Figure 4- 18 Horizontal Misalignment Angle Using Simulated Data

Table 4- 7 Statistics of Misalignment Angles

Component	Means	RMS
Roll (arcmin.)	0.00	0.09
Pitch (arcmin.)	0.00	0.16
Heading (deg)	0.00	0.60

4.5 Summary

The objective of this research was to develop a metre-level accuracy integrated navigation scheme using a medium accuracy IMU. An Inertial navigation system in principle permits autonomous operation. However, due to its error propagation characteristics, most applications requiring high terminal accuracy, utilize external aiding to reduce the INS errors, GPS, in this case. As discussed in the previous chapters, a feedback aiding technique has been used to develop this loosely coupled GPS/INS integration system. The residuals formed by differencing the INS position velocity and GPS position velocity, are sent to the Kalman filter. The Kalman filter contains an internal model of the INS error dynamics and processes the measurements to estimate the value of INS errors. As a feedback scheme, which offers greater robustness, is selected, this system has relatively high accuracy and stability. A simulated data set has been used in this chapter in order to assess the design and implementation of the Kalman filter and the wave estimator. As discussed in Chapter 3, a wave estimator has the advantages of providing higher estimation accuracy in a situation where the input disturbances are of low frequency, slowly varying in nature, and rely on relatively weak observables. The results showed that the state vector, which has a stronger relation with those waveforms described weak observables, would achieve better estimation accuracy. According to the test results, a brief summary is given as follow:

1. Pseudorange DGPS position and velocity updates limited the time dependent INS position and velocity errors through Kalman filtering.

2. Using simulated GPS/INS data, the Kalman filter's maximum position error is no greater than 2.5 m in horizontal. The RMS values for position errors are less than 0.46 m. The RMS values for velocity errors are no greater than 2.1 cm/s.

3. Using simulated GPS/INS data, the wave estimator's maximum position error is no greater than 1.25 m in the horizontal. The RMS values for position errors are less than 0.26 m. The RMS value for velocity errors is no greater than 0.5 cm/s. Compared to the results there is no obvious improvement. The reason for this is that position error estimation does not have a tight coupling with the weakly observed states, the gyro drift, in this case. For velocity error estimation, a wave estimator can achieve better results (see Chapter 5 also).

4. Using a Kalman filter, the estimation accuracy for the horizontal misalignment angle had an RMS value of 0.62 arc-minutes. The Azimuth misalignment angle, it had an RMS value of 1 degree.

5. Using a wave estimator, the estimation accuracy for the horizontal misalignment angle had an RMS value of 0.16 arc-minute, and for the Azimuth misalignment angle, the RMS value was 0.6 degrees. The horizontal misalignment angle estimation improved about four times.

6. Comparing the results from 4 and 5 above, it is clear that attitude estimation can achieve higher accuracy when using a wave estimator.

7. A fixed wave cycle has been used in processing this data set. In practice, the slowly changed sensor's bias can be described more accurately by using a changing cycle time. Therefore, estimation cycle-time adaptive choice will be a future research subject.

CHAPTER 5

RESULTS AND ANALYSIS USING FIELD DATA

As discussed in the Chapters 2 and 3, the mathematical models for both of the Kalman filter and the wave estimator have been established for a loosely coupled integration scheme. Their advantages and disadvantages are also evaluated theoretically. In Chapter 4, a data set from CastNav 4000 GPS/INS simulator was analysed. A real data set from a field test is necessary to evaluate the integration filter. In order to assess the performance of the GPS/INS integration scheme and its application to practice, a land vehicle field test was carried out in Calgary, Alberta. In this chapter, field test results are analysed. As there was no attitude reference while collecting this data set, attitude accuracy can not be assessed in this chapter. Instead, an IAE adaptive filter will be applied to the field data. Also, the INS prediction accuracy for the Kalman filter will be discussed.

5.1 Equipment and Setup

The base station used in this test is a NovAtel OEM-3 Millennium GPS card. The vehicle (rover) was equipped with a NovAtel Black Diamond System (BDS). BDS is a tightly integrated GPS/INS system (NovAtel Inc., 2001) consisting of:

1. BDS controller: The controller is a high performance, dual frequency NovAtel OEM4 GPS card with a PC card slot for raw GPS and IMU data logging.

2. BDS inertial sensor: BDS uses a Honeywell HG1700 IMU, which is a strapdown system using a triad of accelerometers and a triad of ring laser gyros (RLG). Table 5-1 shows the Honeywell HG1700 specifications.

The inertial sensors are mounted orthogonally inside a compact (15 cm high× 15 cm diameter) cylindrical case to measure specific force and angular increments in the body frame. Internally the velocity and rotation angle increments are sampled at a 600Hz rate. Coning and sculling compensations are applied to the accumulated velocity and angular increments. The hardware is shown in Figure 5-1.

Figure 5-1 Honeywell HG1700 IMU and Novatel Black Diamond System(BDS)

(http://www.novatel.com/images/products/bds_sm.jpg)

Table 5-1 Honeywell 1700 IMU Specifications (Honeywell Inc)

Specification	Value
Gyro Input Rate	± 1,000 deg / sec.
Gyro Rate Scale Factor	100 ppm
Gyro Rate Bias	1.0 Deg
Angular Random Walk	0.125 deg/$\sqrt{hr}$. to 0.3 deg/$\sqrt{hr}$.
Accelerometer Range	± 50 g
Accelerometer Linearity	500 ppm
Accelerometer Scale Factor	300 ppm
Accelerometer Bias	1.0 mg (980 mGal)

The test run was carried out in Calgary, Alberta, August 16, 1999. The dataset was collected by the graduate student in Geomatics Engineering. The system was mounted on the roof of the test vehicle and the antenna was hard-mounted on the case containing the IMU. The vehicle was driven on a L-shaped traverse as shown in Figure 5-2. The total duration of the test was about 75 minutes. Raw measurements from the OEM-4 receiver were logged at a 1 Hz rate, and the raw angular rates and specific force data from

HG1700 were recorded at 100 Hz. The maximum baseline length is 11.7 km. The reference station coordinate is:

$$\varphi = 51^{\circ}09'47" \qquad \lambda = -114^{\circ}00'05" \qquad h = 1073.09m$$

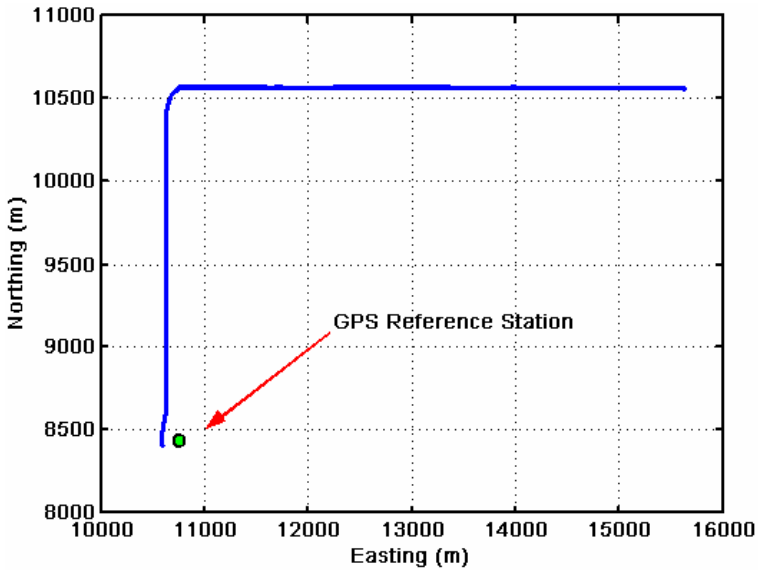

Figure 5-2 Field Test Route

5.2 Data Pre-Processing

5.2.1 Generation of Reference Trajectory

In order to evaluate the integrated results, a reference trajectory was generated to determine if the integration filter was properly designed and implemented. The GPS data was first processed using FLYKIN^{TM}, which is a kinematic software package that processes double differenced (DD) carrier phase, pseudorange and Doppler measurements (Cannon et al., 1999). A Kalman filter is utilized whereby the filter states consist of position and velocity corrections as well as an ambiguity state for each of the double differenced carrier phase measurement. Parallel to this, an integer ambiguity resolution scheme is implemented whereby a search is conducted for the correct integer ambiguity. FLYKIN^{TM} has been used to assess numerous receiver technologies and GPS

missions (Cannon et al., 1997). The satellite elevation cut-off angle used was 15°. Only L1 measurements were used in this test. In order to prove that the carrier phase reference solution was in fact accurate, all the ambiguity fixed DD carrier phase residuals were calculated, and their statistics are given in Table 5-2. RMS values for the DD carrier phase residuals were generally less than 0.8 cm, and the residuals did not exceed ? .6 cm. This shows that the accuracy is consistently high throughout the test and no gross errors occurred. Fixed solutions were achieved at every epoch during the test run. It can then be reasonably assumed that the reference trajectory is accurate to within a few centimetres.

Table 5- 2 GPS DD Carrier Phase Residual Statistics (cm)

PRN	Mean	RMS	Max	Min
3	0.3	0.6	1.9	-1.3
6	0.2	0.6	2.0	-1.5
10	0.1	0.5	1.3	-1.3
13	0.2	0.3	0.7	-0.4
17	0.2	0.4	1.1	-1.0
21	-0.3	0.7	1.5	-2.1
23	0.3	0.8	2.6	-1.9
26	0.0	0.5	2.3	-1.8

5.2.2 Assessment of DGPS Position and Velocity

One of the objectives of this research is to achieve metre-level positioning results by using position and velocity derived from carrier phase smoothed GPS pseudorange measurements integrated with a medium accuracy IMU. So the GPS raw measurements, i.e. pseudorange and carrier phase on L1, were pre-processed by C^3NAVG^{2TM}. The DGPS results from C^3NAVG^{2TM} were assessed through a comparison with the FLYKIN^{TM} results. The statistics of the position and velocity differences between C^3NAVG^{2TM} and the FLYKIN^{TM} are shown in Table 5-2. Both the RMS values of the horizontal and vertical position differences are less than 0.25 m, and the horizontal RMS values of the velocity differences are not greater than 2.7 cm/s. The position differences versus time is shown in Figure 5-3. Figure 5-4 shows how the velocity differences varies

with time. Figure 5-5 shows the satellite geometry and available satellite numbers during the test run. The maximum number of satellites is 9, and the minimum is 4, with an average of 7. These figures show that the DOPs are correlated with satellite availability as expected. For example, at GPS time 14620 seconds, the number of satellite decreased from 9 to 5. The related DOPs values have a jumped increase. This change consequently degraded the position accuracy. These results show that the C^{3}NAVG2^{TM} positions and velocities have a consistent accuracy during this field test, and can be used as updates to the medium accuracy IMU as discussed in the following sections.

Table 5- 3 Statistics of Position and Velocity Differences of C^{3}NAVG^{2TM} versus FLYKIN^{TM} for the Field Data

Component	Mean	RMS
Latitude (m)	-0.14	0.24
Longitude (m)	0.15	0.33
Height (m)	0.15	0.24
North Velocity (cm/s)	0.00	2.70
East Velocity (cm/s)	0.00	1.20

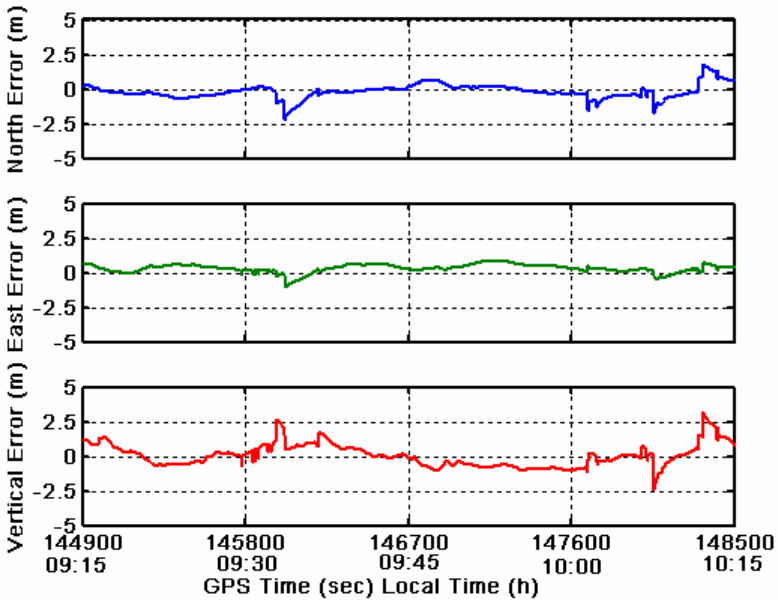

Figure 5- 3 Field Test Data Position Accuracy Assessment

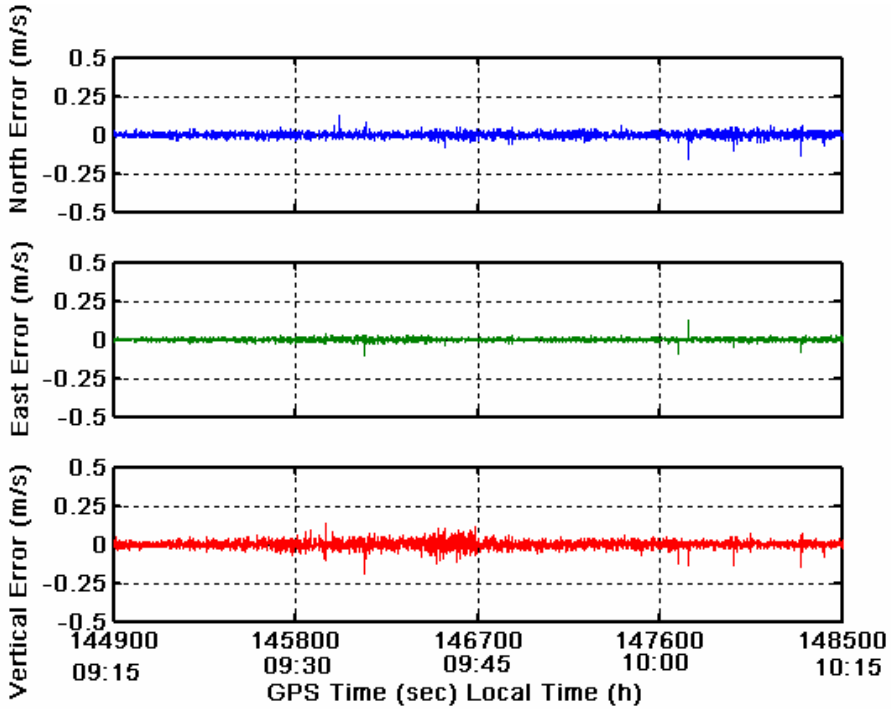

Figure 5- 4 Field Test Data Velocity Accuracy Assessment

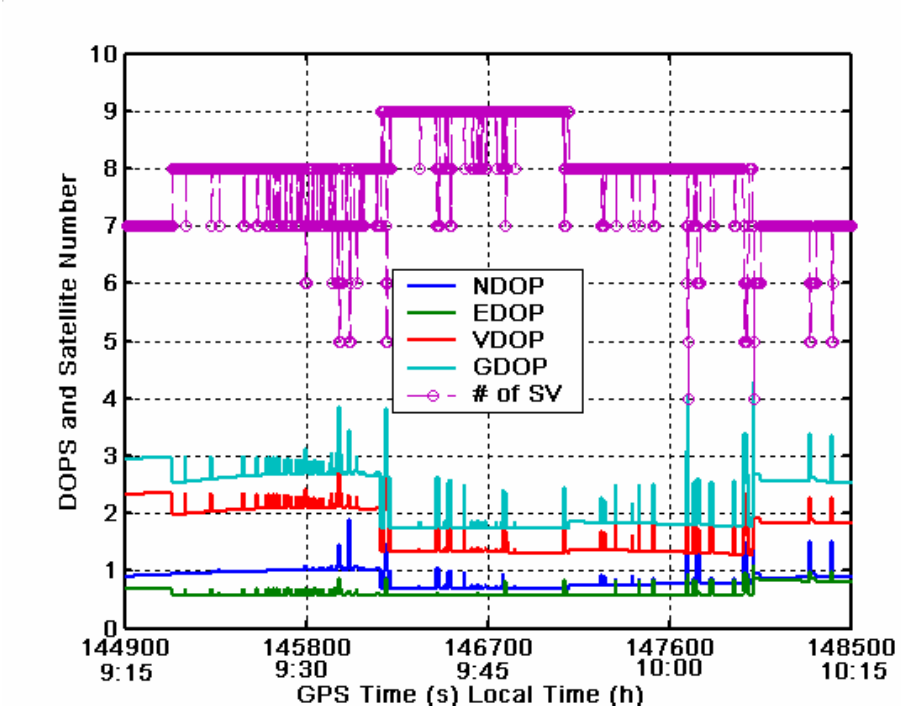

Figure 5-5 Satellite Geometry and Availability for Field Test Data

5.2.3 Simulation of GPS Data Outages

One of the advantages of GPS/INS integration is that the INS predicted positions and velocities are available during GPS outages. The accuracy of the INS predicted positions depends on the following factors: (1) the initial accuracy at the start of the GPS outage, (2) the inertial sensors' properties and (3) the dynamics of the vehicle before and during the GPS outage. Although there were no GPS outages during this test run, different GPS gaps were simulated to check the INS prediction accuracy. The reference trajectory during this simulated outage can be used as a reference to evaluate the prediction results. Both full GPS outages and partial outages were simulated.

A full GPS outage is defined here to be the complete absence of all the GPS observable data, during the time that the GPS satellites are completely blocked. A partial outage is defined to occur when some of the satellite signals are blocked due to canopy or dense urban canyons, for example. The number of observables may be as low as 2 or 3. During these time intervals, the GPS receiver is either unable to complete the positioning calculation or the positioning accuracy is degraded due to poor satellite geometry. There were 10 GPS full data outages simulated for this test run. The data gaps were selected to encompass different vehicle dynamics, from constant velocity to relatively large along-track and lateral acceleration. In this way INS prediction accuracy under different situations can be evaluated. Figure 5-6 shows the 3D field test run trajectory and where the outages were artificially added. Prediction accuracy during the data outages is assessed by the reference solution. Table 5-4 shows the properties of these 10 simulated outages. The duration of the simulated data gaps varied from 5 to 10 seconds. No manoeuvre means the vehicle travels with constant speed during GPS outages. Manoeuvre means there are accelerations during or just before the outage occurs. Partial GPS outage were simulated by artificially raising the satellite cut-off elevation. 30° and 40° cut-off elevations were selected respectively. In each case the available satellite number was not greater than 4. Figure 5-7 shows the HDOPs and the satellite availability at 30° and 40° elevation cut-offs respectively. For the 30° elevation mask case, there were four satellites available most of the time. However, in the 40° elevation mask case,

only 3 satellites were available in general. A decreased number of satellites will cause high DOP values. It is clear that the DOP values are different between the 30° and 40° cut-off angle cases. As discussed in Section 2.1.1, the GPS positioning accuracy is measured by the combined non-modeled measurement error and the effect of the satellite geometry. The non-modeled measurement errors will certainly be different from one satellite to another because of the various view angles. A more simplified way of examining the GPS positioning accuracy can be achieved through the introduction of the user equivalent range error (UERE). Multiplying the UERE by the appropriate DOP value produces the precision of GPS positioning at a 1σ level. Based on above-mentioned situations, INS prediction results will be given in the next section and their accuracy will be analysed.

Table 5-4 Simulated GPS Data Gap Properties

Outage #	Start Time (s)	Position Error (m)		Dynamics During Outage
		North	East	
1	144670	-0.01	-0.03	No manoeuvre
2	145280	0.09	-0.13	Manoeuvre
3	145760	0.02	-0.02	Manoeuvre
4	145920	0.17	0.66	Manoeuvre
5	146362	0.16	-0.31	Manoeuvre
6	146986	-0.01	0.16	No manoeuvre
7	147048	-0.21	-0.43	Manoeuvre
8	147580	0.12	-0.03	No manoeuvre
9	147920	0.41	-0.21	No manoeuvre
10	148230	0.32	-0.21	Manoeuvre

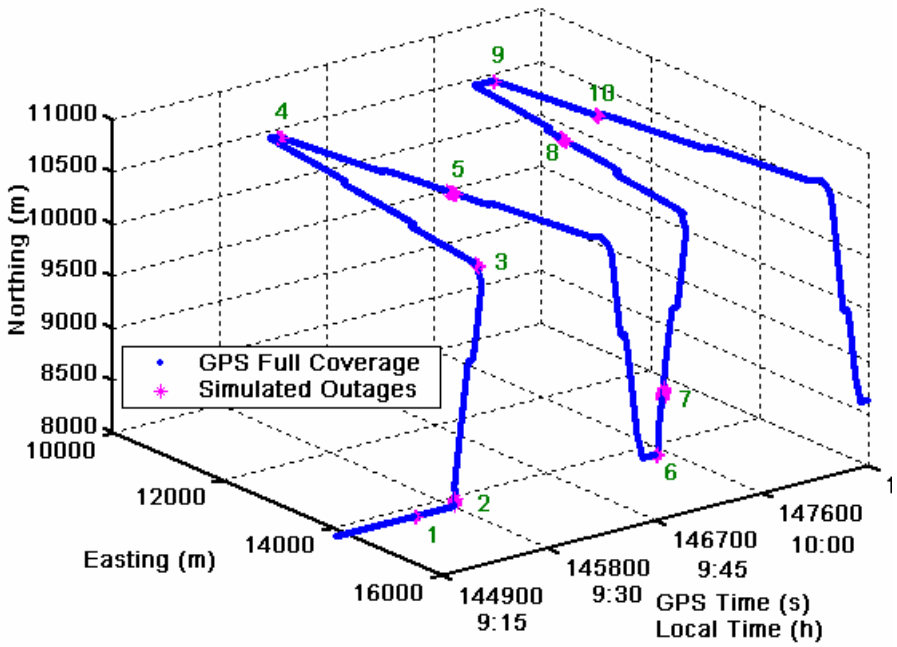

Figure 5- 6 3D Trajectory and GPS Outages for Field Data

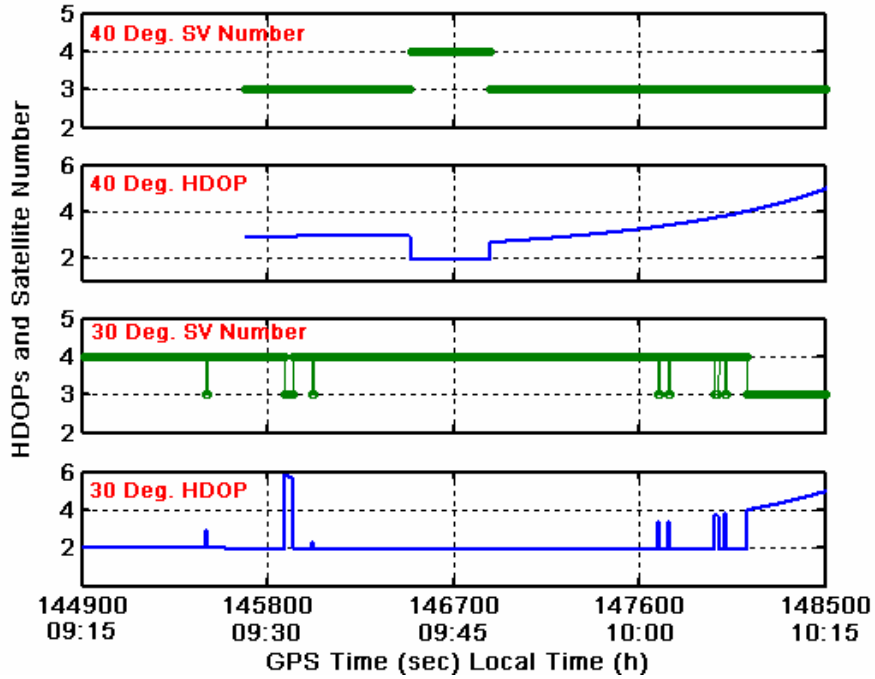

Figure 5- 7 HDOPs and Satellite Number during Partial GPS Outages for Field Data

5.3 GPS versus GPS/INS Integrated Results Using a Kalman Filter

5.3.1 Filtering Results Analysis

The Kalman filter approach for GPS/INS integration is first assessed. Figures 5-8 and 5-9 show the integrated GPS/INS position and velocity errors respectively, which have been determined through a comparison with the reference trajectory. The DGPS positions and velocities are from C^3NAVG^{2TM}. Table 5-5 shows that the RMS value of the horizontal position errors do not exceed 0.5 m and the RMS of the velocity error is limited to within 3.5 cm/s. In the above results, the variance matrix of input the noise is $\mathbf{Q} = \mathbf{Q_0}$, where $\mathbf{Q_0}$ is the average input noise at steady state. $\mathbf{Q_0}$ has been determined by modifying the conventional Kalman filter to an IAE adaptive **Q**-only filter. As discussed in Section 3.2.2, wherein the measurement noise matrix is kept constant and the input noise is estimated adaptively. In Figure 5-8, there are some jumps in the plot of north position error. Comparing to Figure 5-5, the change of satellite geometry causes jumps of the horizontal DOPs value, which coincide with the jumps of the horizontal position error at GPS time 146200 and 148050 seconds respectively.

Table 5- 5 GPS/INS Estimation Error Statistics for Field Data

Component	**Mean**	**RMS**
Latitude (m)	0.05	0.50
Longitude (m)	0.24	0.38
North Velocity (cm/s)	0.00	3.50
East Velocity (cm/s)	0.00	3.10

The average of the estimated input noise at steady state is calculated and used as $\mathbf{Q_0}$ since the system is assumed to be stationary. Table 564 shows the position and velocity accuracies with different input noise values derived from the average steady state values. The statistics show that with higher **Q** (i.e. $\mathbf{Q}>\mathbf{Q_0}$) or lower **Q** (i.e. $\mathbf{Q}<\mathbf{Q_0}$) input noise values, the estimates become noisier and have increased RMS values. This shows that the estimation accuracy is restricted by the level of input uncertainties in the system model. The accuracy cannot be increased within the scope of this type of modeling method.

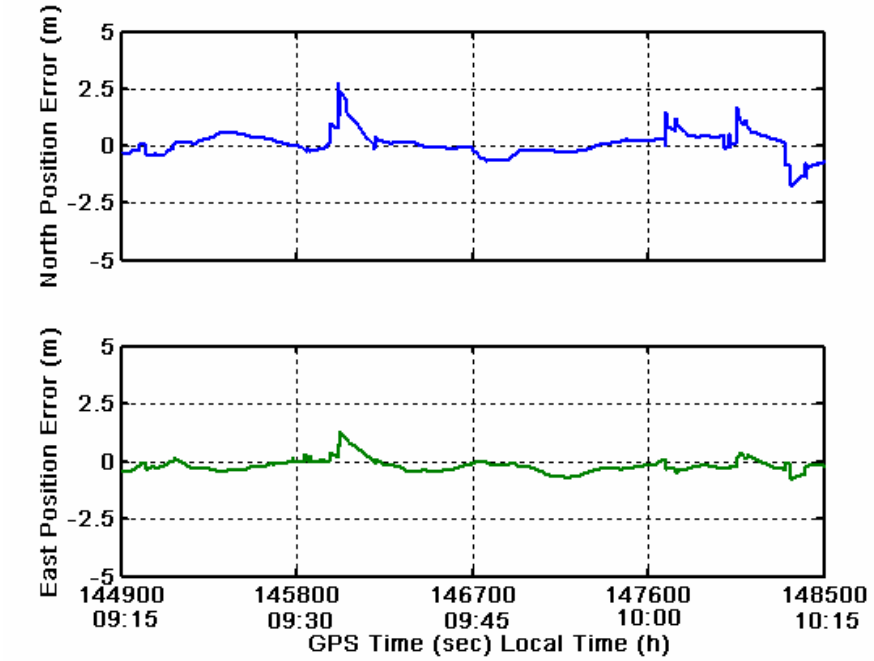

Figure 5-8 Position Errors of Kalman Filtering Result for Field Test Data

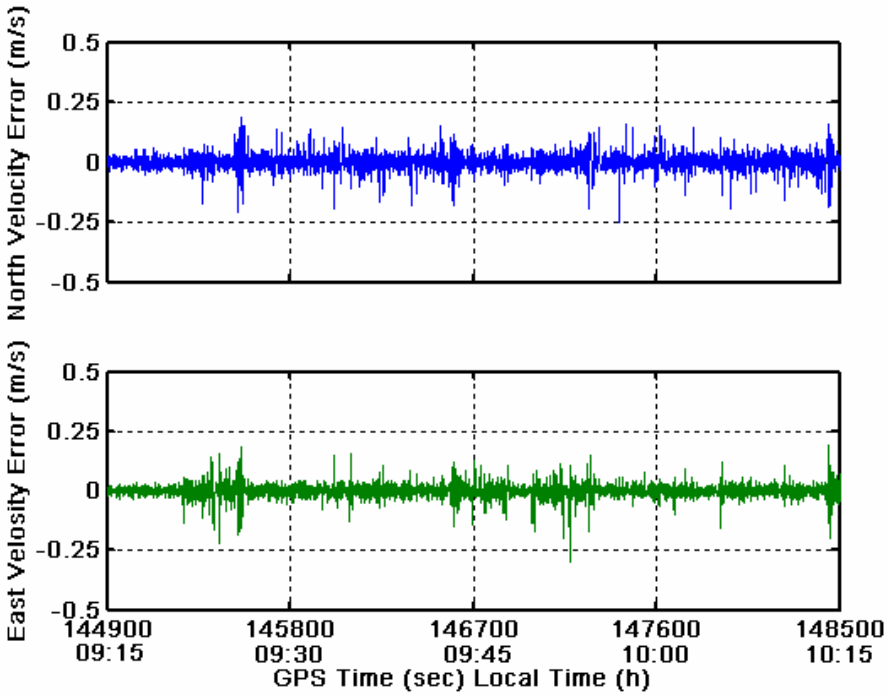

Figure 5-9 Velocity Errors of Kalman Filtering Result for Field Test Data

The results show that when using a conventional Kalman filter, the RMS values for the horizontal positions are no greater than 0.58 metres, and RMS values for horizontal velocities are no less than 3.1 cm/s. For the horizontal loops, the updated position has a DRMS of 0.88 metres. These results satisfy the metre-level positioning requirement.

Table 5- 6 Statistics of GPS/INS Errors with Different Input Noise Values

Value of Q_0	Component	Mean	RMS
$0.01Q_0$	Latitude (m)	0.31	1.12
	North Velocity (cm/s)	0.00	4.30
	Longitude (m)	0.21	0.96
	East Velocity (cm/s)	0.00	3.90
$0.1Q_0$	Latitude (m)	0.16	0.50
	North Velocity (cm/s)	0.00	4.60
	Longitude (m)	0.09	0.71
	East Velocity (cm/s)	0.00	3.60
Q_0	**Latitude (m)**	**0.15**	**0.40**
	North Velocity (cm/s)	**0.00**	**3.00**
	Longitude (m)	**0.11**	**0.58**
	East Velocity (cm/s)	**0.00**	**3.10**
$10Q_0$	Latitude (m)	-0.43	1.14
	North Velocity (cm/s)	0.00	9.00
	Longitude (m)	-0.16	0.80
	East Velocity (cm/s)	0.00	8.20
$20Q_0$	Latitude (m)	-0.46	1.17
	North Velocity (cm/s)	0.00	10.00
	Longitude (m)	-0.01	0.92
	East Velocity (cm/s)	0.00	8.90

5.3.2 Prediction Accuracy Analysis

Full Outage Situation

As discussed in the subsection 5.2.3, GPS data gaps were simulated. 5 seconds and 10 seconds outage time were applied to the 10 data gaps respectively. Figure 5-10 shows 8 INS prediction position errors out of the 10 data gaps. Outage #1 shows results for a 5

seconds GPS outage with a low constant speed and with no manoeuvring. The data gap started at GPS time 144670 second with initial error of - 0.01 m. The maximum predicted horizontal error reached 0.25 metres at GPS time 144675 second when the outage ended. Outage #3 shows another 5 seconds GPS outage time, but with vehicle manoeuvrings. It started at GPS time 145760, the initial error is about 0.09 m. The maximum acceleration during this period reached 1.12 m/s^2. The maximum horizontal error is over 3 metres when this five second outage ended. Outage # 9 shows that during a 10 second GPS outage, the maximum position error is 1.25 m when the vehicle is moving at a constant speed. This data gap started at GPS time 146920 seconds with an initial error of 0.2m. The position error reached 0.5 m after 5 seconds INS prediction. Outage #10 is another 10 seconds data gap start at GPS time 148230 with an initial error about –0.2 m. The vehicle was manoeuvring with a maximum acceleration of 2.15 m/s^2 during this data gap. The maximum error is as high as 11.75 m when the data gap ended at GPS time 148240 seconds.

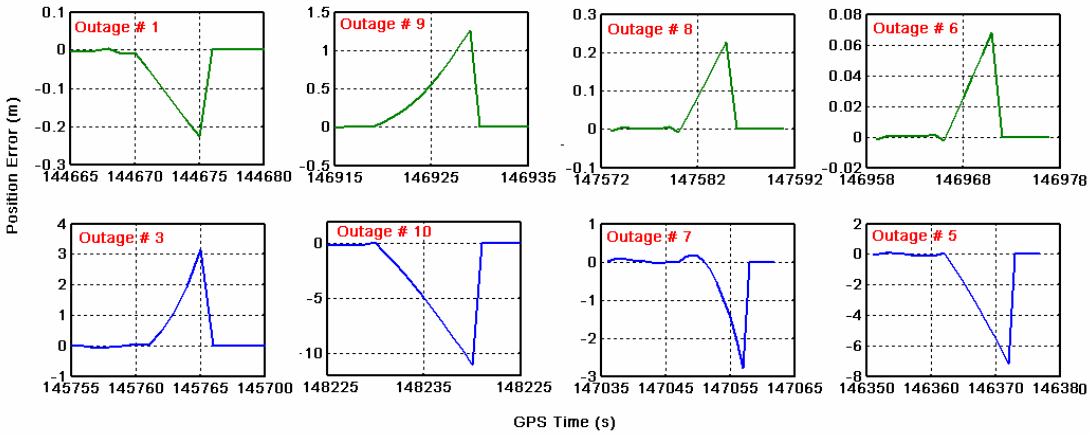

Figure 5- 10 INS Prediction Error for Field Test Data

Table 5-7 gives the statistics of prediction position errors. The results show that the prediction accuracy is dependent on the vehicle dynamics greatly during the GPS gaps. When the vehicle velocity changes during the prediction interval; the prediction accuracy is about 3.15 m over 5 seconds; while during the same GPS gap and the vehicle moving at a constant velocity, the maximum error is only 0.25 m. These errors are closely related

to the IMU (inertial sensor) properties. As discussed in Section 2.2.3, the inertial derived position errors can be divided into two categories, i.e. the stationary part and the non-stationary part. The analytical solution of Equation (2-24) can be expressed as Equation (5-1).

Table 5- 7 Statistics of Position Error during GPS Outage

Outage Time(s)		Position Errors (m)		
	Component	**Mean**	**RMS**	**Max**
5	No manoeuvre	-0.13	0.70	1.64
	Manoeuvre	1.33	1.64	0.81
10	No manoeuvre	0.55	0.81	6.45
	Manoeuvre	-5.66	6.45	1.64

Schuler Part Non-stationary Part

$$\delta\varphi = -\varepsilon_e(0)\cos\upsilon t + \frac{\delta V_N(0)}{\upsilon R}\sin\upsilon t + \omega_E^{dr}(t - \frac{1}{\upsilon}\sin\upsilon t) - \frac{b_y}{\upsilon^2 R}\cos\upsilon t - \frac{\varepsilon_u \Delta E}{R} + \frac{\mu_y \Delta N}{R}$$

$$\delta\lambda = \frac{\varepsilon_n}{\cos\varphi}\cos\upsilon t + \frac{\delta V_E(0)}{\upsilon R\cos\varphi}\sin\upsilon t + \omega_N^{dr}(t - \frac{1}{\upsilon}\sin\upsilon t) - \frac{b_x}{\upsilon^2 R\cos\varphi}\cos\upsilon t + \frac{\varepsilon_u \Delta N}{R\cos\varphi} + \frac{\mu_x \Delta E}{R\cos\varphi}$$

(5- 1) (from Salychev, 1998)

where $\delta\varphi$ and $\delta\lambda$ are the north and east position errors (m)

$\upsilon = \sqrt{\frac{g}{R}}$ is the Shuler frequency (rad/s), and

ΔN and ΔE are distance increments in north and east direction (m).

In Equation (5-1), the non-stationary part will increase with respect to the distance increment due to the azimuth misalignment angle and the accelerometer scale factor errors. This part may become very large as the distance increases. While the vehicle is moving with a constant speed, only the Schuler part is in effect. The position error is an un-damped oscillation with a 84.4 minutes cycle (Refer to Figures 2-8 and 2-9). The magnitude of the error is related to the gyro drift rate and the initial values of the

horizontal misalignment angles. During the vehicle dynamics, the non-stationary errors impact the inertial solution. This part increases with respect to the distance increment due to the azimuth misalignment angle and the accelerometer scale factor error. The non-stationary part may become very large as the distance increases. This explains why the prediction error increases significantly, when the vehicle is manoeuvring.

Partial Outage Situations

In practice, a very common situation is a vehicle traveling in urban canyons. In these cases, satellite availability decreases significantly and may continue for a long time. In this sub-section different elevation masks are applied to C^3NAVG^{2TM} to simulate a partial outage situation and the results are analyzed.

Figure 5-11 shows the results of the integrated position errors using pseudeorange at different elevation masks. The figure shows that at a 30° elevation angle, the position error has a maximum value of about 1 metre with a zero mean, but at a 40° elevation angle the maximum east error is up to 4 metres. Checking the observation numbers, there were 4508 position and velocity solutions at a 15° elevation mask. This number drops to 4443 at a 30° elevation mask. When the elevation mask increased to 40°, the position and velocity solution drops to 3094. The main reason for this is that the higher the elevation mask, the smaller the number of available satellites, which degrades the accuracy of GPS. For the GPS/INS integration software, when there is a lack of measurements (i.e. positions and velocities), there are a larger errors. Compared with the reference trajectory values (the results from FLYKIN^{TM} using 15° elevation mask), the statistics are shown in Table 5-8. This table shows that the results are degraded significantly compared to the reference value. The reason for this is a lower number of satellites causing a degradation of the availability for the GPS/INS integration software. Therefore, the integration accuracy degrades significantly.

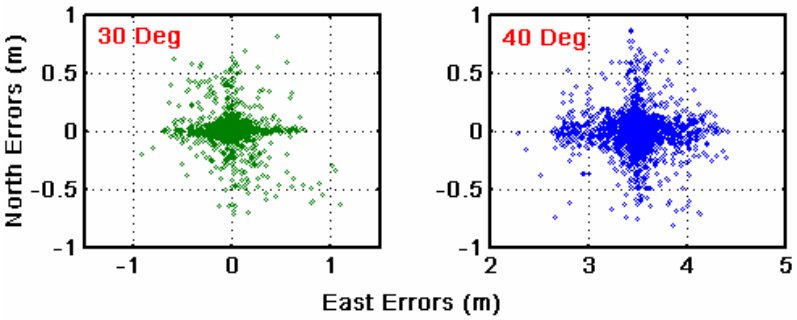

Figure 5-11 Horizontal Position Errors at High Elevation Masks

There are two ways to improve the accuracy of a GPS/INS integrated system in case of a high elevation masking. One is using tightly coupled integration approach, which is less sensitive to a decrease in the satellite availability. The other is using a combined GPS/Galileo constellation (in the future), which can maintain satellite availability in extreme high elevation masking situations (O'Keefe, 2001).

Table 5- 8 Position Degradation Due to High Elevation Mask

Elevation Angle (Deg.)		30	35	40
East Error (m)	**Mean**	11.60	11.90	10.38
	RMS	15.46	11.46	14.42
	MAX	35.92	35.92	35.92
North Error (m)	**Mean**	-14.25	-14.10	-13.58
	RMS	12.46	14.51	13.97
	MAX	26.86	31.86	31.86

5.4 GPS versus GPS/INS Integrated Results Using a Wave Estimator

As discussed in Chapter 3, the accuracy of a Kalman filter is limited by the system input noise level. The analysis in Section 5.3 proved this conclusion. When the conventional Kalman filter was modified to an IAE adaptive filter, the system noise was estimated adaptively while the measurement noise stayed unchanged. From Table 5-6, it can be seen that non- properly selected **Q** values did affect the Kalman filtering results. However, the accuracy improvement by using the IAE filter is still limited by the system

noise. As there are no attitude reference for the field test data, this section will only discuss the position and velocity estimation accuracies by using a wave estimator and compare them with the estimation results from the IAE adaptive Kalman filter.

As discussed in Section 3.2.3, the gyro drift can be described as a slow varying disturbance. A pseudo-random model can be used to describe its property. Its state space model can be expressed by equation (3-49). In one wave cycle, c_0 and c_1 are constant, their value changes only when a new wave cycle started. A test and trial method was used to find a suitable value of the wave cycle. The estimation errors for different wave cycles are shown in Table 5-9. Among these results, a wave cycle equal to 300 seconds gave relatively better results. Figure 5-12 and 5-13 show the estimated velocity and position errors respectively by using the wave estimator (WE) with the wave cycle equal to 300 seconds. As a result, there are no estimates in the first cycle as mentioned in Section 3.3. Therefore, what is shown in these figures is the estimation error starting at the second wave cycle. Table 5-7 shows the statistics of position and velocity errors with the wave cycle equal to 300 seconds. The jumps at the beginning of some wave cycles in Figure 5-12 are caused by improperly selected initial values of the vector **s** for that wave cycle, and the assumption that the wave coefficient of the input noise changes at a fixed interval. In this case 300 seconds here, might not be optimal.

From Figure 5-12 it can also be seen that the north channel has more jumps than the east channel, though its effect is not big enough to show noticeable differences in the mean and RMS values in Table 5-10. One reason for this is that the inertial sensor noise along the north and east axes have different wave cycles. The same cycle time (300s) is used to describe both of them, which may cause errors, since it may not be able to be optimal for both axes. The second reason is that there is not sufficient static data to do initial drift testing and scale factor calibration, so these errors will affect the estimates.

Table 5-10 shows that 300-seconds interval is a reasonable choice for a wave cycle for this data set. Comparing Tables 5-4 (highlighted lines) and 5-10, it can be seen that the position estimation results have no improvement, and in fact the Kalman filter shows

marginally better results. For velocity, the wave estimation errors improved by about 50%. For example, the RMS value of the north velocity error is 3.0 cm/s using a Kalman filter, whereas it improved to 1.3 cm/s when using the wave estimator. It should be noted that these improvements are nearing the accuracy of the velocity reference.

It can be concluded that wave estimation shows an improved performance in comparison with a Kalman filter in the situation where the input disturbances are of low frequency, slow varying in nature, and for relatively weak observables in the state vector. The results show that by using the wave estimator, velocity estimation but not the position estimation, gives better results in comparison with the Kalman filter for this data set. This is because the gyro drift was modeled by a deterministic model in a wave cycle. The state vector, which has a stronger relation with it, will benefit by the wave approach. On the other hand, the position error, which does not have a strong relation with the gyro drift, has no direct benefit.

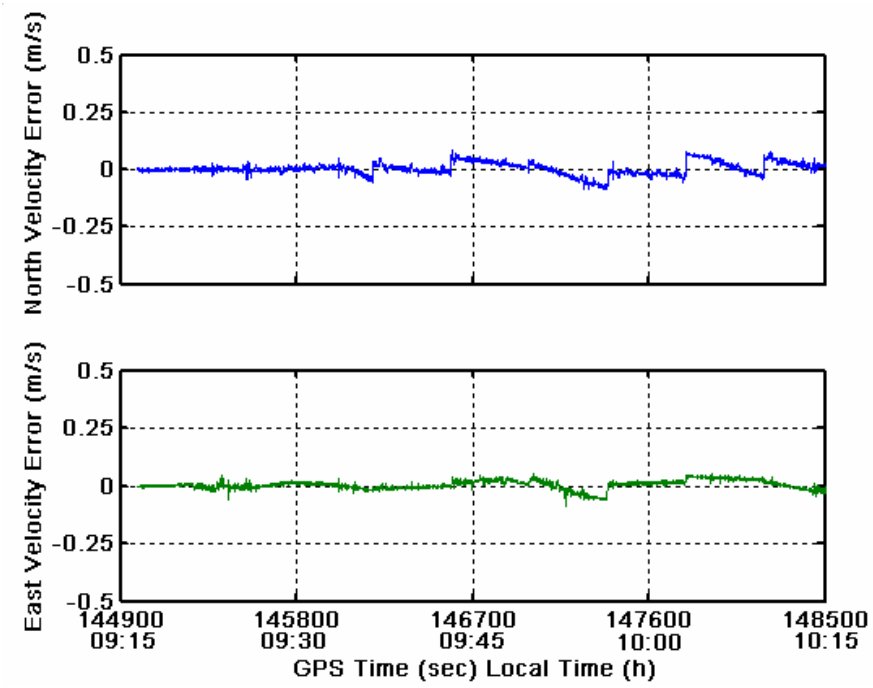

Figure 5-12 Velocity Estimation Error of the Wave Estimator for Field Data

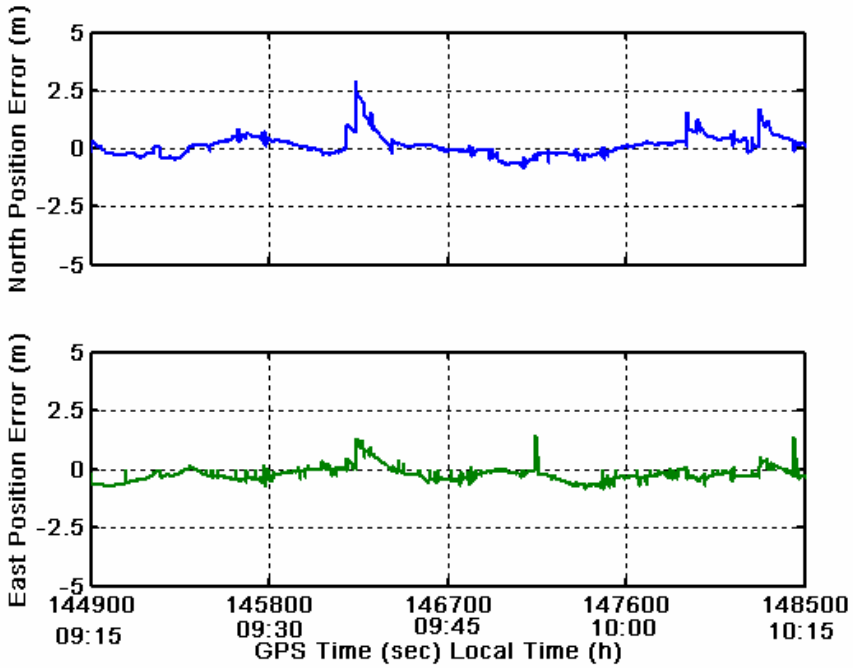

Figure 5- 13 Position Estimation Error of The Wave Estimator for Field Data

Table 5- 9 Velocity Errors for Different Wave Cycles

Cycle (s)	**North Velocity (cm/s)**		**East Velocity (cm/s)**	
	Mean	**RMS**	**Mean**	**RMS**
200	0.79	2.46	-0.23	2.02
250	0.88	2.59	-0.58	1.82
300	**0.01**	**0.25**	**-0.01**	**0.26**
350	1.06	2.93	-0.2.2	2.20
400	0.89	3.85	0.86	12.6
500	1.60	4.78	0.46	3.15
600	0.66	4.98	0.58	6.62

Table 5-10 Error statistics of wave estimation

Component	Mean	RMS
Latitude (m)	0.34	0.56
Longitude (m)	-0.29	0.68
North Velocity (cm/s)	0.10	1.30
East Velocity (cm/s)	-0.10	1.30

5.5 Summary

The objective of this research was to develop a metre-level integrated navigation scheme using a medium accuracy IMU. An inertial navigation system, in principle, permits autonomous operation. However, due to its error propagation characteristics, most applications requiring high terminal accuracy utilize external aiding to reduce the INS error, GPS, in this case. As discussed in the previous chapters, a feedback aiding technique has been used to develop this loosely coupled GPS/INS integration system. The residuals formed by differencing the INS position and velocity from the GPS position and velocity are sent to the Kalman filter. The Kalman filter contains an internal model of the INS error dynamics, and processes the measurements to estimate the values of INS errors. A feedback scheme, which offers greater robustness, is selected. The error estimates are then used to correct the navigation data within the INS itself. An adaptive **Q-**only IAE adaptive filter is used to average the input noise since the system under investigation is stationary. The wave estimation result showed improved performance in comparison with a Kalman filter where the input disturbances are of low frequency, slow varying in nature, and have relatively weak observables in the state vector. As discussed in Section 4.4, the convergence process of the state vector component is different from one to the others; the transit time depends on the observability. Data analysis results show that the position and velocity errors converge first, the misalignment angles follow, and the gyro drift component needs at least 40 seconds to converge. Therefore, the gyro drift is considered as a weakly observed state, and is modelled as pseudo-random model in the wave estimator. In this chapter, both the Kalman filter and wave estimator are used to

process the field test data. The integration of GPS and INS has been proven very successful. According to the test results, a brief summary is given as follow:

1. Pseudorange DGPS position and velocity updates limited the time dependent INS position and velocity errors through Kalman filtering.

2. Using a Kalman filter, the maximum position error is less than 1 metre in the horizontal. The RMS values for position are less than 0.12 m. The RMS values for velocity are less than 0.17 m/s.

3. For a full GPS outage situation with no vehicle manoeuvring, the INS prediction accuracy is from 0.25m to 1.26m during 5 and 10 s simulated GPS data gaps, respectively.

4. For a full GPS outage situation with vehicle manoeuvrings, and the maximum acceleration is up to 2.11 m/s^2, the INS prediction accuracy varies from 3.15 m to 12 m during 5 and 10 s GPS data gaps.

5. For partial GPS outage, 35° and 40° elevation cut-off angles were simulated. The results show that as the elevation mask increases, the available satellites decreased. This degraded the availability, reliability, and integrity of GPS greatly with significant position errors appearing.

6. The remedies for partial GPS outages are to use tightly integrated schemes or GPS/Galileo constellation combinations.

7. INS prediction accuracy is highly related with the vehicle dynamics and the properties of inertial sensors. Non-stationary errors may be large if the system is not well calibrated before it is switched to the navigation mode.

8. An IAE adaptive filter is used to average the input noise since a stationary system is under investigation in this case. The results show that the level of input uncertainties in the system model restricts the estimation accuracy. The accuracy cannot be increased within the scope of this type of modeling method.

9. The wave estimation results show that for the velocity estimation, better results are obtained in comparison with the Kalman filter. The reason for that is the gyro drift, which in this case is modeled by a wave function. It is deterministic over a wave cycle. The state vector has a stronger relation with it, and will benefit by the wave approach. On the other hand, the position error, which does not have a strong relation with the gyro drift, has no direct benefit. As there was no attitude reference for this field data set, the estimation results for the misalignment angles were not be able to be analysed.

10. The wave cycle should be selected very carefully. It was shown that an improperly selected wave cycle will result in larger errors. An improperly chosen initial value for the vector **s** at the beginning of each wave cycle will also cause errors of the estimates in the current wave cycle.

11. In practice, the slowly changed sensors' biases can be described more accurately by using an adaptive varying cycle time. Therefore, estimation cycle-time adaptive choice will be a future research subject.

CHAPTER 6

CONCLUSIONS AND RECOMMENDATIONS

The contribution of this research was in the development and testing of a GPS/INS integration scheme for metre-level positioning using a medium accuracy IMU. An INS mechanization model was developed through the research and the navigation solutions obtained from the existing GPS software (C^3NAVG^{2TM} and $FLYKIN^{TM}$). These were combined in a loosely coupled GPS/INS approach, and both a Kalman filter and a wave estimator were designed and implemented. A simulated data set and a filed test data set were used to assess the algorithm and mathematical models. The advantage of the wave estimation approach is that it shows improved performance in comparison with Kalman filter in a situation where the input disturbances are of low frequency, slow varying in nature, and a relatively weak observables in the state vector. The improvement is obvious in the estimation of misalignment angles. As there was no attitude reference for the field test data, these results are only shown in simulated data. One of the advantages of GPS/INS integration is that the INS predicted positions and velocities are available during GPS outages. Full and partial GPS outages were simulated respectively and the INS prediction results were analyzed in details for the field data. The following conclusions address the findings in both the application of a Kalman filter and the wave estimator.

6.1 Conclusions

The following conclusions regarding GPS/INS integration using both a simulation data set from a CastNav 4000 GPS/INS simulator and a field data set from a medium accuracy IMU for metre-level positioning made from this research are:

1. The achievable accuracy of GPS/INS integration using a medium accuracy IMU is at the metre-level using both simulated data and land vehicle field test data when consistent GPS updates are available. The GPS updates were at a 1 Hz data rate in this case.

2. The Honeywell HG1700, a medium accuracy IMU, used in this research can successfully bridge the GPS gaps. The prediction accuracy is a function of the initial errors at the beginning of the outage and the vehicle dynamics.

3. The partial GPS outage, which often happens in urban canyons and mountainous areas, degrades the integration accuracy. The remedies for partial GPS outages are to use tightly coupled integration schemes or to use GPS/Galileo constellation combinations which will be available in the future.

4. Another advantage of the GPS/INS integration system is that it can provide attitude information. This is usually impossible for off-shelf GPS receivers. For a medium to low accuracy IMU, INS-only derived attitude has a low accuracy. With GPS corrections, the horizontal misalignment angles have a RMS value of 1.2 arc-minutes when a Kalman filter was applied.

5. The Kalman filter has a sequential convergence property. Data processing results show that the position and velocity estimation errors converge first, misalignment angles follow, and the gyro drift took about 40 seconds to converge. Gyro drift and misalignment angles are considered as weakly observed state vectors.

6. Wave estimation is suitable for low frequency, slow varying disturbances. Gyro drift was modeled by a wave function in this research. A wave estimator was applied to both the simulation and the field data. The results from the simulation data shows that wave estimation improved the estimation accuracy to the weakly observed states. The estimation accuracy of the misalignment angle improved greatly, because it has a close relationship to the gyro drift. Improved estimation accuracy for the velocity error estimates is achieved as well since the misalignment angle affects the velocity equation directly. Since there was no attitude reference for the field data, attitude estimation can not be evaluated. However, the velocity estimate yields improved results.

7. A fixed wave cycle has been used in processing this data set. In practice, the slowly changed sensors' bias can be described more accurately by using a changing cycle time. Therefore, estimation cycle-time adaptive choice will be a future research subject.

8. For a Kalman filter, IAE was used to average input noise since a stationary system is under investigation in this case. The result shows that the level of input uncertainties in the system model restricts the estimation accuracy. The accuracy cannot be increased within the scope of this type of modeling method.

6.2 Recommendations

Based on the results of this research, the following recommendations regarding improvement of the performance of GPS/INS integration for metre-level positioning using a medium accuracy IMU are drawn:

1. Embedding the GPS solution software into the GPS/INS integration software will be beneficial from the user's point of view.

2. In order to improve the IMU prediction accuracy during GPS outages, an initial calibration and gyro drift testing algorithm should be introduced and applied before the system starts to work. In the case of long partial GPS outages, it is necessary to introduce ZUPT to the system in order to improve the INS-only solutions.

3. As discussed in Section 5.4, the selection of wave cycle is important to the estimation results of a wave estimator. Adaptive wave cycles should be introduced since each wave cycle may not exactly be the same length.

4. A further improvement of wave estimation and its application to real time GPS/INS integration system should be investigated.

5. The tightly coupled GPS/INS integration scheme should be considered in order to improve the integration accuracy during partial GPS outages (Petovello, 2003).

6. Consider the GPS/Galileo constellation combination to increase available satellite number and improve the satellite geometry when the vehicle travels in a city canyon.

REFERENCES

Britting, K.R. (1971) Inertial Navigation System Analysis. Wiley Interscience, New York.

Brown, R.G. (1996), Introduction to Random Signal Analysis and Kalman Filtering with Matlab Exercises and Solutions. Wiley, John and Sons, Inc. 3rd Edition, New York.

Buetler, G.,(1997) Panel Discussion: The Civil and Military Issues Facing GPS and GNSS. Proceedings of 10th International Technical Meeting of the Satellite Division of the Institute of Navigation, Kansas City, USA, pp.3-20.

Buetler, G., Weber, W., Hugentobler, U., Rothacher, M., and Verdun, A. (1998) GPS for Geodesy. Springer-Verlag.

Bugoslavskaya, N.Y. (1962) Solar Activity and the Ionosphere, for Radio Communications Specialists. Pergamon Press Ltd., New York.

Cannon, M.E. (1991), Airborne GPS/INS with an Application to Aerotriangulation. UCGO Report #20040, Department of Geomatics Engineering, University of Calgary.

Cannon, M.E. (1992), Integrated GPS-INS for High Accuracy Road Positioning, Journal of Surveying Engineering, Vol. 118, pp.103-117.

Cannon, M.E., Lachapelle, G., Szarmes, M, Herbert, J., Keith, J. and Jokerst, S. (1997), DGPS Kinematic Carrier Phase Signal Simulation Analysis for Precise Velocity and Position Determination. Proceedings of the ION NTM 97. Santa Monica, CA. USA. pp. 335-350.

Cannon, M.E., Lachapelle, G., Sun, H., Fletcher, T., Hawes, I., and R. Caballero (1999), Development and Testing of an Integrated INS/GPS Crossed-Linked System for Sub-Meter Positioning of A CF-Jet Fighter, Proceedings of the ION Annual Meeting, June 28-30, Cambridge, MA, pp. 801-809.

Cast Navigation Inc. (2001), CAST 4000 GPS/INS Simulator Product Description, http://www.castnav.com/products/cast4000.pdf

Cast Navigation Inc. (2003), A Leader in GPS and GPS/INS Simulation and Integration Tools, A product introduction presentation provided by the Cast Navigation Inc.

Dong, X. Zhang, S. and Z. Hua (1998), GPS/INS Integrated Navigation System and its Application , Changsha Science and Technology University Press (in Chinese).

El-Rabbany, A. (2002), Introduction to GPS, The Global Positioning System. Artech House, INC.

Farrell, J. and M. Barth (1999), The Global Positioning System and Inertial Navigation. McGraw-Hill.

Ford. T, Neumann, J, and M. Bobye (2001), OEM4_Inertial: An Inertial/GPS Navigation System on the OEM4 Receiver, Proceedings. of the International Symposium on Kinematic Systems in Geodesy, Geomatics and Navigation. Banff, Canada, June 5-8, 2001 pp. 150-168.

Fortes, L., (2002). Optimizing the Use of GPS Multi-Reference Stations for Kinematic Positioning. UCGO Report #20158, Department of Geomatics Engineering, University of Calgary.

Gelb, A. (1974), Applied Optimal Estimation. MIT Press, Cambridge, MA. USA.

Greenspan, R.L. (1996) GPS and Inertial Integration, In: Global Positioning System: Theory and Applications, Chapter 7, Vol. II.

Grewal, M.S., and L.R. Weill (2001) Global Positioning System, Inertial Navigation and Integration. John Wily & Sons, Inc., New York.

Gustafson, D., Dowdle, J., Flueckiger, K. (1996), A Deeply Integrated Adaptive GPS-Based Navigators with Extended Range Code Tracking. Proceedings of PLAN IEEE 2000. San Diego, CA. March 13-16, 2000, pp 118-124.

Hay, C., The Accuracy Improvement Initiative. GPS World. June 2000, pp56-61.

Hofmann-Wellenhof, B., Collins, J., Lichtenegger, H. (2001), Global Positioning System : Theory & Practice, 5th edition, revised. Springer-Verlag New York, Incorporated.

IGS. (2001) IGS Product Table International GPS service, http://igscb.jpl.nasa.gov/components/prods.html.

IGS ACC. General Information About the IGS Product. http://www.aiub.unibe.ch/acc.html.

Jekeli, C. (2000), Inertial Navigation Systems with Geodetic Applications. Walter de Gruyter, Berlin, Germany.

Lachapelle, G. (1998) GPS Theory and Applications ENGO 625 Lecture Notes, Department of Geomatics Engineering, University of Calgary.

Lachapelle, G., (2001) Advanced GPS Theory and Applications ENGO 625 Lecture Notes, Department of Geomatics Engineering, University of Calgary.

Lei, Y.,(1978) Inertial Navigation System. Harbin Engineering University Press, Harbin, China.

Leick, A., (1995) GPS Satellite Surveying. John Wiley and Sons, Inc., 2nd Edition, New York, USA.

Leondes, C.T., (1976), Concepts and Methods in Stochastic Control, Control and Dynamic Systems: Advances in Theory and Applications. vol. 12. Academic Press.

Liu, Z. (1992), Comparison of Statistical methods For the Alignment of Strapdown Inertial Systems. UCGO Report #20047, Department of Geomatics Engineering, University of Calgary.

Lutgens, F.K., Tarbuck, E.J. (1989), The Atmosphere: An introduction to Meteorology. 4th edition. Prentice Hall, Englewood Cliffs, NJ. USA.

Maybeck, P.S. Stochastic Models, Estimation and Control, Volume I. Navtech Book and Software Store, Arlington, USA.

Mohamed, A. H. (1999), Optimizing the Estimation Procedure in INS/GPS integration for Kinematic Applications. UCGO Report #20127, Department of Geomatics Engineering, University of Calgary.

Mohamed, A. H., Schwarz, K.P. (1999), Adaptive Kalman Filter for INS/GPS. Journal of Geodesy. Vol. 73, Issue 4, pp. 193-203.

Nayak, R. (2000), Reliable and Continuous Urban Navigation Using Multiple GPS Antennas and A Low Cost IMU. UCGO Report #20144, Department of Geomatics Engineering, University of Calgary

NovAtel, (1999), OEM3 Millennium GPS Card and Enclosures Guide to Installation and Operation. http://www.novatel.ca/Documents/Manuals/om-20000016.pdf

Ohlmeryer, E.J., Pepitone, T.R., Miller, B. L. (2002), GPS-aided system requirements for start monitors and guided missiles. 37th Annual Gun and Ammunition Symposium. April 15-18, 2002, Panama City, Florida, USA. pp. 1-16.

O'Keefe, K., (2001) Availability and Reliability Advantages of GPS/Galileo Integration. ION GPS, Salt Lake City, USA. September 11-14, 2001. pp. 100-120.

Petovello, M., Cannon, E., Lachapelle, G. C3NAVG2TM Operation Manual, Department of Geomatics Engineering, The University of Calgary.

Petovello, M., (2001), Real-Time Integration of Precise GPS Data with Inertial Navigation Sensors. Special Project Course Report, Department of Geomatics Engineering, The University of Calgary.

Petovello, M., Cannon, M. E, Lachapelle, G., (2003), Quantifying Improvements from the Integration of GPS and a Tactical Grade INS in High Accuracy Navigation Applications. NTM 2003, January 22-24, Anaheim, CA. USA, in press.

Raquet, J. (1998), Development of a Method for Kinematic GPS Carrier-Phase Ambiguity Resolution Using Multiple Reference Receivers UCGO Report #20116, Department of Geomatics Engineering, University of Calgary.

Ray, J.K., Salychev O.S., and M.E. Cannon (1999), The Modified Wave Estimator as an Alternative to a Kalman Filter for Real-Time GPS/Glonass-INS Integration. Journal of Geodesy, Vol. 73, Issue 10, pp. 568-576.

Ray, J.K., (2000), Mitigation of GPS Code and Carrier Phase Multipath Effects using a Multi-Antenna System. UCGO Report #20136, Department of Geomatics Engineering, University of Calgary.

Roulston, A., Talbot, N., and Zhang, K. An Evaluation of Various GPS Satellite Ephemerides. Proceeding of the 13th International Technical Meeting of the Satellite Division of the Institute of Navigation, Salt Lake City, September 2000, pp. 45-54.

Salychev, O.S., and A.B. Bykovsky (1991), Wave Method in Processing Navigation Information in Survey Systems, International Association of Geodesy Symposia 107: Kinematic Systems in Geodesy, Surveying, and Remote Sensing, pp. 238-246.

Salychev, O.S. (1995), Inertial Surveying: ITC Ltd. Experience. Bauman MSTU Press, Moscow.

Salychev, O.S. (1998), Inertial Systems in Navigation and Geophysics, Bauman MSTU Press, Moscow.

Salychev O.S., V.V.Voronov, M.E. Cannon, R.Nayaka, G. Lachapelle (2000), Low cost INS/GPS integration: Concept and Testing, Proceedings of the ION National Technical Meeting, Anaheim, CA. January 26-28, pp.705-711.

Salychev, O.S. (2001), Lecture Notes for ENGO 699.44: Inertial Navigation Systems in Geodetic Applications, Department of Geomatics Engineering, University of Calgary.

Salychev, O.S. (2003), A personal communication.

Scherzinger, B., (2001), Robust Inertially-Aided RTK Position Measurement, Proceedings. of the International Symposium on Kinematic Systems in Geodesy, Geomatics and Navigation. Banff, Canada, June 5-8, 2001. pp. 265-272.

Schwarz, K.P. and Wei, M., (2000), Lecture Notes for ENGO 623: INS/GPS Integration for Geodetic Applications, Department of Geomatics Engineering, The University of Calgary.

Schwarz, K.P. and Zhang, G., (1994), Development and Testing of a Low-Cost Integrated GPS/INS, Proceedings of ION GPS International Technical Meeting, Salt Lake City, September 20-23, pp. 1137-1144.

Seeber, G. (1993), Satellite Geodesy Foundations, Methods, and Applications. Walter de Gruyer, Berlin.

Skone, S., (1999), Atmospheric Effects on Satellite Navigation Systems. ENGO 699.56 Lecture Notes, Department of Geomatics Engineering, The University of Calgary.

Skone, S., Cannon, M.E., Karunanayaka, M.D., Nicholson, N., (2003), Wide Area DGPS Performance Analysis, Proceedings of CASI AGM03, Montrèal, Quebec, Canada, April 28-30, to be published.

Spilker Jr., J. A. (1996), Global Positioning System: Theory and Applications. Volume I. American Institute of Aeronautics and Astronautics, Inc., Washington D. C., USA.

Wang, J., Stewart, M.P., and M. Taskiri (2000), Adaptive Kalman Filtering for Integration of GPS with GLONASS and INS, International Association of Geodesy Symposia 121: Geodesy beyond 2000, The Challenges of the First Decade.

Wanninger, L., Effects of the Equatorial Ionosphere on GPS, GPS World, July 1993.

Wong, R.V.C., (1988), Development of a RLG Strapdown Inertial Survey System, UCGO Report #20027, Department of Surveying Engineering, University of Calgary.

Yi, G., (1987), Principle of Inertial Navigation System, Aviation Press, Beijing, China.

Zhang, X., (2001), Integration of GPS and INS for Metre-Level Positioning, Special Reading Course ENGO699.68 Report, Department of Geomatics Engineering, The University of Calgary.

Zhang, X., Cannon, M.E. (2002), Integration of GPS with a Medium Accuracy INS for Meter-Level Positioning Using a Wave Estimator, Proceedings of Institute of Navigation 58th Annual Meeting, Albuquerque New Mexico, USA, June 241-249, pp.

Zheng, D., (1998) Linear System Theory. Tsinghua University Press, Beijing, China.